RICE UNIVERSITY

Array microscopy technology and its application to digital detection of Mycobacterium tuberculosis

by

Brian P. McCall

A THESIS SUBMITTED
IN PARTIAL FULFILLMENT OF THE
REQUIREMENTS FOR THE DEGREE

Doctor of Philosophy of Bioengineering

APPROVED, THESIS COMMITTEE

Tomasz Tkaczyk, Assistant Professor
Rice University, Bioengineering and Electrical and Computer Engineering
Thesis Committee Chair

Rebecca Richards-Kortum, Professor and Chair
Rice University, Bioengineering and Electrical and Computer Engineering

Edward A. Graviss, Associate Member
The Methodist Hospital Research Institute, Center for Molecular and Translational Human Infectious Diseases Research

Richard G. Baraniuk, Professor
Rice University, Electrical and Computer Engineering

HOUSTON, TEXAS
April 2013

ABSTRACT

Array microscopy technology and its application to digital detection of Mycobacterium tuberculosis

by

Brian P. McCall

Tuberculosis causes more deaths worldwide than any other curable infectious disease. This is the case despite tuberculosis appearing to be on the verge of eradication midway through the last century. Efforts at reversing the spread of tuberculosis have intensified since the early 1990s. Since then, microscopy has been the primary frontline diagnostic. In this dissertation, advances in clinical microscopy towards array microscopy for digital detection of *Mycobacterium tuberculosis* are presented. Digital array microscopy separates the tasks of microscope operation and pathogen detection and will reduce the specialization needed in order to operate the microscope. Distributing the work and reducing specialization will allow this technology to be deployed at the point of care, taking the front-line diagnostic for tuberculosis from the microscopy center to the community health center. By improving access to microscopy centers, hundreds of thousands of lives can be saved. For this dissertation, a lens was designed that can be manufactured as 4×6 array of microscopes. This lens design is diffraction limited, having less than 0.071 waves of aberration (root mean square) over the entire field of view. A total area imaged onto a full-frame digital image sensor is expected to be 3.94 mm^2, which according to tuberculosis microscopy guidelines is more than sufficient for a

sensitive diagnosis. The design is tolerant to single point diamond turning manufacturing errors, as found by tolerance analysis and by fabricating a prototype. Diamond micro-milling, a fabrication technique for lens array molds, was applied to plastic plano-concave and plano-convex lens arrays, and found to produce high quality optical surfaces. The micro-milling technique did not prove robust enough to produce bi-convex and meniscus lens arrays in a variety of lens shapes, however, and it required lengthy fabrication times. In order to rapidly prototype new lenses, a new diamond machining technique was developed called 4-axis single point diamond machining. This technique is 2-10x faster than micro-milling, depending on how advanced the micro-milling equipment is. With array microscope fabrication still in development, a single prototype of the lens designed for an array microscope was fabricated using single point diamond turning. The prototype microscope objective was validated in a pre-clinical trial. The prototype was compared with a standard clinical microscope objective in diagnostic tests. High concordance, a Fleiss's kappa of 0.88, was found between diagnoses made using the prototype and standard microscope objectives and a reference test. With the lens designed and validated and an advanced fabrication process developed, array microscopy technology is advanced to the point where it is feasible to rapidly prototype an array microscope for detection of tuberculosis and translate array microscope from an innovative concept to a device that can save lives.

Acknowledgments

I would like to thank my adviser, Dr. Tomasz Tkaczyk, for guidance and support during my five years at Rice. This dissertation was made possible by his vision, motivation, and advocacy of the research presented here.

I would also like to thank my other committee members for their contributions and guidance in this research. In particular, I would like to thank Dr. Edward Graviss for making resources for this research available at The Methodist Hospital. I would like to thank Dr. Rebecca Richards-Kortum for the shared equipment which made this research possible and for providing feedback and guidance on the design, execution, analysis, and presentation of experiments.

I would like to thank Dr. Randall Olsen for his valuable insights in clinical pathology and for his tireless efforts in executing experiments for the benefit of my research. For the same reasons, I would also like to thank Dr. Nicole Nelles and Dr. Dawn Williams. I would like to thank Judith Mardoquio and Patricia Cernoch at The Methodist Hospital for their help in obtaining materials needed to conduct this research.

Several past and current lab members have provided a great deal of assistance throughout my time at Rice, including Dr. Robert Kester, Dr. Liang Gao, Dr. Nathan Hagen, Dr. Michal Pawlowski, Dr. Noah Bedard, Dr. Matthew Kyrish, Kevin Jackson, Chris Fan, Roberto Cortés, Alessandra Forcucci, and Adam Shadfan.

Last but not least, I would like to thank Patrick Peter McCall and Patrick Columkille McCall. They are the giants whose shoulders I stand on.

This research was done with support from the Virginia and L. E. Simmons Family Foundation, internal funding through The Methodist Hospital Research Institute Department of Pathology and Genomic Medicine, and Award Number U54AI057156 from the National Institute Of Allergy And Infectious Diseases. The content does not necessarily represent the official views of the Simmons Family Foundation, the National Institute of Allergy And Infectious Diseases, or the National Institutes of Health.

Contents

List of Figures

List of Tables

List of Equations

Nomenclature

AIDS	Acquired immunodeficiency syndrome
AFB	Acid fast bacteria/bacilli
ASOM	Adaptive scanning optical microscope
BD	Becton-Dickinson
CCD	Charged couple device
CDF	Cumulative density function
CNC	Computer numerical control
DOTS	Directly observed treatment short course
DSLR	Digital single lens reflex
FG	Freeform generator
FOV	Field of view
FSSM	Fluorescence sputum smear microscopy
FTS	Fast tool servo
FWHM	Full width at half maximum
HIV	Human immunodeficiency virus
IRB	Institutional Review Board
ISO	International organization for standardization, refers here to standards for sensitivity in photography and digital photography sensors.
LED	Light emitting diode
LVDT	Linear variable differential transformer
MP	Megapixel

MTB/Mtb	*Mycobacterium tuberculosis*
MTF	Modulation transfer function
NA	Numerical aperture
NC	Numerical control
NOA	Norland optical adhesive
PCR	Polymerase chain reaction
PSF	Point spread function
PV	Peak-to-valley
RGB	Red, green, and blue pixels/color space
RIF	Rifampicin
RMS	Root mean square
RPM	Rotations/revolutions per minute
R_q	Root mean square / quadratic mean roughness
RSS	Root sum square
SLR	Single lens reflex
SPDM	Single point diamond machining
SPDT	Single point diamond turning
SSM	Sputum smear microscopy
ss+/ss-	Sputum smear positive / sputum smear negative
STS	Slow tool servo
TB	Tuberculosis
TIR	Total indicator runout
TMH	The Methodist Hospital

TMHRI	The Methodist Hospital Research Institute
TOMBO	Thin observation modules by bound optics
UPL	Ultra-precision lathe
USAF	United States Air Force
USB	Universal serial bus
UV	Ultra-violet
WD	Working distance
WEC	Workpiece error compensation
WHO	World Health Organization

Chapter 1

Introduction

The second half of the 20th century saw a rise in the global rates of incidence of active *Mycobacterium tuberculosis* (Mtb) disease, also known as tuberculosis (TB), in many developing countries. This disease had been all but wiped out in modernized countries by the 1950s, but with the advent of acquired immunodeficiency syndrome (AIDS) brought about by the human immunodeficiency virus (HIV), in 1993 TB had been declared a global emergency [1]. By this time, TB had become the leading cause of death among curable infectious diseases in the world [2]. The World Health Organization (WHO) introduced the directly observed treatment short course (DOTS) program to halt and reverse the global increase in the incidence and prevalence of tuberculosis. The goal was to reduce the incidence and prevalence of TB in all regions of the world to half of their levels as of 1990 [3] with the target of reaching 70% case detection for sputum positive cases and 85% cure rates by 2000 [4]. Since the adoption of this initiative,

passive case detection of Mtb by sputum smear microscopy (SSM) has been the cornerstone of the TB case detection effort [3].

The incidence of Mtb peaked in 2004, showing that the WHO strategy has had some success in reversing the trend of increasing incidence and prevalence of active Mtb infections. The reversal and decline have been slower than targeted, however, and the same report concludes that the goal of reducing global incidence rates to half of their 1990 levels by 2015 will not be met [5]. Part of the problem is that the WHO target for case detection is well short of its 70% target. A 1998 study showed that this target, if met, would significantly reduce the incidence and prevalence of Mtb throughout the world, even where rates of human immunodeficiency viral (HIV) infection are high [3]. The actual case detection rate, however, is 53% [6]. It is clear that both the strategy and the technology of TB case detection must be improved significantly in order to meet the WHO targets for TB control.

The reasons for the low case detection rates are the limited accessibility of microscopy centers to large segments of the population [7], the inability of SSM to detect non-pulmonary Mtb [7], and the sensitivity of SSM [8], which studies have shown ranges from 32% to 94% [8]. Due to the limitations of microscopy services, development of new and improved diagnostics has been an ongoing effort [9]. A study by Keeler et al estimated the impact of new diagnostics and concluded that the introduction of a new test similar to SSM with 85% sensitivity and 97% specificity with a turnaround time to results that eliminated the need for a follow-up appointment would save 95,000 – 263,000 lives annually. The number would be on

the lower end if such a diagnostic could only be made available at specialized tuberculosis clinics and on the higher end if it could be made available to 100% of patients seeking health care – i.e., a point of care device [7]. In 2010, the World Health Organization approved the rollout of a polymerase chain reaction (PCR) based test for Mtb and Rifampicin (RIF) resistance, the Xpert® MTB/RIF test, as the front line diagnostic for Mtb case detection [10]. This system provides diagnostic accuracy well above SSM but at a significantly higher cost. The Xpert MTB/RIF system also lacks the ability to deploy as a point of care diagnostic due to the adverse effects of extreme environmental conditions and the need for hours of uninterrupted power supply while processing samples, ample storage space, and dedicated trained personnel. While the Xpert system is a significant advance in front-line diagnostics at the district and sub-district level and superior to SSM services currently offered at microscopy centers, there is still need for a diagnostic tool that can be used for monitoring treatment progress, whether at the point of care or at a microscopy center, and for case detection at the point of care [11].

Microscopy has also seen some recent development. SSM using a fluorescent dye (FSSM) instead of the conventional carbol-fuchsin dye had previously shown increased sensitivity, but only in the last ten years was it demonstrated that there is no decrease in the specificity of the exam [8]. Microscopy also now has the potential to transition to a digital technology in a way that it could not previously. This is because of the rapidly increasing size and pixel count of camera sensors (charged couple devices, CCDs) and high throughput imaging systems. 2, 4, or even 8 megapixels is not enough to image the amount of area examined for SSM. Digital

single lens reflex cameras (digital SLRs or DSLRs) now have large format CCDs with over 20 megapixels (MP). The large number of pixels enables these sensors to image a greater area than was previously possible, but this alone is still not enough. High throughput imaging systems are needed to image multiple fields of view on the same CCD. An example of a high throughput imaging systems is the microscope array, which was developed for virtual slide pathology. With this technology, digital images of whole microscope slides can be acquired rapidly at high resolution, although the equipment for this technology is quite expensive. The technology to fabricate lens arrays for these devices, particularly diamond turning technology, has also advanced in recent years, and has promise as a rapid prototyping technology for the development of new microscope arrays. Figure 1.1 shows a conceptual drawing of a microscope array for Mtb detection. The system consists of an array illumination system, active sample holder, array of microscopes, and DSLR camera. Combining these new technologies into one system has the potential to create a powerful new microscopy diagnostic tool that can have a significant impact in the fight against tuberculosis.

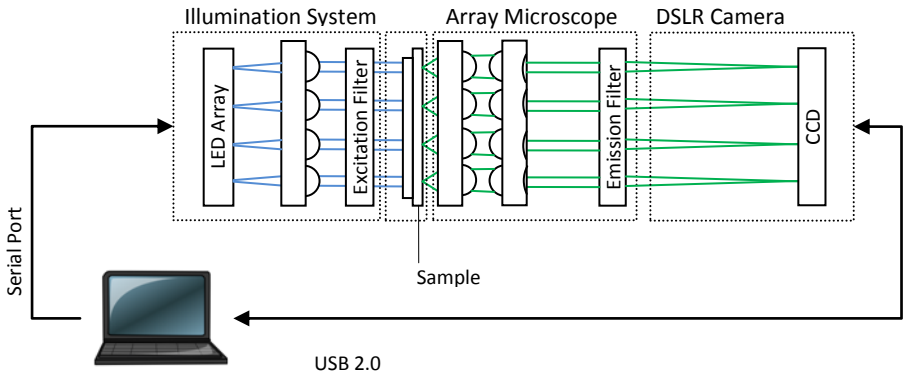

Figure 1.1. System schematic of an integrated diagnostic platform for tuberculosis.

Chapter 2 provides a summary of the goals of this project and the specific aims accomplished during this dissertation. The chapters that follow describe how the accomplishment of these aims overcomes limitations of prior technology and how these aims were accomplished. The aims include a microscope lens design, a validation of the feasibility of the microscope lens using clinical specimen, and array microscope fabrication technology.

Chapter 3 provides the background on the current state of technologies used in this project: SSM, digital pathology, array microscopy, lens fabrication. The limitations of these current technologies, how their limitations affect their applicability to the proposed system, and how the proposed aims overcome this limitations will be described.

Chapters 4 through 6 detail research methods that were used to accomplish the specific aims of this project, and the results and conclusions obtained by these methods.

Chapter 7 summarizes the major outcomes of this dissertation as well as the applicability of this research to applications beyond the motivation for this dissertation.

Chapter 2

Project summary and specific aims

2.1. Project summary

In order to meet the diagnostic needs of TB clinics and community health centers in developing countries, a new diagnostic platform based on array microscopy and digital pathology is proposed. At the heart of this platform is a miniature objective lens that is replicated several times in an array for high throughput imaging, all fitting within the area of a sputum smear. The size constraints prevent the use of conventional microscope objectives, which are about as wide as the sputum smear itself, and miniature endoscopes [12–20], which have very short working distances insufficient magnification for FSSM. Implementation of an array microscope requires the design of a new miniature objective that meets the size and imaging requirements of FSSM. In addition to designing this objective, it

needs to be fabricated as an array of objectives. A number of lens array fabrication techniques have previously been developed and put into use for other applications, but each has its own drawback when applied to array microscopy. Furthermore, existing lens array fabrication techniques tend to lack effective means to self-align multiple lenses for ease of fabrication and assembly. Lastly, the microscope lens design needs to be fabricated and tested with clinical samples to establish that the design meets the standard of FSSM, and is tolerant to the fabrication errors inherent in any fabrication process without loss debilitating loss of image quality.

This diagnostic platform will increase access to better Mtb diagnostics in resource poor countries by virtue of being a rapid test with no need for follow-up that is easy to operate and compact enough to be transported. The cost of this device is expected to be on par with current microscopy platforms, but due to its portability, compactness, and ease of use, will be made more widely available and can be implemented as a part of a more efficient strategy for TB case detection.

2.2. Specific aims

In order to develop and test this system, the following specific aims were set and accomplished for this research:

Aim 1: Design a microscope objective optimized for array fluorescent sputum smear microscopy. In this aim, a lens design is developed to have a low chromatic dispersion and full aberration correction for wavelengths in the emission band of Auramine O. This lens should be diffraction limited, satisfy the imaging

needs of FSSM examination protocols, and be tolerant to reasonable fabrication errors so that actual imaging performance remains diffraction limited. The designed range of wavelengths is centered about the emission peak of Auramine O, but the design should have similar performance over a similar range of wavelengths centered about other dyes, such as Acridine O. The limited chromatic dispersion allows a wide range of wavelengths to focus within the diffraction limited depth of focus. Thus, dyes with background stain of a different color, such as Acridine O, can be imaged with very little blurring in the background stain. The limited chromatic dispersion will also allow the sample to be brought into focus using bright field illumination, which is much brighter than epi-fluorescent illumination.

Aim 2: Build a prototype objective and validate lens design and tolerances for diamond machining fabrication. In this aim, the system designed in Aim 1 will be fabricated and assembled as a single microscope objective using single point diamond turning (SPDT) and integrated into a test platform with a DSLR camera and light emitting diode (LED) epi-illumination system. This platform will be used to validate the lens using standards for image resolution, a qualitative comparison to a benchmark clinical FSSM objective, and testing its diagnostic accuracy in comparison with the same benchmark objective.

Aim 3: Develop a method for fabricating arrays of lenses that can be assembled and self-aligned in an array of microscopes. The method developed in this aim will include a design and discussion of precise fixturing, and alignment procedures during fabrication and assembly. Emphasis is placed on ease of setup,

repeatability of performance over large numbers of arrays, and meeting similar tolerances to those of SPDT.

Chapter 3

Background and significance

This research seeks to combine sputum smear microscopy with array microscopy and digital pathology to bring SSM diagnostic services to the point of care. SSM is a process of examining sputum stained with a dye that highlights Mtb that must be carried out by a trained and experienced microscopist. The need for a trained microscopist limits the availability of SSM services to microscopy centers, which may be 1-2 days travel from the patient's home village. SSM samples can be prepared at the point of care so that the patient need not make the journey, but the slides must still be transported, delaying diagnosis and treatment. Digital images can be transmitted faster and more easily than physical specimen, reducing the time needed to return an examination result. Array microscopy is a new paradigm in microscopy that can be used to increase the digital imaging throughput of a microscope or simplify its operation. This chapter describes the current state of

these three technologies and how they will be combined and improved upon to accomplish the goal of building an array microscope.

3.1. Sputum smear microscopy

Mtb belong to the family of mycobacterium, also known as acid fast bacteria, or AFB. These bacteria are called acid fast because they retain dyes after staining and de-colorization. In active pulmonary tuberculosis, Mtb are found in the lungs and can be coughed up in a patient's sputum. In order to perform a SSM examination, this sputum is collected and smeared over a 20 mm × 30 mm area on a glass slide. The smear is typically prepared using the following steps [21]:

1. Heat fixing
2. Staining (while still heating)
3. De-colorization
4. Counterstaining

Heat fixing helps bacteria adhere to the glass slide and take up more dye. This is one of the steps that adds delay to the return of the result and requires some skill as it can damage the smear and render it diagnostically useless. Some protocols have been tested that eliminate the heat fixing step, as well as the heating during staining for these reasons [22,23]. By comparison, the fluorescent dye requires no heating during staining [24].

After the slide is prepared, it is visually examined using a 100x microscope objective and usually a 2.5x or 4.5x eyepiece. Mtb appear as red elongated rods as shown in Figure 3.1. A minimum of 100 fields of view must be examined (equaling roughly 3mm^2 total area) before a negative diagnosis can be determined [21].

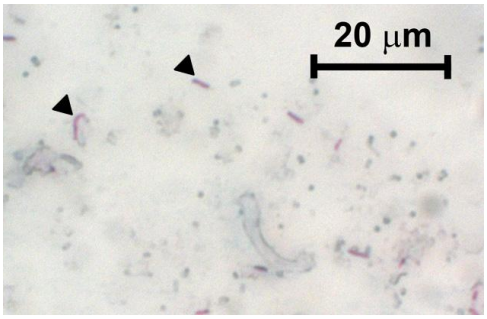

Figure 3.1. Sputum smear with Ziehl-Neelsen stain, 100x magnification, Courtesy Mark Pierce, Kortum Lab. Black arrows indicate some of the bacilli that can be seen in this image.

The cost of SSM diagnostics is generally modest compared to the diagnostic equipment found in hospitals everywhere in developed countries. Light emitting diode (LED) microscopes designed for FSSM detection of TB as well as other infectious diseases are made available to low income countries at a discounted price of $2,000 per microscope [25]. The cost per test is minimal. The Global Focus microscope, introduced in 2010, costs even less, with a price tag of about $240. Initial tests demonstrate excellent concurrence with current SSM examinations [26]. This microscope is still in the evaluation stage, but represents a significant cost reduction in SSM equipment. These prices are quite modest for equipment that can be used for hundreds of SSM examinations daily, and represent a one-time cost, but for some community health centers, the cost of the microscope is not the only

hurdle in its adoption. The expertise needed to examine a sputum smear and report an accurate diagnosis is another factor to consider in adopting a point of care device.

SSM protocols typically recommend that a person performing an exam have regular experience, as much as one exam per day [21,27]. Nurses and community health workers require a test that is easy to read and gives a definitive qualitative result rather than a test that must be interpreted by an examiner [28]. Access to SSM diagnostics is typically only extended by transporting slides from the point of care to a clinic that is capable of processing them and returning with a diagnosis. This takes at least a day and requires follow-up with a patient. It is not uncommon for follow-ups to be missed, resulting in a missed treatment opportunity. This has a demonstrable detrimental impact on TB related mortality [7]. Fluorescence sputum smear microscopy (FSSM) has been shown to increase sensitivity without loss of specificity, and its protocols are reported to be easier to follow than SSM protocols [8], but specialized training is still needed to examine the slides and report an accurate diagnosis.

3.2. Digital Pathology

Digital pathology simply refers to the digitalization of pathology slides. Slides of any type, including histology slides, blood smears, and sputum smears, can be digitized using a CCD detector and stored digitally. Digital storage of pathology slides is particularly advantageous for slides that degrade or bleach over time, as fluorescent dyes do. Digital slide images can also be transported much more rapidly

than physical slides since all that is required is a cell phone capable of transmitting data. Despite lacking many forms of technology that are taken for granted in developing countries, cell phone coverage is readily found in some of the remotest places in developing countries. The simple ability to transmit slides to a TB clinic or microscopy center for expert diagnosis rather than waiting for the slides to arrive can greatly reduce the time needed to return a diagnosis. The practice of transmitting digital slides electronically in order to receive a diagnosis is referred to as telepathology. In addition to reducing the time needed to return an exam, a particular benefit is that the pathologists to whom the slide images are sent are not restricted to the nearest clinic with microscopy facilities. The can be sent to national or regional hospitals, or anywhere in the world, for that matter.

3.3. Array microscopy

Digital microscopy is primarily limited by imaging throughput. The field of view of a digital microscope is limited by the number of pixels on the detector. A single image at this sampling rate that covers the minimum total area for a sputum smear examination would likely require over 100 MP. Only recently have 21 MP cameras become available commercially, and these cameras typically have a Bayer color mask. For FSSM, this cuts the effective number of useful pixels in half. Scanning is a simple solution to overcome this limitation. Manual scanning of microscope lenses can be a time consuming task for someone not accustomed to the practice, however. This practice is often a little more difficult when attempting to find the proper focus for acquiring a digital image.

Array microscopy has been introduced into digital pathology to resolve this limitation on imaging throughput. In an array of microscopes, miniature lenses are packed tightly together occupying a total area similar to the area occupied by a traditional microscope. These microscopes each image a separate field of view simultaneously. The concept has been applied to whole slide imaging of pathology slides by automatically scanning a microscope array across the length of a pathology slide, as shown in Figure 3.2 [29].

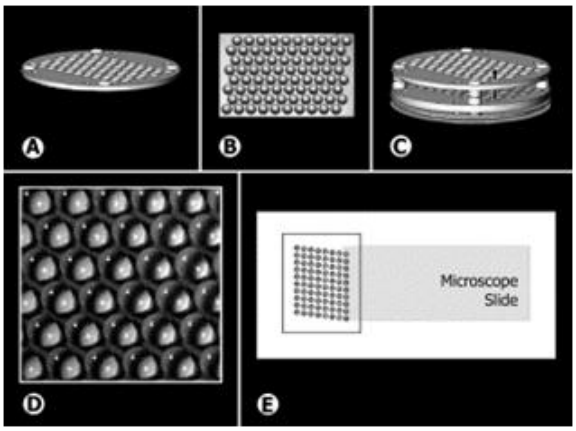

Figure 3.2. DMetrix array microscope for virtual slide pathology [29].

This system did not prove to be cost effective, however, as it required complicated scanning technology in order to acquire the digital images. Another high-throughput approach that uses fewer opto-mechanical components is the Adaptive Scanning Optical Microscope (ASOM). In this system, a scanning mirror in the pupil of a standard microscope objective is tilted to a field of view to image. This system can only image one field of view at a time, though, and it still relies on some scanning to select field of view. It also includes a deformable mirror to correct for field dependent aberrations, which adds to the overall system cost. This system

diagram is shown in [30]. In a remote clinical setting, such specialized components as deformable mirrors are impractical. In array microscopy, each field of view is imaged by an independent objective, so adaptive optical components are not necessary.

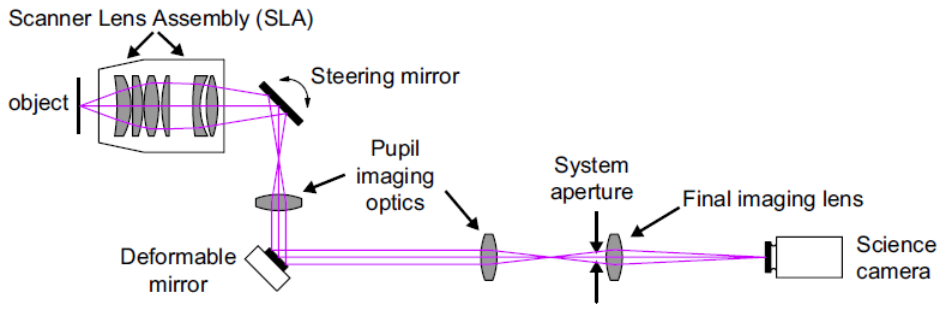

Figure 3.3 Conceptual layout of ASOM [30].

Applications that do not require a continuous field of view are inherently more suitable for array microscopy. An array of lenses can be used to effectively increase the throughput of an imaging flow cytometer [31], and the resulting system is quite simple. FSSM will require an array of miniature microscope objectives, more like the array microscope built by DMetrix than the lens arrays used for flow cytometry. Like flow cytometry, though, FSSM does not require a continuous field of view, so the expensive and bulky lateral scanning equipment used by DMetrix is unnecessary.

Despite the accomplishment thus far in array microscopy, the technology remains relatively undeveloped. Other technologies such as plenoptic cameras [32] and three dimensional imagers [33] have been developed using low-cost lens arrays

in camera systems, but the field of array microscopy has remained dormant. A major contributing factor to the lack of rapid development of a promising technology is the difficulty in producing lens arrays with the size and shape of lenses typically seen in miniature microscope objectives, such as endoscopes [17–19]. The techniques used to produce the type of lens arrays found in plenoptic cameras and thin observation modules by bound optics (TOMBO) [34] include: thermal reflow [35], micro-jet printing of ultra-violet (UV) cured epoxy [36], and grayscale lithography [37]. Each of these techniques has a limitation on one or more parameters of the lens, such as the volume, edge slope, or maximum sag. SPDT is the technique used by DMetrix to fabricate lens arrays, but this technique requires the lens array to be manually repositioned once for each lens in the array on a spindle that requires ultra-precise balancing whenever adjusted. Other diamond machining techniques such as slow and fast tool servo (STS/FTS) can machine precise lenses in a one-step process, but these techniques cannot produce lenses with steep edges [38].

Prior to this research, micro-milling was the only technique capable of producing the full range of lens shapes and sizes needed for a typical miniature microscope objective in brass inserts for plastic injection molding [39]. Although fabricating lens molds with micro-milling was an important advance in the field of diamond machining, the development of new array microscopes is better served by a rapid prototyping process where the lenses are machined directly into plastic, skipping the injection molding step. This allows the development process of array microscopes to become iterative, with prototype array microscopes being fabricated, tested, and improved over multiple generations.

Chapter 4

Design of a miniature microscope objective for array microscopy

This chapter will describe the system specifications needed of an array microscope objective for FSSM and introduce a lens design for an objective that meets these specifications. The contents of this chapter, with the exception of lens prescription data, have been published in a peer reviewed journal article introducing the concept of array microscopy to the community of tuberculosis researchers in a special issue of *Tuberculosis* [40]. The lens prescription data will be published in an upcoming issue of *Archives of Pathology & Laboratory Medicine* [41].

4.1. System specifications

A key part of the design of a microscope array that meets the criteria of the application, FSSM, is the design of a single miniature objective that can be replicated

as a microscope array. Before a lens design can be optimized, some first order parameters or constraints need to be specified. The most important of these parameters are numerical aperture (NA), magnification, field of view (FOV), working distance (WD), outer diameter, and choice of lens material. For applications such as traditional microscopy or endoscopy, the specification of some or all first order lens parameters and constraints is fairly straightforward. The numerical aperture determines the optical resolution of the system. The magnification must at a minimum satisfy the Nyquist sampling criterion, which is based on NA and the CCD pixel size [42]. FOV is generally limited by the size of the detector (whether it be an eye or a camera) and the magnification. For commercial objectives, the outer diameter is often less than 1", but this is arbitrary. Traditional microscopes do not in general have any limit on the outer diameter. In array microscopy, NA and magnification have the same limitations as in traditional microscopy. FOV is not directly constrained by the detector size, however, and outer diameter does have physical constraints. For FSSM, FOV and outer diameter need to be chosen so that enough lenses fit over the size of a sputum smear and image enough area of the sputum smear onto the detector in order to make a diagnosis. Working distance is flexible as well. There is not much flexibility in choice of lens material, as there are only a handful of optical plastics available to choose from. The general imaging criteria that need to be met by each individual miniature objective lens design are listed in Table 4.1, and the reasons for these constraints are discussed.

Table 4.1. General imaging parameters.

Numerical aperture (NA)	0.4-0.55
Magnification (M)	>50x
Array field of view (smear size)	20 mm × 30 mm
Total area imaged	>3 mm^2
Contrast agent	Auramine O
Lens material	Zeonex, polystyrene
Minimum edge thickness	2 mm
CCD dimensions	24 mm × 36 mm
(Canon EOS Mark II DSLR)	6.27 μm × 6.27 μm pixels
	8.87 μm × 8.87 μm spacing b/t green pixels (Bayer mask)

4.1.1. Design wavelengths

The fluorescent dye Auramine O is the intended contrast agent. The spectrum of Becton-Dickenson's Auramine M solution was measured and is shown in Figure 4.1. This solution contains the Auramine O dye along with phenol, glycerine, isopropanol, and purified water. The use of a fluorescent dye simplifies the objective design because with a narrow range of wavelengths to image, the range of chromatic aberrations, including longitudinal aberration, latitudinal aberration, and spherochromatism, is small compared to lens designs for brightfield or broadband imaging. The primary effect of using a dye other than the designed contrast agent is to change the focal length of the objective. It can also alter the balance of aberrations in the lens design, usually for the worse, since the lens design is optimal at the given wavelength.

When designing a lens for fluorescence imaging, it is occasionally sufficient to design the system using only the peak wavelength of the intended dye's emission spectrum. In this case, initial attempts to design the lenses using only a single wavelength yielded designs with such high chromatic dispersion that even fluorescence imaging would be impossible. In order to force the optimizer to account for finite bandwidth of a fluorescent dye and provide a modest amount of aberration correction, the lens design was optimized over several wavelengths grouped tightly within the emission spectrum of Auramine O. The relative weights for the design wavelengths are shown in Table 4.2. The emission filter chosen for design purposes was a Semrock filter FF01-517/20-25. The relative weights in Table 4.2 are based on the filter's transmission spectrum and the emission spectrum of the designed contrast agent.

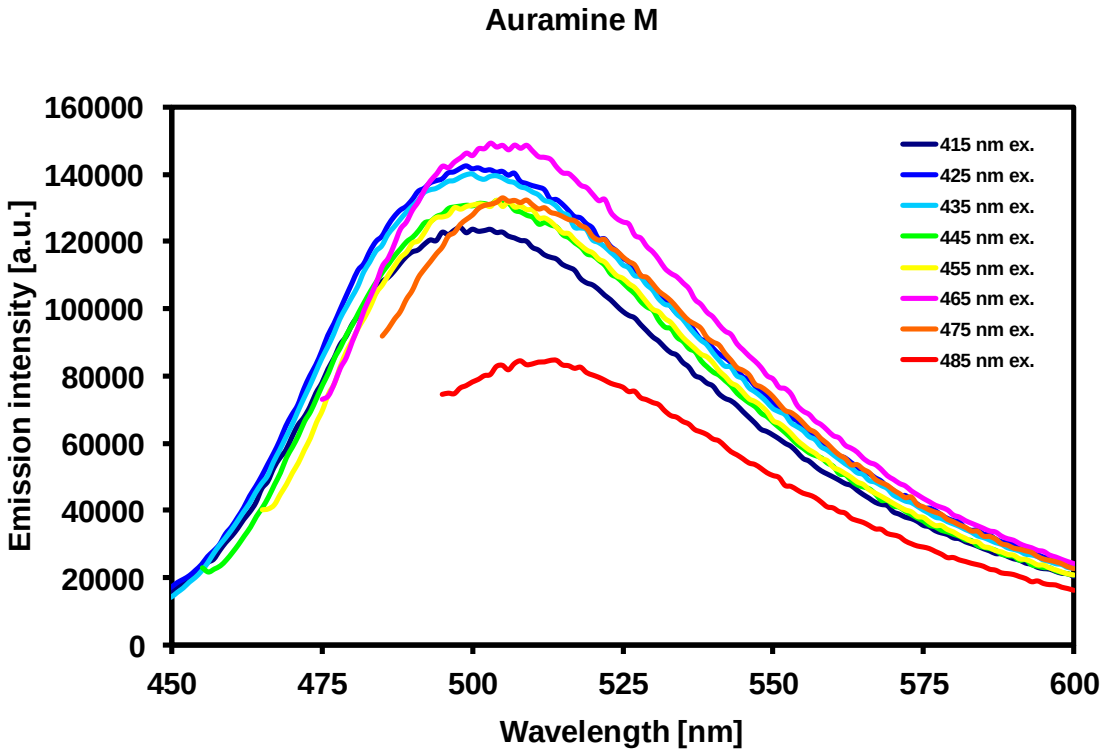

Figure 4.1. Emission spectra of Auramine M, a solution containing the Auramine O dye, for several excitation wavelengths.

Table 4.2. Design wavelengths and relative weights.

Wavelength	Relative weight
0.506	0.76
0.511	0.98
*0.516	0.93
0.521	0.88
0.527	0.79

* - Primary wavelength

Acridine O is another dye that is commonly used to detect microorganisms. When excited at 450 nm, Acridine O stains white blood cells green and the mycolic acid of Mtb and other mycobacteria red. Although this design is optimized for Auramine O, it would be advantageous if the design were to image both emission peaks of Acridine O simultaneously without the need to refocus for different wavelengths.

4.1.2. Lens material

The lens material is limited to optical grade plastic, since plastic is lighter and cheaper than glass. The doublets are bonded with Norland Optical Adhesive 61 (NOA61). Some plastics can be machined into lenses in a single step diamond turning process for rapid prototyping or molded by injection molding for mass production. Zeonex and polystyrene are lightweight, low cost, and low auto-fluorescence plastic materials that are both diamond turnable. These two plastics also have complementary dispersion and refractive indices so they can be used to correct for chromatic aberrations [19].

4.1.3. Numerical aperture (NA)

The NA is possibly the most sensitive design parameter of the miniature objective in terms of the difficulty of the design. Based on a review of literature describing the sensitivity of direct FSSM and computer algorithm enhanced FSSM, numerical apertures from 0.4 to 0.55 have been shown to provide diagnostically useful images resolution [8,43]. Increasing numerical aperture allows better optical

resolution and the collection of more light, but introduces more optical aberrations, which causes blurring if not properly corrected. Correcting higher levels of aberrations that come with higher numerical aperture complicates the design process and may not be possible within the size constraints necessary for array microscopy. For this reason, the numerical should not be made arbitrarily large. Therefore, the final design NA should fall within the range established by prior studies in FSSM.

4.1.4. Image detector format and optical magnification

The magnification is limited by the choice of detector, which is limited by what is commercially available. Currently, DSLR cameras are the best commercially available cameras. These cameras typically have ~20 megapixels (MPs) and a full frame chip size (24 mm × 36 mm). The magnification needs to be large enough so that small details in the smear are captured by several pixels. Otherwise the image will appear pixilated and the microscopist will not be able to render a diagnosis from the digital image. For a Canon EOS Mark II DSLR camera, whose specifications are listed in Table 4.1, the minimum magnification needed in order to satisfy the Nyquist sampling criterion with a sample spacing of 8.87μm is 50x. 8.87 μm is the spacing of the green pixels. The importance of the green pixels is that the designed contrast agent, Auramine O, stains AFB green, so the blue pixels pick up substantially less signal while the red pixels pick up almost none at all (Figure 4.2). The designed magnification should be slightly higher than 50x, but not much larger, because higher magnification limits the field of view. There are other commercially

available DSLRs with slightly different specifications, but most are similar the Canon EOS Mark II.

With Acridine O, signal falls predominantly on red pixels, with a small amount of signal found in green pixels. Almost no signal is found in blue pixels (Figure 4.3). The red pixels are spaced 12.54 μm apart, fewer red pixels are sampled than green pixels. When sampled at Nyquist for green pixels, the red channel can have aliasing in the higher spatial frequencies of the image. Fewer samples also leads to lower signal to noise ratio. Green dyes are therefore more optimal for use with red, green, and blue pixel (RGB) cameras than red dyes. Nonetheless, the optical system should accommodate dyes of any color, so long as they are not broadband dyes.

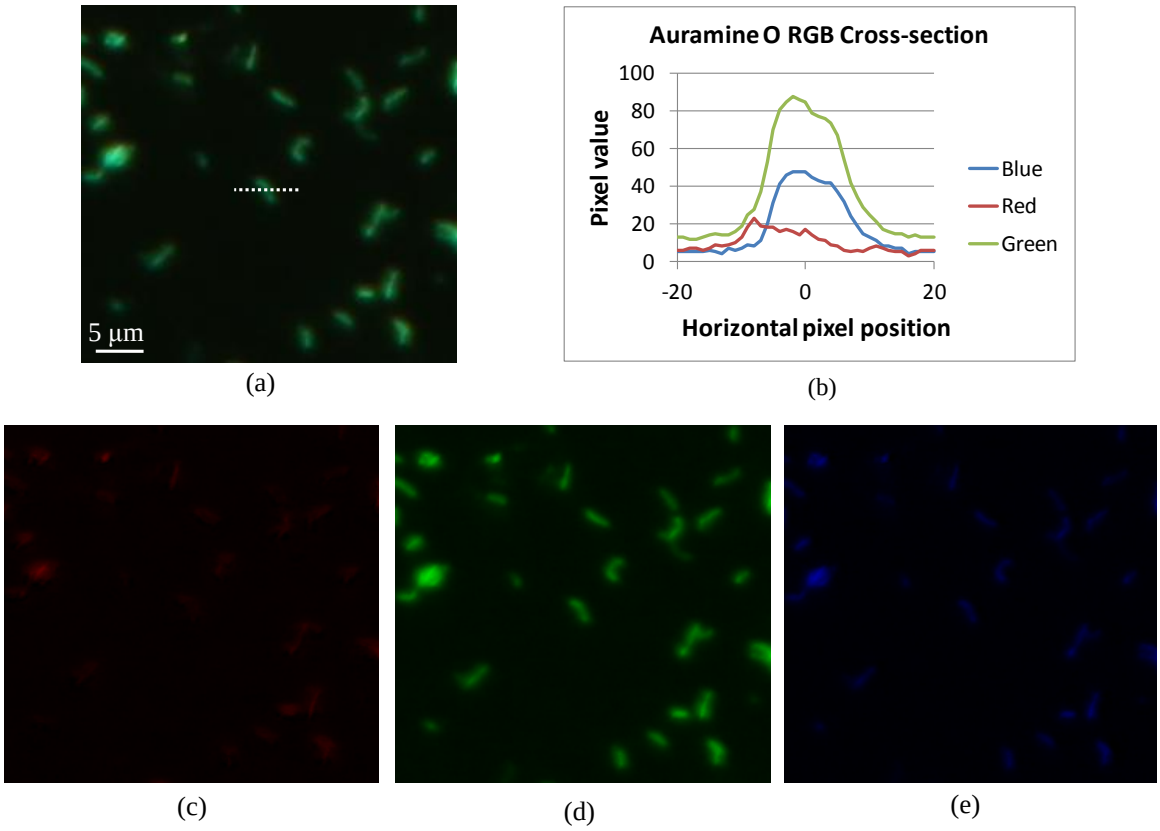

Figure 4.2. (a) Image of AFB stained with Auramine O taken at 40x magnification. (b) Cross section of RGB pixel values from (a) indicated by dotted white line. (c-e) Images of red, green, and blue channels, respectively, from (a).

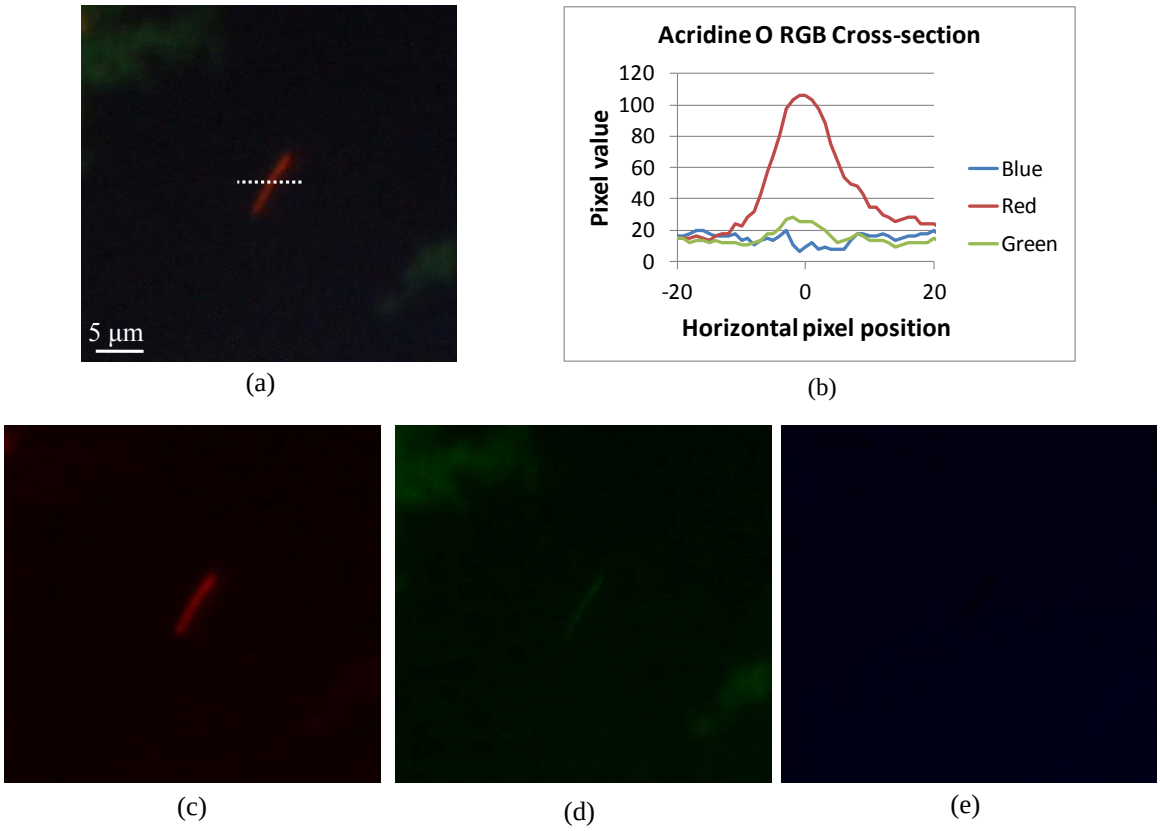

Figure 4.3. (a) Image of AFB stained with Acridine O taken at 63x magnification. (b) Cross section of RGB pixel values from (a) indicated by dotted white line. (c-e) Images of red, green, and blue channels, respectively, from (a).

4.1.5. Outer diameter and field of view

The outer diameter and field of view of a microscope are typically determined by its intended application and are independent of each other. In array microscopy, the outer dimensions of the lens array are loosely controlled by the outer dimensions of the sputum smear, which is typically 20 mm x 30 mm, and the total field of view imaged by the lens array must add up to 3 mm^2 [21]. These are not direct specifications of outer diameter and field of view, however, and the outer diameter of the lens design actually affects how much field of view falls onto the

detector. This means that these parameters are not independent, and are in fact conflicting. Reducing aberrations at the edge of the field of view can often be done by increasing the outer diameter, but increasing outer diameter increases the spacing between lenses and results in less total area imaged onto the CCD of the DSLR. Therefore, these two parameters need to be chosen carefully so that the performance of the lens is diffraction limited over the entire designed field of view and so that the total area imaged meets the requirements of FSSM given the size of the sputum smear, the magnification chosen, and the size of the sensor.

An algorithm for calculating the total area imaged given the magnification, sensor dimensions, and the spacing of the lenses (pitch) is included in Appendix A. The pitch of the lens array must be larger than the clear aperture diameter. It must have enough extra room for a diamond tool to cut between the lenses. While the exact amount of extra spacing needed depends on the slope at the edge of the lenses, the rule of thumb for this design was that the clear aperture diameter should be approximately 90% of the pitch or less. The algorithm could be implemented in Zemax® (Redmond, WA) and included in the merit function for optimization, letting field of view and lens diameter become free variables. This would require the use of a macro, however, and would greatly slow down the optimization process. Instead, the total area imaged for a range of combinations was computed offline and used as a reference to guide the selection of a field of view and clear aperture diameter size (Figure 4.4). Lens designs were attempted starting with a 3 mm diameter. As lens diameter was found to be the limiting factor in the lens design, this parameter was allowed to increase, while also increasing the field of view by the necessary amount.

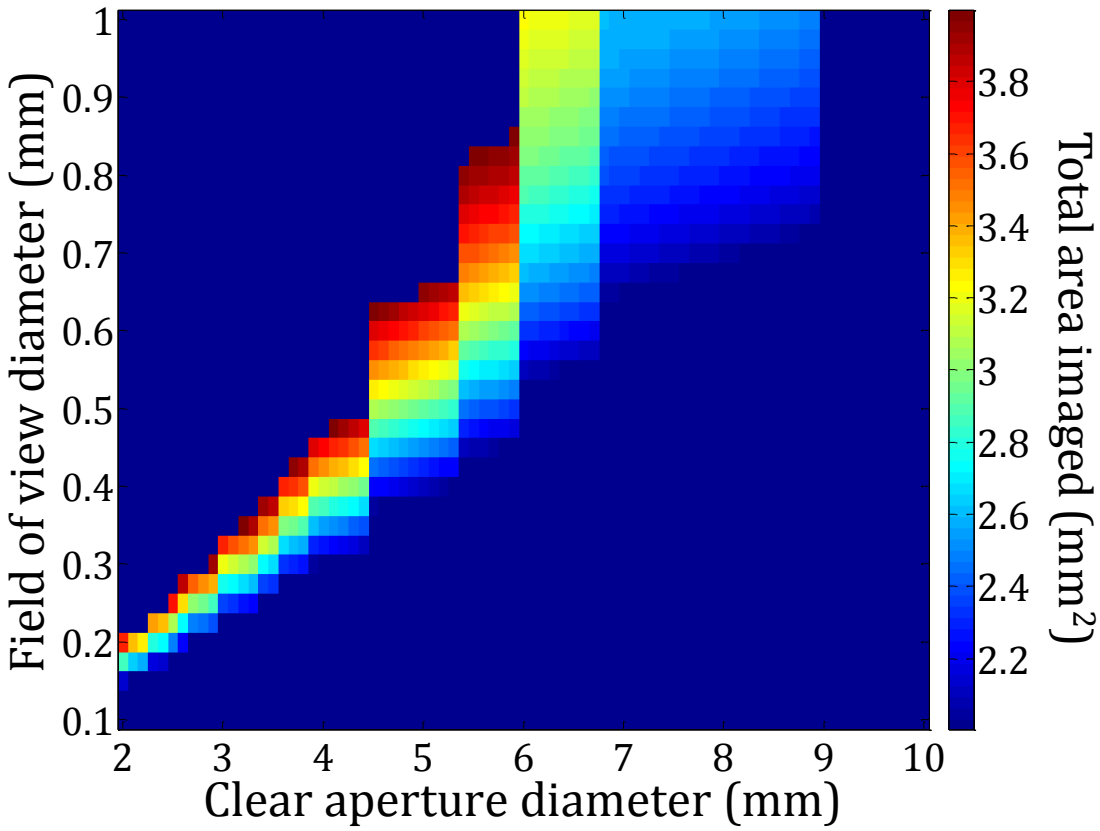

Figure 4.4. Total area imaged versus field of view and clear aperture diameter.

4.1.6. Other design considerations

Other general requirements of the lens design are that the system be diffraction limited, and be easy to use and easy to assemble. Easy to use is fairly vague, but a lens will certainly not be easy to use if it must be aligned manually or if the lenses are too thin to handle during fabrication and assembly. Self-aligning features are not a major concern in the design process, but thickness is. Prior experience with plastic lens fabrication has shown that 2 mm thick plastic substrates do not bend easily. Similar experience led to the adoption of a 50° limit on the edge slope of a lens. A cover slip on the smear or a thin glass cover on the

front lens also makes the microscope array easier to use since the plastic lenses will be protected from sputum and debris. Glass is easier to wipe clean without damaging the optics than plastic. Lastly, an objective that is telecentric is easier to focus as the apparent magnification of the image does not change as the focus is adjusted.

4.1.7. First order system specifications

Based on these general constraints and trial and error techniques, a set of specific first order parameters were chosen, which are shown below in Table 4.3.

Table 4.3. Optical system specifications.

NA	0.5
Magnification	63x
Outer diameter	5.4 mm
Pitch	5.9 mm
Field of view diameter	0.54 mm
Total area imaged	3.10 mm^2
Minimum thickness	2 mm
Maximum edge slope	50°
Primary wavelength	516 nm
Working distance	0.42 mm
Entrance pupil location	Infinity
Cover slip correction	0.17 mm
Back working distance	32 cm
Lens material	Zeonex, polystyrene

4.2. Lens design and theoretical evaluation

A lens design restricted by these constraints was optimized using Zemax® lens design software (Redmond, WA) using a combination of automatic optimization and manual guidance.

4.2.1. Lens prescription and layout

The lens prescription data of the designed objective is presented in Table 4.4. The 4^{th}-8^{th} order coefficients of even aspheric surfaces are given in Table 4.5. The design consists of three elements, including 2 doublets, for a total of five lenses. In the design, the cover glass is over the object, but can be moved instead to the surface of the first lens without changing the ray aberrations in any way. A layout of the design and ray trace for a few selected field points are shown in Figure 4.5.

Table 4.4. Lens prescription data for the miniature objective designed for fluorescence array microscopy detection of Mtb, including emission and cover glass.

Surf	Radius	Thickness	Material	Diameter	Conic
C0VER		0.17	BK7	0.54	
1		0.51		0.66	
2	-1.80	2.57	480R	1.14	
3	-2.36	0.14		3.16	
4	5.83	3.56	480R	3.79	-2.22
5	-1.77	0.03	NOA61	4.15	-1.67
6	-1.80	2.20	POLYSTYR	4.15	-1.68
7	-21.93	0.53		4.83	-73.55
8	13.08	5.04	480R	5.04	
9	-11.88	0.03	NOA61	5.17	10.33
10	-11.88	2.20	POLYSTYR	5.18	10.21
STOP	-13.23	2.00		5.38	
FILTER		2.00	BOROFLOAT	5.50	
13		331		5.61	
IMAGE				34.0	

Table 4.5. 4th to 8th order coefficients of even aspheres of the lens prescribed in Table 4.4.

Surf	A4	A6	A8
3	2.453e-4	-6.665e-4	4.128e-5
4		-3.389e-4	5.877e-5
7		-1.099e-4	1.012e-5
8	-7.147e-4	2.494e-5	1.956e-6
*11	2.905e-4	1.767e-5	-5.590e-7

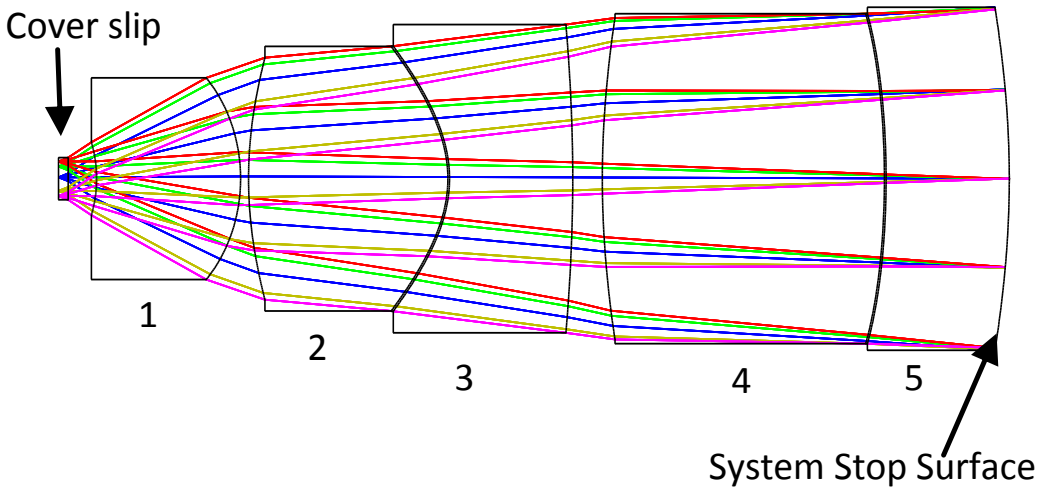

Figure 4.5. Lens design layout and ray path for an individual system within the microscope array.

4.2.2. Predicted nominal performance

The nominal performance of the lens design is characterized in Zemax by calculating the modulation transfer function (MTF), the Strehl ratio, and the full width at half maximum (FWHM) of the point spread function (PSF) at various field

points. The MTF is the amount of contrast that can be seen in images of period waves normalized to the zero frequency. The PSF is the distribution of energy at the detector plane of the image of a unit point source, and it varies from one field point to the next. The Strehl ratio is the ratio of the peak intensity of the nominal PSF to the peak intensity of an Airy disc, the ideal PSF for a circular aperture, of a perfect lens with the same NA as the designed lens. The MTF for several field points and the PSF cross section at the center and edge of the field of view are shown in Figure 4.6.

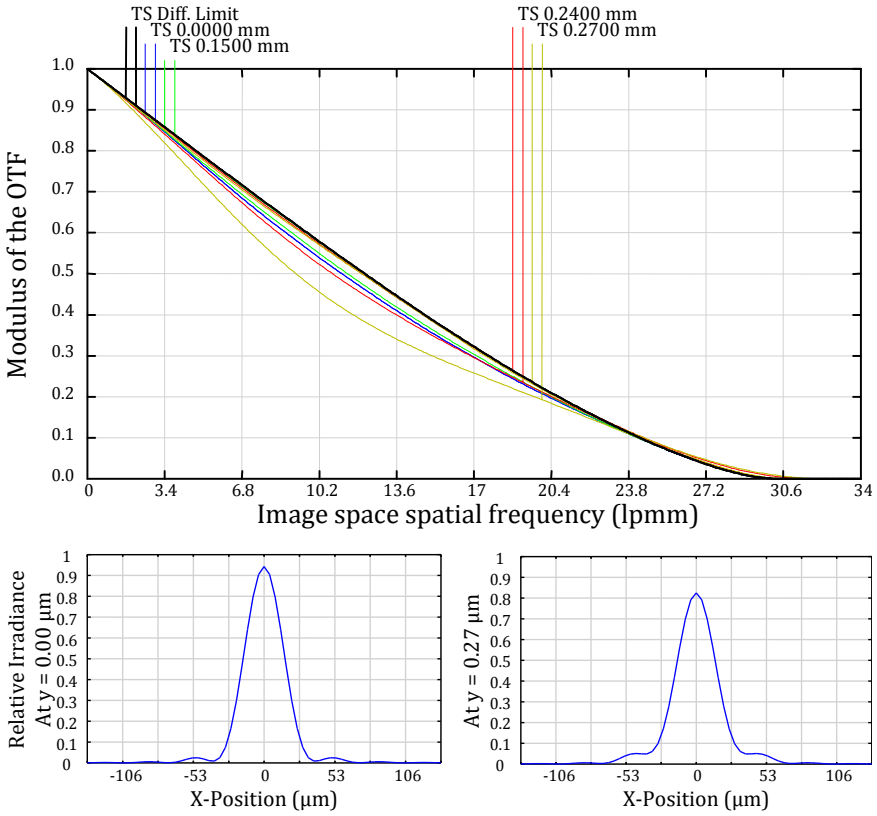

Figure 4.6. Predicted performance of lens design. (Top) MTF at selected image points (Bottom left) Huygen's PSF at the center of the field. (Bottom right) Huygen's PSF at edge of the field.

All of the MTF curves are close to the diffraction limited MTF for an ideal lens (black curve). The PSFs show that the FWHM would be 42 µm at the center of the

FOV and 48 μm near the edge. At 63x magnification, this corresponds to an optical resolution of 0.67 μm and 0.76 μm, respectively, of the sputum smear. The lower limit on the optical resolution due to diffraction is 0.63 μm. A system is considered diffraction limited if the root mean square (RMS) wavefront error is less than λ/14 (0.071λ.). As shown in Figure 4.7, the wavefront error of the design is expected to fall below the diffraction limit over the entire range of the field.

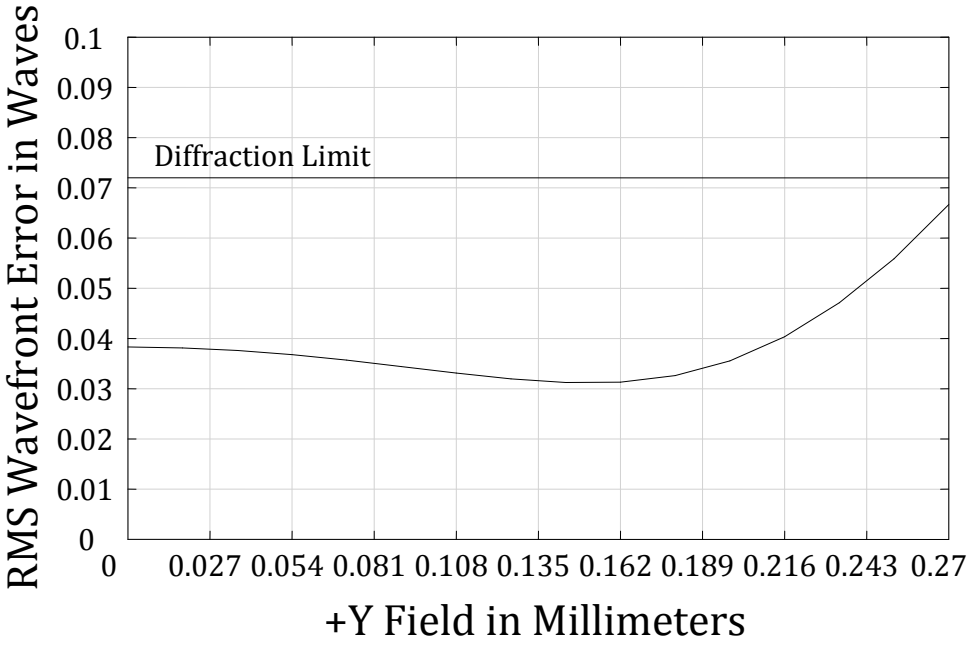

Figure 4.7. Nominal RMS wavefront error of lens design.

4.2.3. Chromatic performance

The diffraction limited depth of field in the image conjugate of this lens design is 8.0 mm. The axial chromatic shift in the image conjugate for the designed wavelengths covers a range of 3.2 mm, well within the range of the chromatic focal shift. On the red side of the designed bandwidth, where the emission peak of

Acridine O associated with mycolic acid lies, the axial chromatic dispersion is very narrow. From 600 nm to 750 nm, there is less than 1 mm of axial chromatic shift in the image conjugate. Because of the narrow dispersion at longer wavelengths, there is an optimal focal point that brings both emission peaks of Acridine O. into focus simultaneously.

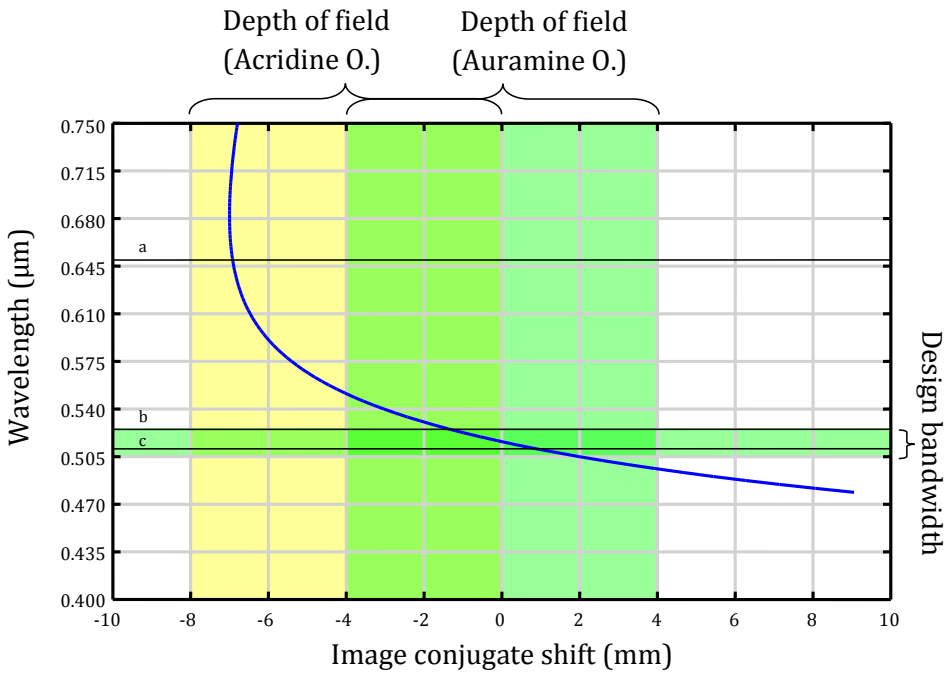

[a] – Peak emission of Acridine O. when associated with RNA
[b] – Peak emission of Acridine O. at ambient pH
[c] – Peak emission of Auramine O.

Figure 4.8. Axial chromatic shift in image conjugate vs wavelength compared to the design bandwidth (506 nm – 527 nm), the peak emissions of Auramine O. and Acridine O., and the depth of field (±4.0 mm).

4.2.4. Tolerance analysis

The lens needs to be tolerant to the fabrication errors that can be expected from fabrication. It is assumed that a sufficiently optimized diamond machining

process can match the same tolerances achievable with single point diamond turning, since the surface and positional measurements are made with the same tools. With reasonable effort and the use of sub-micron positional measurement tools and alignment features, the errors in diamond turning technology can be kept very small. The tolerances expected for the lens fabrication process used to fabricate the designed lens are listed in Table 4.6.

Table 4.6. Single point diamond turning tolerances.

Error	Limit
Radius	±0.5%
Surface Decentration	10 μm
Surface TIR[a]	40 μm
Surface Irregularity	36 nm
Lens thickness	±10 μm
Lens spacing	±10 μm

[a] – Total Indicator Runout, a measure of tilt

The primary merit function (Φ) used in the lens design was the RMS wavefront error averaged over the entire field of view. Nominally, this figure of merit is 0.0457 waves. A root-sum-square (RSS) tolerance analysis is the fastest and easiest to perform. In this analysis, each tolerance, i, is applied to each lens, j, one at a time, and the change in the merit function, $\Delta\Phi_{i,j}$, is computed. The front and back working distances are allowed to be adjusted in order to find the best image conjugate at the designed magnification before $\Delta\Phi_{i,j}$ is computed. The RSS of the changes is computed and added to the nominal merit function to find the expected merit function after fabricating the lens. The results of this analysis are shown in Table 4.7.

Table 4.7. Expected performance based on RSS tolerance analysis. λ = 0.52.

Nominal Φ	0.0461λ
RSS(ΔΦi,j)	0.0279λ
Expected Φ	0.0740λ

This analysis does not predict diffraction limited performance. A Monte Carlo simulation provides a more detailed look at the expected range of Φ. In each Monte Carlo trial, each lens is randomly perturbed according to the expected tolerances, which are assumed to be normally distributed with limits of ±3σ. Two thousand (2,000) of these simulations were run. As in the RSS tolerance analysis, the front and back working distances are adjusted to find the optimal image conjugate at the designed magnification. The result of this simulation is an estimate of the cumulative density function (CDF) of the perturbed lens wavefront error, shown in Figure 4.9. This analysis predicts that 83% of lenses fabricated with the tolerances listed in Table 4.6 will have an average RMS wavefront error of 0.071λ or less.

Another smaller Monte Carlo simulation was run to see how the RMS wavefront error can be expected to vary across the field. Figure 4.10 shows that nearly all lenses even when perturbed with the expected fabrication errors will have diffraction limited performance over a 0.38 mm diameter field of view. Furthermore, it is likely that the aberrations at the edge of the field of view will be no worse than 0.1λ.

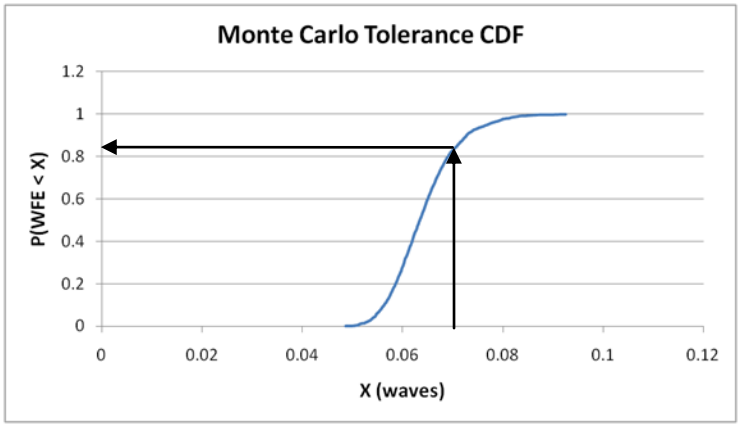

Figure 4.9. CDF of perturbed lens wavefront error estimated by Monte Carlo analysis.

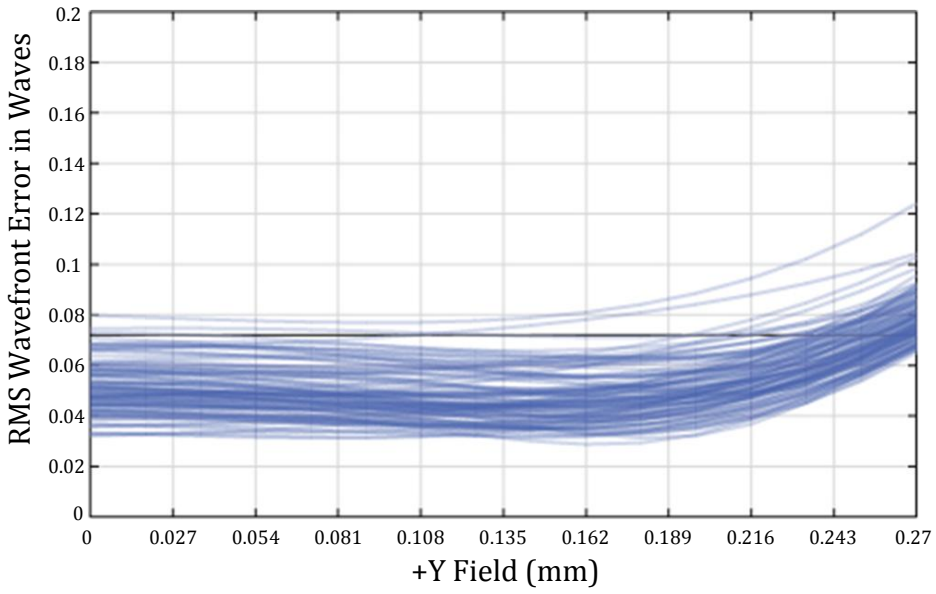

Figure 4.10. Monte Carlo simulations of RMS wavefront error vs field. Each curve represents the RMS vs field of one simulated perturbed lens.

4.1. Conclusions

An “all plastic lens” has been designed that meets the imaging criteria for FSSM. This lens is expected to resolve sub-micron features in AFB slides as small as 0.67 μm at the center of the field of view and 0.76 μm at the edge. With this lens

fabricated in a 4 × 6 array, a total area of 3.10 mm^2 will be imaged onto a DSLR camera at 63x magnification. The area imaged is sufficient for sensitive detection of Mtb, and the magnification is sufficient to avoid aliasing. The image quality over the entire field of view is diffraction limited. The axial chromatic image conjugate shift is within the diffraction limited depth of field for the designed wavelengths of Auramine O. In addition, the emission peaks of Acridine O both fall within a diffraction limited depth of field that is slightly offset from the designed image conjugate. Taking into account reasonable fabrication errors, it is nearly certain that the performance will be diffraction limited over 64% of the field of view, which would cover 1.98 mm^2. It is likely (83% chance) that the image quality averaged over the entire field of view will be diffraction limited. With this level of tolerance, there is a high likelihood that these lenses can be successfully fabricated if single point diamond turning tolerances can be met in an array fabrication process.

Chapter 5

Evaluation of prototype miniature objective designed for array microscope

A prototype of the miniature objective designed in Specific Aim 1 was fabricated as a single lens prototype in order to validate the lens design and the tolerances of diamond machining. The prototype objective was fabricated using single point diamond turning (SPDT). A test platform was built to validate the high resolution and image performance of the miniature objective. The sub-micron resolution of the objective was demonstrated, the image quality of the prototype was compared to that of a standard clinical fluorescence microscope, and the diagnostic value of digital images obtained with the prototype miniature objective was compared to standard FSSM. Detection of Mtb using the prototype miniature objective in this evaluation platform was found to be highly concordant with

standard FSSM, indicating that an array microscope based on this design can detect Mtb with high sensitivity and specificity.

These experiments and their results will be published in an upcoming issue of *Archives of Pathology & Laboratory Medicine* [41].

5.1. Prototype and test platform

The prototype miniature objective was fabricated using SPDT. A single objective was fabricated in 1.5" disks of plastic with alignment features built directly into same component as the lenses. These features are complementary bumps and grooves cut in a ring around the lenses (Figure 5.1). Although the disks are 1.5" in diameter, size of the objective is much smaller than a 40x/0.65 NA Zeiss Primo Star objective. The clear aperture diameter of the microscope objective limits the lens spacing. At 5.4 mm, with a 5.9 mm wide fillet around the lens, up to four of these microscope objectives can fit within the width of a single microscope slide, as shown in Figure 5.2. Only one Primo Star objective fits within the same width.

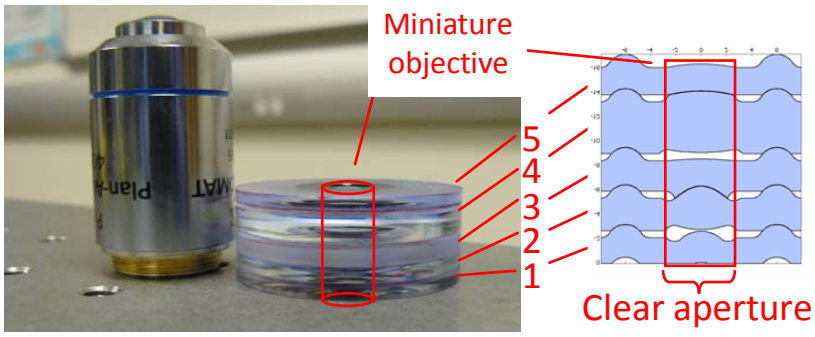

Figure 5.1. Plastic miniature objective for FSSM (right) compared to the Zeiss PrimoStar (left) also designed for FSSM capabilities. The lenses are cut into disks along with self-aligning features. No expertise is required in order to assemble the lenses.

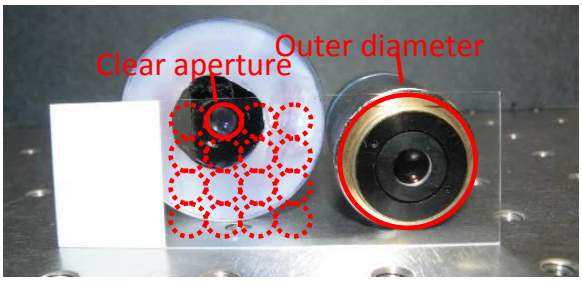

Figure 5.2. Multiple miniature objectives can be fabricated into the same disks. The spacing is limited by the clear aperture of the lens. Up to 4 miniature plastic objectives can fit over the width of a microscope slide.

The test platform used to evaluate the miniature objective is shown in Figure 5.3. This platform consists of a modified Zeiss® Primo Star™ lab microscope, a Canon® EOS 5D Mark II DSLR camera with a universal serial bus (USB) connection to a laptop, a high resolution monitor, Thorlabs opto-mechanics, and custom 3D printed parts. Not all of these components are expected to be used in a low-cost point of care diagnostic with the array microscope, but in this evaluation these tools facilitate troubleshooting unknown or unanticipated problems in evaluating the first

prototype of an all-plastic miniature lens designed for digital FSSM. This Primo Star microscope includes a blue (455 nm wavelength) LED for epi-fluorescence illumination and a white light LED for brightfield illumination in transmission. A collector lens and filter set for fluorescent microscopy sit above the Primo Star's turret with the objective acting as the condenser. Another pair of collector and condenser lenses are included beneath the microscope stage for bright field illumination. The prototype objective was mounted to the turret of the Primo Star microscope by a 3D printed lens holder. Another 3D printed component allows Thorlabs 1 inch cage pieces to sit in the port normally used to seat the Primo Star's binocular or trinocular. The DSLR camera was then attached to the Thorlabs SM2 tubes at the other end with a 3D printed bayonet mount. A second Primo Star microscope was used for standard FSSM in these evaluations, so that the test platform did not need to be disassembled and reassembled when switching from standard to digital FSSM and back.

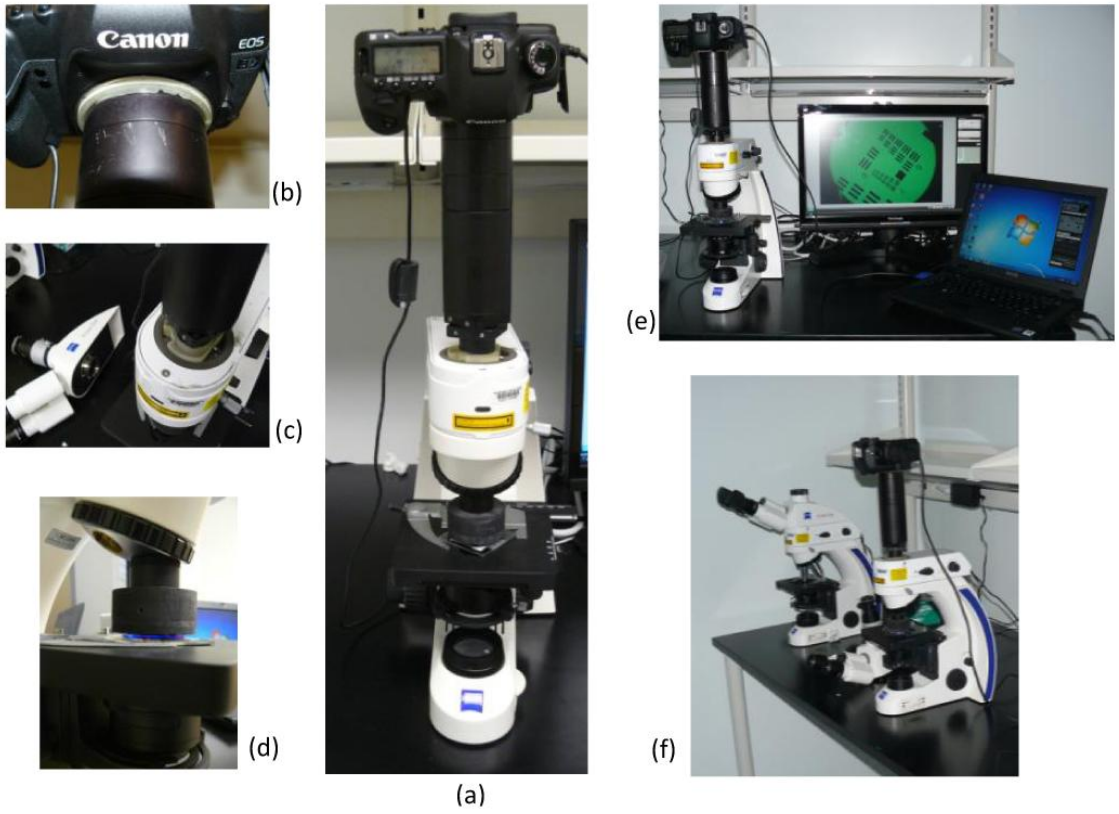

Figure 5.3. (a) Modified Zeiss Primo Star lab microscope used to evaluate the prototype miniature objective. (b) A 3D printed bayonet glued to a Thorlabs SM2 tube holds the Canon EOS 5D Mark II DSLR camera in place. (c) The Thorlabs tube assembly was glued to another 3D printed component that takes the place of the Primo Star trinocular mount. (d) A 3D printed lens holder was fixed to a Thorlabs SM1 tube with an SM1 to RMS thread adapter, which screws into the Primo Star turret. (e) Canon EOS Utilities controlling the camera via USB. The EOS utilities had a Remote Live View function which is useful for bringing objects into focus and navigating fields of view. (f) The evaluation system was used for digital FSSM while another unmodified Zeiss Primo Star microscope was used for standard FSSM.

5.2. Imaging performance

5.2.1. Sub-micron resolution

The high resolving capability of this objective was demonstrated by imaging an Edmund Optics® Hi-Resolution 1951 US Air Force target. A strip of paper covered in fluorescent highlighter ink was placed beneath the target. The test platform Primo Star's illumination mode was set to epi-fluorescence. In this configuration, the illumination light passed through the transparent portion of the target and excited the fluorescent highlighter ink behind it. The image formed on the CCD of the DSLR was the transmission of the fluorescent light emitted by the highlighter ink passing back through the resolution target. Element 3 of Group 9 is the smallest element on this target (Figure 5.4). The feature size of this element is 645 line pairs per millimeter (lpmm), which corresponds to a line pair width of 1.55 μm and a line width of 0.775 μm. This feature is clearly resolved by the prototype objective, as shown in Figure 5.4.

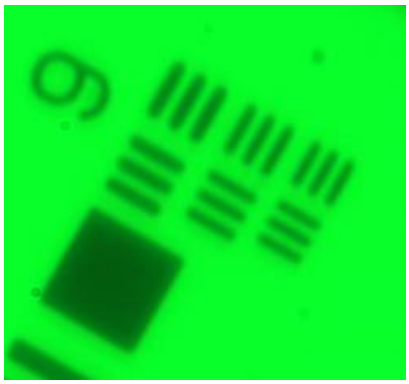

Figure 5.4. Image of a Hi-Resolution target taken with the prototype objective (63x magnification) for the microscope array. Group 9 Element 3 has a line width of 0.775 µm.

5.2.1. Qualitative comparison with Zeiss Primo Star

The ability of the objective to resolve 0.775 µm line-width features on a resolution target is promising, but the Mtb in the smears that will be examined with this microscope can be as little as 0.1 µm wide and 1 µm long. The next test of imaging performance for the prototype was to take digital images of AFB and compare these images to digital images of the same field of view taken with a Zeiss Primo Star 40x/0.65 NA objective. The Primo Star objectives were designed to meet the needs of FSSM examination, so a comparison of images recorded with both objectives is a practical test of the resolution of the prototype miniature objective. The sample imaged for this purpose was a Becton-Dickinson (BD) AFB test slide stained with Auramine O. The camera sensitivity (ISO) setting used for these images was ISO 400. A 0.25 second exposure time was used to capture the image with the 40x Primo Star objective, and a 0.5 second exposure time was used to capture the image with the prototype objective. Those images are shown in Figure 5.5.

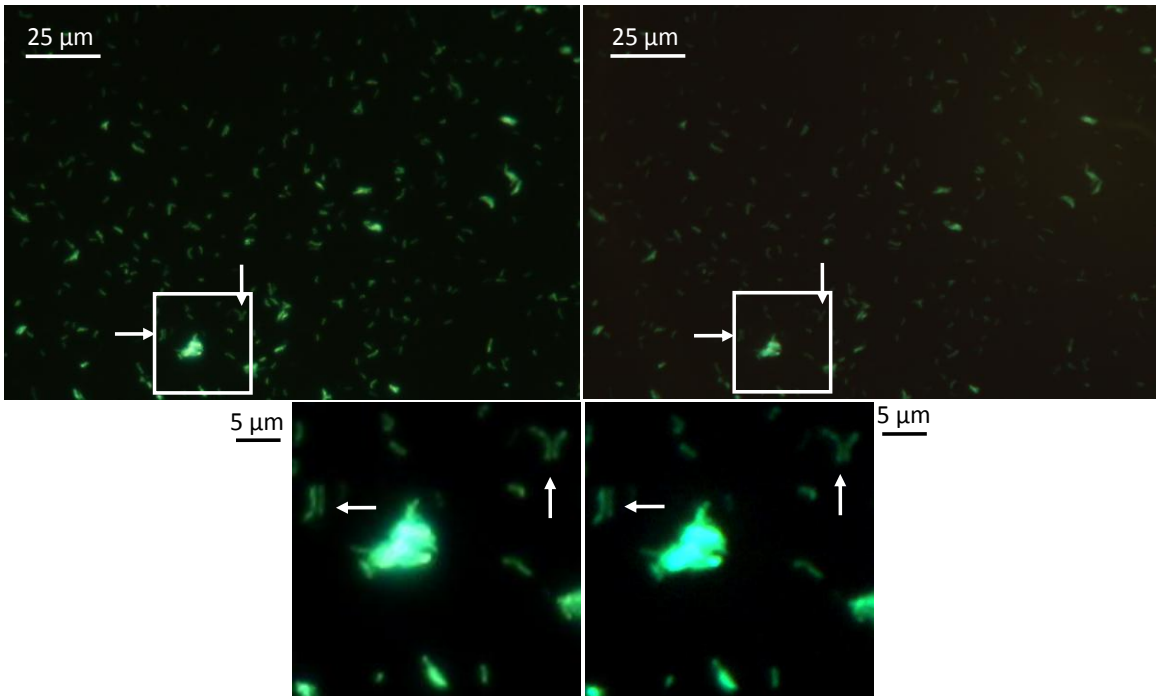

Figure 5.5. Image of an AFB test slide stained with Aruamine O and a digitally zoomed in region of interest using (left) a Zeiss Primo Star® 40x, 0.65 NA objective and (right) the prototype 63x, 0.5 NA miniature array objective. The inset on the left is contrast stretched with a 1.5x gain in brightness. The inset on the right is contrast stretched with a 3x gain in brightness.

A longer exposure time was used with the prototype miniature objective because it generates less signal than the Primo Star objective. With a lower NA, the prototype objective delivers less excitation light and collects less emission light than the 40x objective. With higher magnification, the prototype objective spreads light out more in the image than the light from the Primo Star objective. The signal level picked up with the Zeiss microscope is higher than the prototype objective, despite the compensation in exposure time, and there is more background light in the image of the prototype. When background is removed and brightness is equalized, Figure 5.5 shows that images of the same field of view taken with the two microscope

objectives are nearly indistinguishable. In the insets of Figure 5.5, there are two pairs of AFB that are separated by less than 1 μm lengthwise, and the detail is just as clear in the image recorded with the prototype objective as it is with the Zeiss objective.

5.2.2. Imaging clinical specimens

To demonstrate the objective's ability to capture high quality images of clinical specimen, patient samples stained with Acridine O using the standard fluorochrome staining procedure of The Methodist Hospital (TMH) microbiology laboratory [24] and imaged using the prototype objective. Blinded samples were obtained from TMH according to protocol IRB0511-0077 approved by The Methodist Hospital Research Institute (TMHRI) Institutional Review Board (IRB) and protocol 12-050E-Tkaczyk approved by the Rice University IRB.

When stained with Acridine O, the background stain in the smear appears green while the AFB appear red. The signal levels from this dye used with patient samples was much lower than the BD AFB test slides stained with Auramine O, so longer exposure time or higher sensitivity (higher ISO setting) was needed to increase the dynamic range of the image. Increasing the ISO setting or increasing exposure time increases the level of background light seen in the images. Increasing exposure time is preferable to increasing the ISO setting because increasing exposure time yields a higher signal to noise level. A 5 second exposure time was found to be optimal. At 6 seconds, objects of interest begin to saturate pixels. At 5 seconds, there was no saturation in objects of interest, and some organisms were

bright enough to be distinguished from the background (Figure 5.6). Organisms can be difficult to find in large fields of view at low contrast, however.

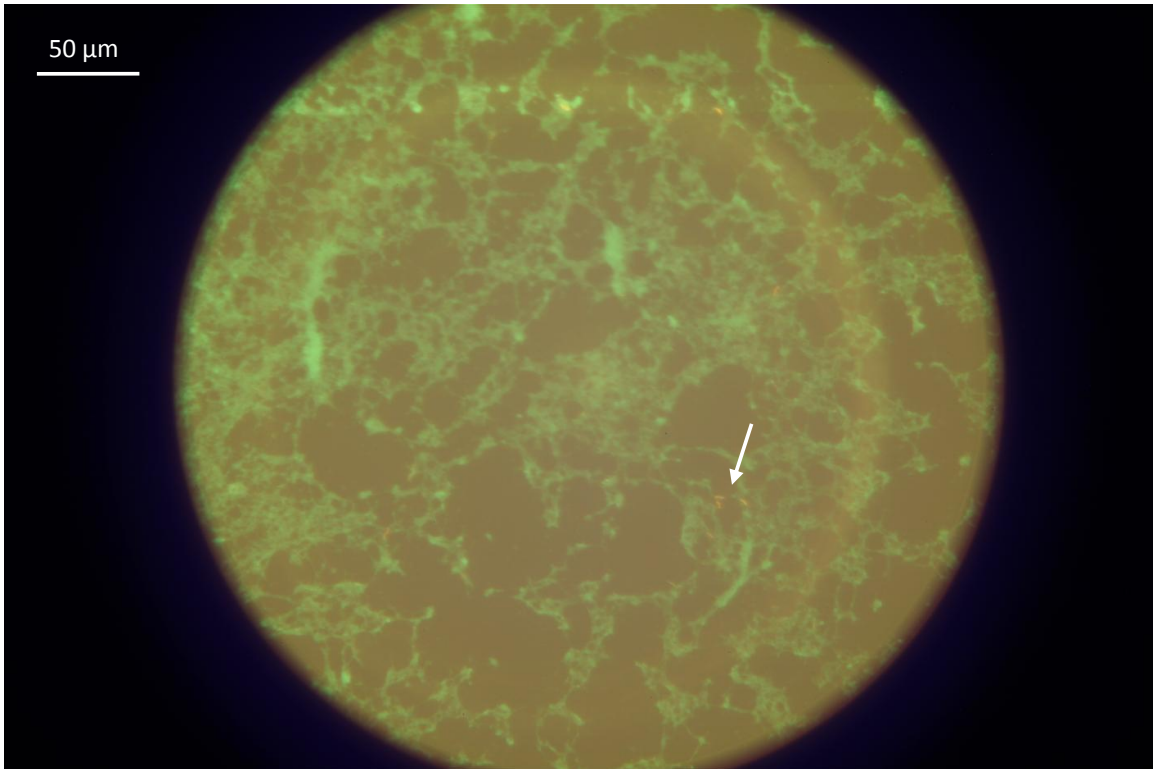

Figure 5.6. Digital image of a patient sample without enhancements. The arrow indicates a group of AFB.

Background subtraction increases the contrast of raw images significantly (Figure 5.7). Digital contrast enhancements were then applied to the RGB color channels independently. After background subtraction, the median RGB pixel value was subtracted from the entire image, and the red, green, and blue channels were scaled by factors of 2.6, 0.975, and 0.65 respectively (Figure 5.8). These values were chosen empirically to maximize contrast of the red acid fast stain without saturation while limiting the peak intensity of the green background staining to approximately

half of the peak intensity of the red channel. The same gains were used for all subsequent images in the evaluation of the microscope. As the brightness of the acid fast and background stains varies from one smear to the next, so too does the ratio of peak red intensity to peak green intensity of the enhanced images.

5.3. Quantitative evaluation of diagnostic performance

In the qualitative comparison of the Zeiss and prototype miniature objectives, there is little if any noticeable difference in resolution between the two (Figure 5.5). There are some differences in signal levels and background, giving the images taken with the Zeiss objective have a slightly better appearance, but as shown in Figures 5.7 and 5.8, these differences can be compensated digitally. Therefore a person examining a digital image taken with the miniature prototype objective (digital FSSM) would count all the bacteria that they would have counted by examining the same field of view through the standard clinical microscope (standard FSSM). In order to provide a more quantitative comparison of standard versus digital FSSM, two experiments were conducted focusing on comparing the diagnostic accuracy of these techniques.

(a)

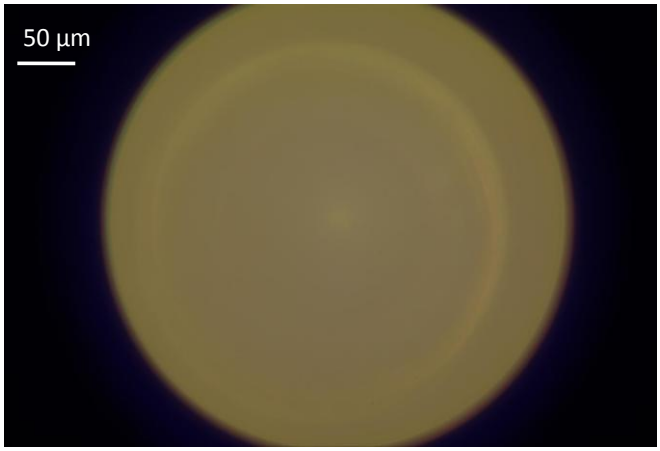

(b)

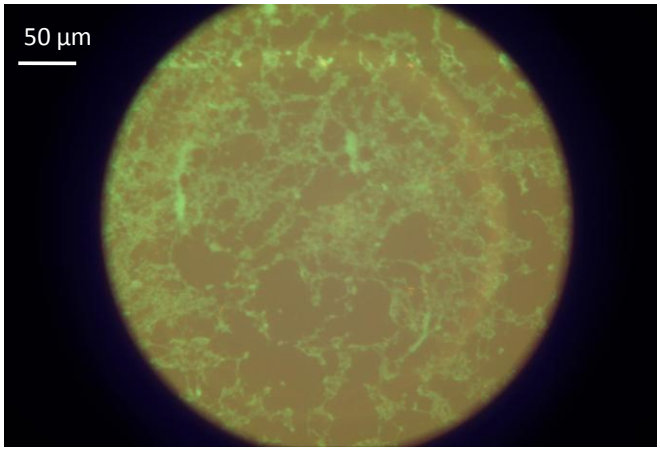

(c)

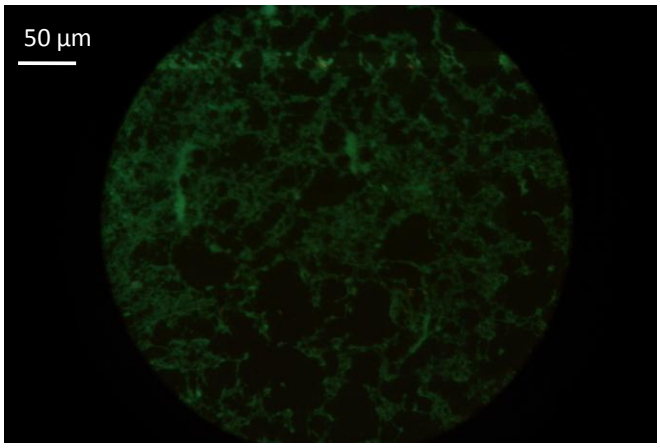

Figure 5.7. (a) Background image taken at 5 s exposure with 400 ISO sensitivity without a sample on the microscope. (b) Image of a patient sputum smear on a reticule with the same exposure and sensitivity settings. (c) Background subtracted from the image of the sample.

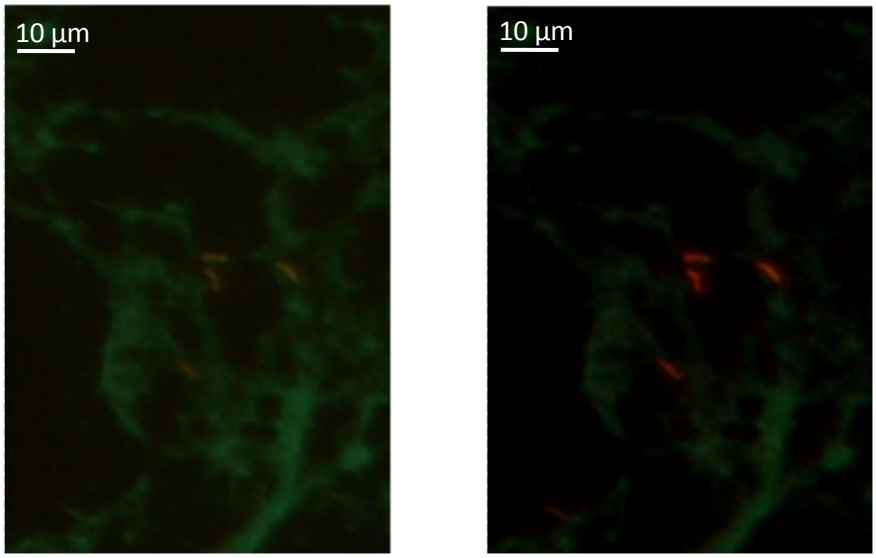

Figure 5.8. (Left) Sub-image from Figure 5.7 after background subtraction. (Right) Same image after subtracting the median pixel and scaling red, green, and blue channels by 2.6, 0.975, and 0.65 respectively.

5.3.1. Counting AFB in matched fields of view

When examining a sputum smear in SSM or FSSM, the procedure involves not only determining whether or not AFB are present, but also the average number of bacteria found per microscopic field [21]. Therefore, it is important to compare the bacterial counts obtained with standard FSSM to the counts obtained using digital FSSM. Two (2) smears were prepared from 2 patient samples at the TMH microbiology laboratory. Both patients had previously been diagnosed as positive by FSSM and confirmed by SSM using a modified Kinyoun stain [24,44]. One patient was reported as 1+ smear positive and the other was reported as 3+ smear positive. An experienced pathologist was recruited to examine both smears using standard FSSM and digital FSSM. The same field of view was counted using both techniques so that the number of counted organisms could be directly compared.

5.3.1.1. Smear preparation

Eyepiece reticules with a 10x10 grid of 100 indexed 1 x 1 mm^2 tiles were used instead of the microscopy slides normally used in the preparation sputum smears [24]. These reticules were placed in custom holders machined out of aluminum that were similar in size to standard microscope slides (Figure 5.9). The reticule slides were not coated with albumin. A drop of concentrated sputum solution was placed in the middle of the reticule and allowed to diffuse across the surface of the slide and strained as previously described.

Figure 5.9. 75mm × 25mm aluminum reticule holder for a 21 mm diameter reticule slide with a 10x10 grid of 1 mm^2 indexed squares.

5.3.1.2. Standard FSSM counting

The pathologist counted the AFB in 10 out of 100 tiles of each reticule using the Zeiss Primo Star clinical microscope at 400x magnification (40x objective, 10x eyepiece). The width of each tile is approximately twice as large as the field of view of the Zeiss Primo Star with the 40x objective, so the tiles were examined in quadrants.

5.3.1.3. Digital FSSM counting

Sixteen to twenty (16-20) overlapping digital images were taken of each tile by another researcher and stitched together using a custom Matlab® script. The enhanced images were down-sampled by a factor of 4 to reduce file size after applying a digital anti-aliasing filter. A complete tile is shown in Figure 5.10. These tiles were examined in Adobe Photoshop CS4 (San Jose, CA) at 100% zoom on a 27" monitor with 2560x1440 screen resolution (620x magnification).

The bacterial counts from standard examination of the sputum samples are shown alongside the counts from the digital images taken with the miniature 63x objective in Tables 5.1 and 5.2. Table 5.1 has the counts for the 1+ smear, and Table 5.2 has the counts for the 3+ smear. The data in these tables are plotted in Figure 5.11 as digital FSSM counts versus standard FSSM counts.

Table 5.1. AFB counts for 10 1×1 mm² tiles of a 1+ sputum sample examined by standard and digital FSSM.

Tile #	36	44	45	46	54	55	64	74	75	76
Standard FSSM counts	29	12	9	5	7	5	5	2	2	3
Digital FSSM counts	59	29	55	46	31	37	17	24	25	53

Table 5.2. AFB counts for 10 1×1 mm² tiles of a 3+ sputum sample examined using by standard and digital FSSM.

Tile #	35	44	45	46	54	55	56	64	65	66
Standard FSSM counts	826	567	532	472	510	620	370	402	390	276
Digital FSSM counts	1051	1191	880	505	1241	952	801	1410	2812	1104

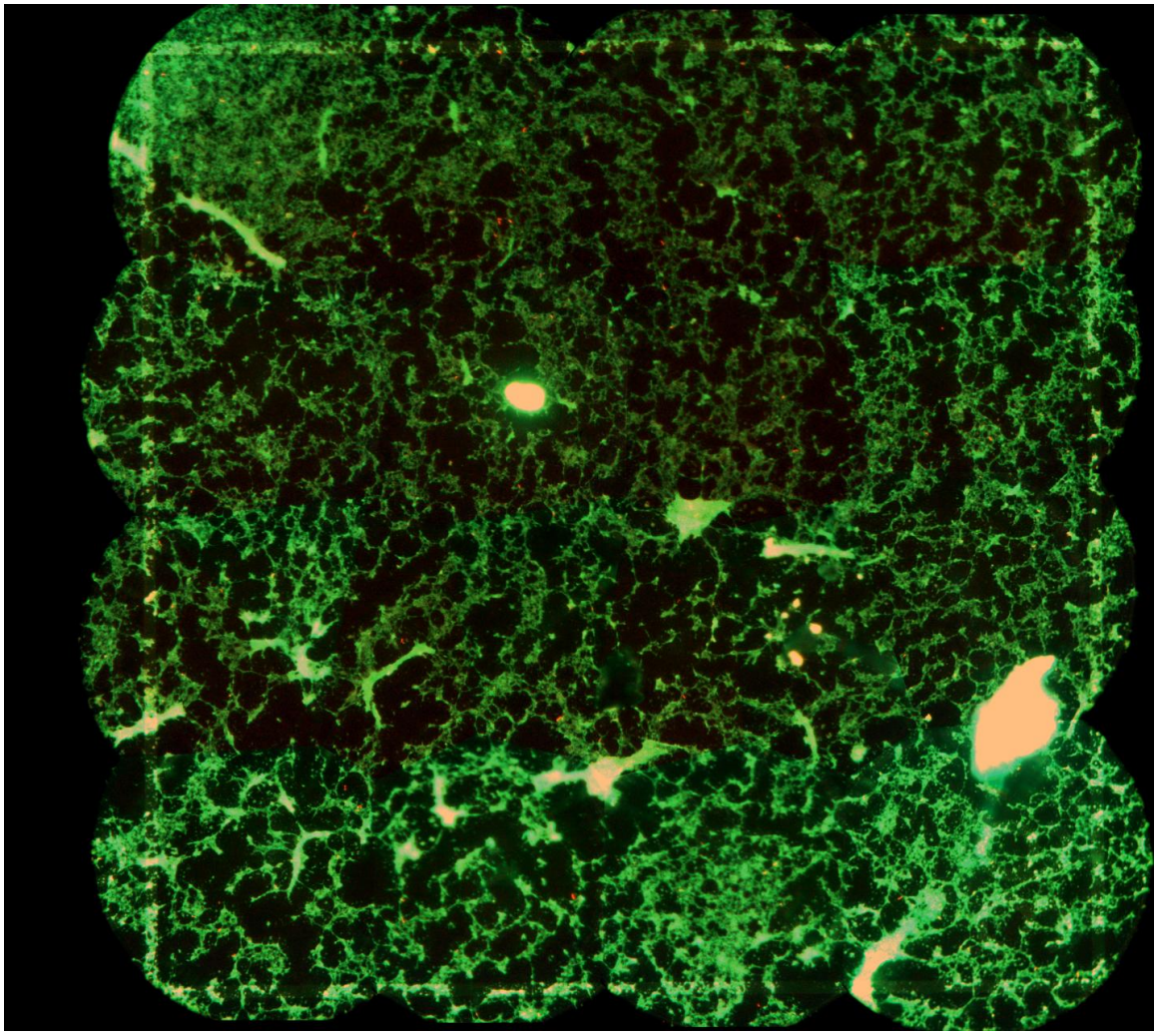

Figure 5.10. An image of a 1 x 1 mm^2 tile within a 10x10 indexed grid of such tiles. This image was stitched together from 16 digital images of overlapping fields of view taken one at a time at 63x magnification with the prototype miniature objective.

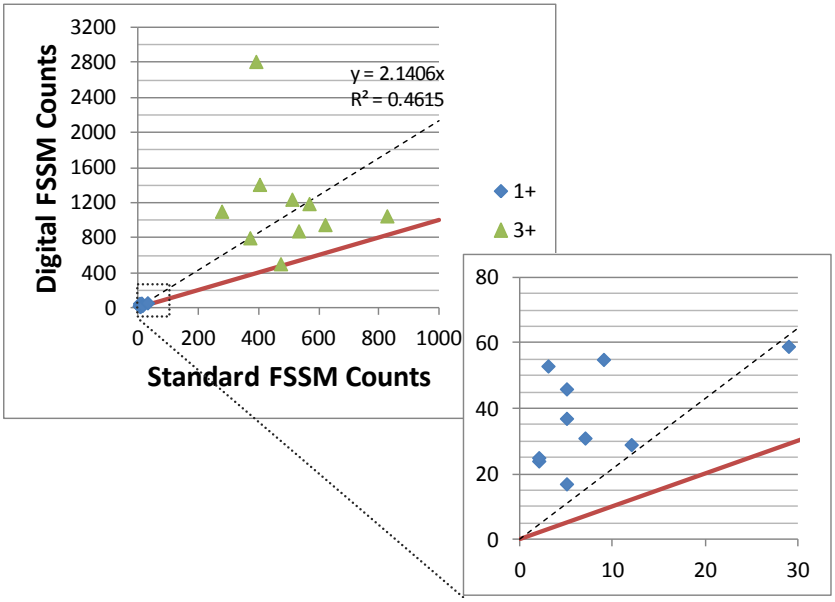

Figure 5.11. Digital FSSM counts vs. standard FSSM counts done by the same pathologist for matched fields of view of a 1+ sputum smear and a 3+ sputum smear. The red line indicates where equivalent counts would lie. All digital FSSM counts are higher than standard FSSM counts. The dashed line is the restricted zero-intercept linear regression line fit to the combined dataset.

The results of this experiment show that digital FSSM counts are higher than standard FSSM counts, whether these counts are compared for each dataset ($p < 0.001$, $p = 0.005$ for 1+ and 3+ datasets respectively) or combined ($p = 0.006$). To test for dependence, the best fit unrestricted linear mode, $y_i = \beta_0 + \beta_1 x_i + e_i$, is compared with the independent model $y = \beta_0 + e_i$, which is a linear model with the restriction $\beta_1 = 0$. In the unrestricted model, the dependent variables, y_i, are the digital FSSM counts and the independent variables, x_i, are the standard FSSM counts. When the datasets are combined, the unrestricted linear model ($\beta_0 = 145$, $\beta_1 = 1.87$, $R^2 = 0.48$) is a significantly better fit than the restricted, independent linear model ($p = 0.00067$). The best fit zero-intercept of this model is positive, which might mean that the specificity of digital FSSM will be poor. This conclusion is not

significant, however, because the unrestricted model is not a significantly better fit than the restricted zero-intercept model ($\beta_0 = 0$, $\beta_1 = 2.14$, $R^2 = 0.46$, $p = 0.57$), and the variance explained by the zero-intercept model (46%) is similar to the variance explained by the unrestricted linear model (48%).

5.3.2. Diagnostic comparisons

The goal of this experiment was to estimate the sensitivity and specificity of a diagnostic examination performed using the miniature objective and digital FSSM and compare the diagnostic performance to standard FSSM. The previous experiment showed that a pathologist may find more organisms on a slide known to be positive by examining digital images. The second experiment required the pathologist to find organisms and distinguish them based on morphology from other debris or organisms that were irregularly shaped or round instead of rod-like. Clinical specimen from 13 patients provided sputum for 40 smears. Three (3) patients provided 6 samples of sputum which were all reported as ss+ by FSSM and SSM. One of the ss+ samples was identified by AFB culture as *Mycobacterium abscessus*, and the other five were identified as *Mycobacterium avium-intracellulare*. Twenty (20) smears were prepared from these six sputum samples for this experiment. The other 10 patients provided 12 sputum samples, which were all reported as ss- by FSSM and SSM. AFB culture results were all negative as well. 20 negative smears were prepared from these 12 negative sputum samples. The experiments were conducted in sets of 8, with 4 positive and 4 negative smears per set. An experimental set size of 8 slides with a 4:4 positive to negative ratio was

chosen to minimize the number of smears originating from the same sample while providing enough samples that relatively few diagnoses would be affected by process of elimination. Two pathologists, blinded to the previous result, examined each smear both using the standard FSSM technique and the digital FSSM technique. The researcher responsible for recording digital images of the smears was also blinded to the previous result. A result of ss+ or ss- was reported for each slide, once for each pathologist's standard FSSM examination, and again for each pathologist's digital FSSM examination. Each experimental set was examined and imaged on different days based on the availability of smears from the TMH Microbiology Lab. Due to scheduling constraints, one pathologist was only available to examine one set. A third pathologist was recruited to examine the other four experimental sets so that each set would be examined by two pathologists. The pathologist who examined smears in the previous experiment was referred to as Dr. A in this experiment. Dr. A examined all 5 sets, Dr. B examined 4 sets, and Dr. C examined 1 set.

5.3.2.1. Smear preparation

Smears for this experiment were prepared according to the standard TMH Microbiology Lab fluorochrome staining protocol with Acridine O [24]. This protocol included the use of standard microscopy slides instead of reticules and the practice of smearing the sputum rather than letting it diffuse, unlike the previous experiment. Without predefined fields of view, there was little chance that the same

field of view could be examined with both standard and digital FSSM, so only sensitivity and specificity were compared in this experiment, not bacterial counts.

5.3.2.2. Diagnostic procedures

As with standard FSSM counting in the previous experiment, the standard FSSM diagnosis was done by the pathologists using the Primo Star with the 40x objective. Before making a negative diagnosis, two lengths of the smear were examined. The total area imaged with two sweeps depended on the smear shape and dimensions, but was approximately 15-20 mm^2. A positive diagnosis was made if any acid fast bacilli (AFB) were found, but the examination continued until at least 50 AFB were counted or two lengths of the smear were examined. A typical standard FSSM examination required less than 10 minutes per smear.

For the digital diagnosis, images were recorded by a technician as in the previous experiment using the same settings and applying the same enhancements. The fields of view were not overlapping however, and the images were not stitched together. Instead they were examined one at a time. Forty to forty-five images were recorded for each slide. The total area imaged by digital FSSM was approximately 7.5-8.4 mm^2. As with standard FSSM, a positive diagnosis was made if any AFB were found. All images were examined unless 50 or more AFB were identified before finishing the set of images. Twenty to thirty minutes were required to capture the digital images for each slide. Processing digital images for each slide required another 15-20 minutes. As with standard FSSM, examining each digital slide required less than 10 minutes by the pathologists. Not all pathologists used the

same computer monitor, so final image magnification varied. Dr. A examined digital images at 620x, Dr. B examined digital images at 590x, and Dr. C examined images at 720x.

5.3.2.3. Results

The sensitivities and specificities of the diagnoses obtained in this experiment were calculated and are tabulated in Table 5.3 for each pathologist using either standard FSSM or digital FSSM. Confidence intervals for each pathologist are shown in Table 5.4. The lower limits on the sensitivities of digital FSSM found for Dr. A and Dr. B were well above 70%, the point at which new point of care diagnostics begin to increase the number of lives saved compared the diagnostics used under the DOTS program [7].

Table 5.3. Sensitivity and specificity of FSSM examination of patient slides. Dr. A examined all 40 slides, Dr. B examined 32 of the slides (16 positive, 16 negative), and Dr. C examined the other 8 (4 positive, 4 negative).

	Dr. A Standard FSSM	Dr. A Digital FSSM	Dr. B Standard FSSM	Dr. B Digital FSSM	Dr. C Standard FSSM	Dr. C Digital FSSM
Sensitivity	90% (18/20)	100% (20/20)	94% (15/16)	100% (16/16)	100% (4/4)	100% (4/4)
Specificity	100% (20/20)	100% (20/20)	94% (15/16)	88% (14/16)	100% (4/4)	100% (4/4)

Table 5.4. Confidence intervals[a] for sensitivity and specificity for each pathologist using either standard or digital FSSM.

	Dr. A Standard FSSM	Dr. A Digital FSSM	Dr. B Standard FSSM	Dr. B Digital FSSM	Dr. C Standard FSSM	Dr. C Digital FSSM
Sensitivity	0.73-0.97	0.86-1.00	0.75-1.00	0.83-1.00	0.47-1.00	0.47-1.00
Specificity	0.86-1.00	0.86-1.00	0.75-1.00	0.67-0.98	0.47-1.00	0.47-1.00

[a] – Exact interval, calculated using F-distribution [45]

A chi-square test of equal proportions was applied to four of these categories for reference positive smears: standard FSSM of by Dr. A, digital FSSM by Dr. A standard FSSM by Dr. B, and digital FSSM by Dr. B. The average sensitivity of the four combined categories (96%) was not statistically significant ($p = 0.33$). Similarly, the difference in specificity of the four sets of diagnoses given by Dr. A and Dr. B was not found to be significantly different from the specificity averaged over these four sets ($p = 0.20$). So neither the pathologist (Dr. A or Dr. B) nor the method (standard or digital FSSM) has a significant effect on the sensitivity or specificity of the exam. The sensitivity and specificity of standard and digital FSSM averaged over all raters, including Dr. C, are shown in Table 5.5, and are sufficient for diagnostic use.

Table 5.5. Average sensitivity and specificity of standard and digital FSSM, and the difference between digital and standard FSSM sensitivity and specificity.

	Standard FSSM	Digital FSSM	Difference
Sensitivity	92.5%	100%	+7.5%
Specificity	97.5%	95.0%	-2.5%

Fleiss's kappa statistic for digital FSSM by the two pathologists, standard FSSM by two pathologists and the reference diagnostic (standard FSSM confirmed by a modified Kinyoun stain, SSM) was calculated as 0.88. An alternative calculation of Fleiss's kappa can be made by grouping the diagnoses of smears drawn from the same sputum sample as additional independent ratings of the same subject.

Although the number of ratings per subject is not uniform, the proportion of agreement can still be calculated [45]. In this case, the kappa statistic is 0.86.

5.4. Discussion

The main focus of this project was validating the experimental lens design for the array microscope and demonstrating that the lens design can be reduced to practice in a prototype that meets the needs for digital TB detection. Counting bacteria in matched fields of view shows that more bacteria are counted with digital FSSM than standard FSSM. There is high concordance (κ=0.88) between standard FSSM, digital FSSM, and the clinical lab results from TMH.

Although none of the ss+ samples were positive for Mtb by culture, AFB microscopy does not distinguish between different species of mycobacteria. This set of experiments tested the sensitivity and specificity of standard and digital FSSM with respect to AFB detection as opposed to Mtb detection. The sensitivity and specificity of the diagnostic to Mtb detection in particular depends on the prevalence of Mtb in the local population.

The preliminary estimates of sensitivity and specificity for digital FSSM using the prototype microscope for AFB detection are 100% and 95%, respectively. If the same tolerances met when fabricating an individual prototype miniature objective can be held for an entire array, then similar image quality, sensitivity and specificity is likely. Lens array fabrication is an active area of research, but certain tolerances, namely radius error, form error, and surface finish have been shown to be

repeatable for arrays of lenses, and the speed of prototyping plastic lenses has been increasing [46].

Further experiments will need to address the low throughput of digital FSSM seen in these experiments, seek better estimates of the sensitivity and specificity of digital FSSM, and reduce the size, weight, and cost of the evaluation setup as a step towards achieving the goal of a low-cost portable device for point of care Mtb detection. The low throughput was a result of using only a single miniature objective rather than an array and the lack of motorized stages for lateral translation and auto-focusing in the test platform. Automating the stages or completing the array microscope and building an array-compatible test setup would increase evaluation throughput, although automated stages are not a long term goal for the array microscope. Increasing throughput would help improve estimates of the sensitivity and specificity of digital FSSM by allowing more samples to be processed in the same amount of time. More samples would improve the precision of these estimates. Accuracy of estimates of sensitivity and specificity can be improved by increasing the number of smears examined in each set. It is possible that the low number of samples per set and the non-randomized ratio of positive and negative samples increased the chance that a diagnosis would be influenced by prior knowledge of previous diagnoses within a set. For the purpose of accurately evaluating the sensitivity and specificity of digital FSSM on its own, specimens can be digitally imaged as they become available and presented to the pathologists for diagnosis in one complete set. The concurrence of digital and standard FSSM has already been found to be very high, so there is no further need to examine smears by standard

FSSM in parallel. Finally, the cost, size, and weight of the evaluation setup can all be reduced by using off the shelf opto-mechanics in place of the modified clinical microscope. An example of such a system is shown in Figure 5.12. This system is still not a portable point of care system, but it is made up of more lightweight and low-cost opto-mechanics and off the shelf collector and condenser lenses for from Thorlabs® and filters from Chroma®. The use of these components instead of the test platform based on a Primo Star microscope has not diminished the imaging performance of the miniature objective, as shown in Figure 5.12.

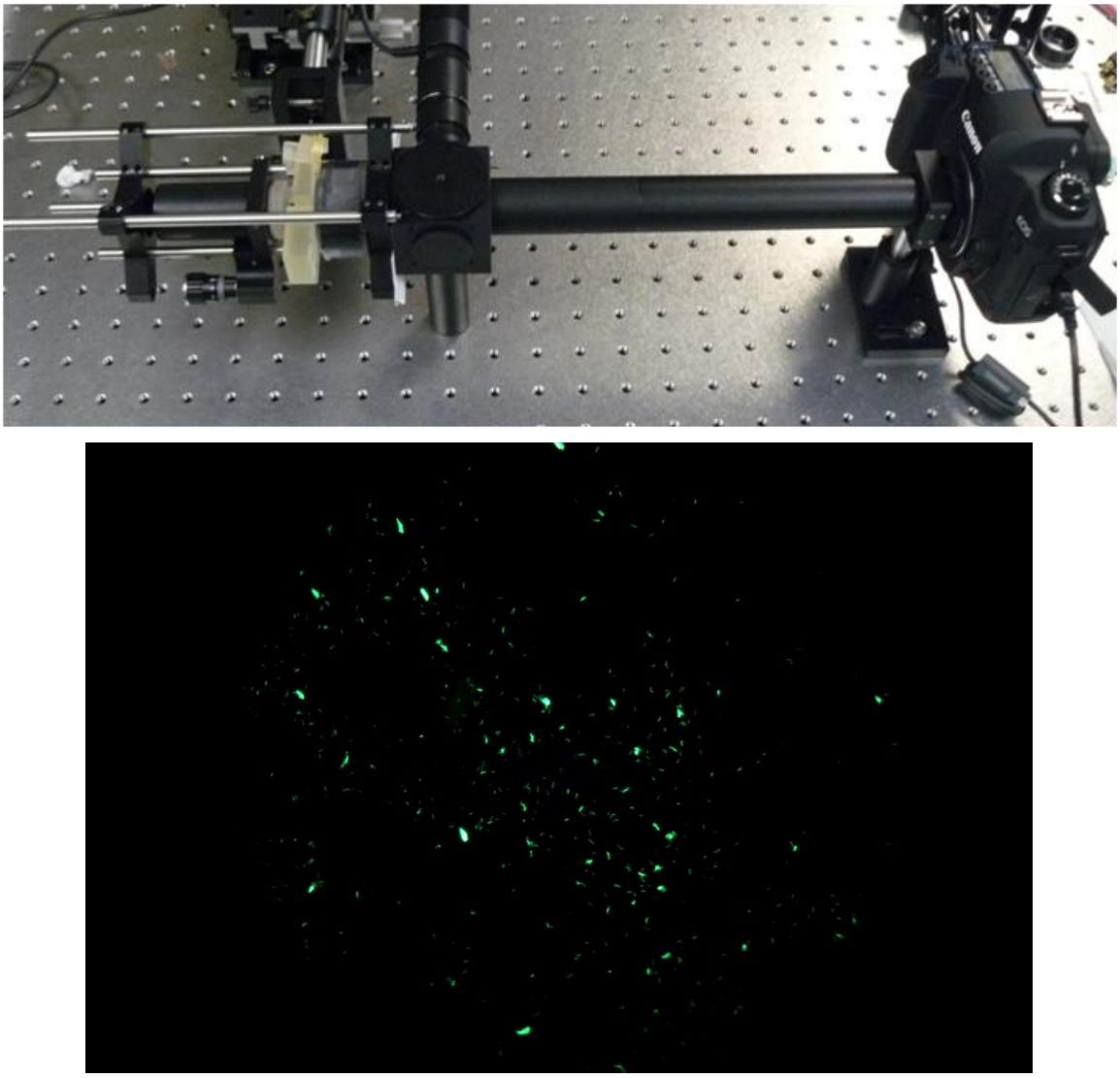

Figure 5.12. (Top) Prototype miniature objective integrated with an LED source and DSLR camera using Thorlabs optical components and Semrock filters. The stages (Bottom) Image of a BD AFB test slide stained with Auramine O. taken at 63x magnification using the above system. Exposure time was 2 s at ISO 400 sensitivity. Background is subtracted, but the contrast is not enhanced.

The increase in the number of bacteria counted with digital FSSM compared to standard FSSM is an interesting result, particularly because the root cause is unknown and it does not seem to lead to a significant difference in diagnostic

results. There were, however, six smears for which one of the pathologists changed their diagnosis between standard and digital examinations. One smear was changed from standard ss+ to digital ss-, and the other five were changed from standard ss- to digital ss+. Out of those diagnoses that were changed, more diagnoses were changed from ss- to ss+ than vice versa, although this finding is not quite significant (p = 0.102). Of the five that were changed to digital ss+, three were positive according to the reference diagnosis, and two were negative. In each of these cases, there were four or fewer bacteria counted by the pathologist who gave different standard and digital diagnoses. Figure 5.13 shows four images from four of the slides for which a pathologist gave diagnoses of standard ss- and digital ss+. Each of these images contributed to the digital FSSM bacteria count of this pathologist, but not to the standard FSSM count. Whether this is because the digital FSSM examination covered a different field of view is unknown. Further comparative experiments that combine the matched field of view and the effort to distinguish between positive and negative samples when few bacteria are present could shed some light on what patterns, if any, there are in the type of acid fast stained objects are counted as bacteria in digital FSSM, but not standard FSSM. Further experiments would also help to determine which factors, including magnification, contrast, and choice of microscope objective, have an effect on whether an object fitting this pattern is counted as an AFB.

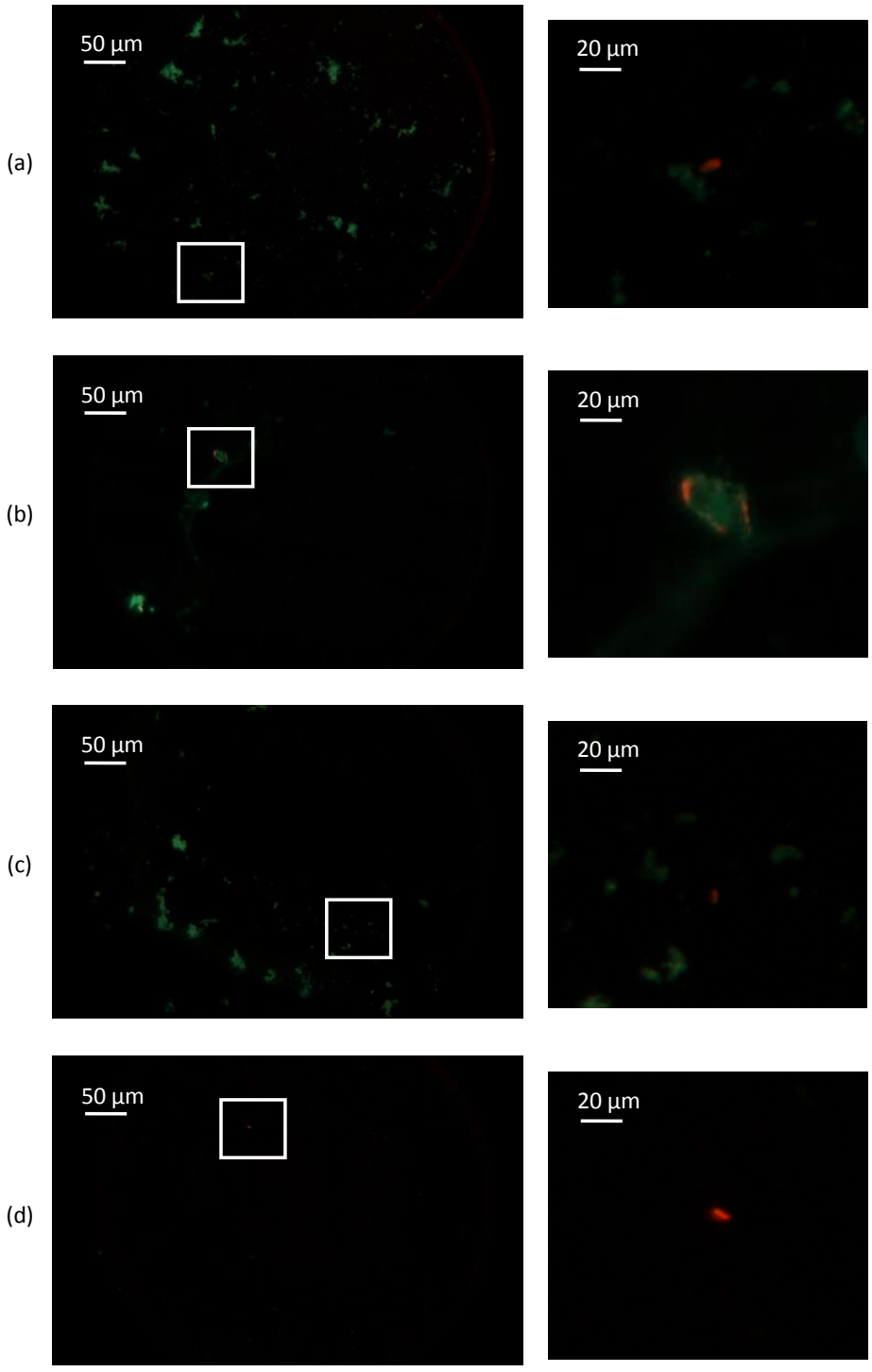

Figure 5.13. (a-b) Images from reference negative smears reported by Dr. B as standard ss- and digital ss+ (Dr. A reported standard ss- and digital ss-). (c-d) Images from reference positive smears reported by Dr. A as standard ss- and digital ss+ (Dr. B reported standard ss+ and digital ss+).

5.5. Conclusions

A prototype miniature microscope objective designed for production in an array microscope for Mtb detection has been experimentally evaluated. It can be shown to resolve sub-micron detail in a USAF resolution target. A side-by-side comparison of image quality shows that digital images acquired with the prototype miniature objective are nearly indistinguishable from digital images taken with the Zeiss Primo Star 40x objective, a commercial objective designed for FSSM. Background light levels are higher with the prototype objective, but these background light levels can be reduced with improvements in lens assembly and integration. For now, background light can be digitally subtracted and the colors digitally enhanced to provide high quality diagnostic images for digital FSSM. Digital FSSM using this miniature objective has shown an increase in organism counts compared to standard FSSM over the same field of view for patient samples smeared on an indexed grid and stained with Acridine O. Diagnostic comparisons of standard and digital FSSM by pathologists with a reference diagnostic show high concordance (κ=0.88). The preliminary estimates of sensitivity and specificity of digital FSSM determined by these experiments, 100% and 95%, are sufficient for diagnostic use. Sensitivity easily exceeds the 70% benchmark set by SSM in the DOTS program. Future work includes building the objective as an array microscope, integrating it into a lightweight, robust, and portable instrument that can be used at the point of care, and conducting larger scale studies of its effectiveness in clinical and field tests.

Chapter 6

Lens array fabrication

Two lens array fabrication techniques were explored during the course of this project. The first was 3-axis micro-milling, a technique previously shown capable of producing high quality lens mold inserts. This technique was tested for the fabrication of plastic lens arrays, which had not previously been micro-milled, eliminating the need for plastic injection molding, which adds cost and lag time to the prototyping process. The results of this experiment were published in the *Journal of Optical Engineering* in October 2010 [47]. This was the first study to show that polystyrene, Rexolite 1422 by C-Lec Plastics, Inc., could be cut with a smooth clear finish by diamond machining. These experiments determined that it is possible to machine a high quality lens surface in plastic by micro-milling and do so in an array format. The full surface of the lenses fabricated for this experiment could not be measured, however, and it was found that the machining parameters could not produce the necessary surface finish over the surface of the entire lens.

Due to the changes necessary to address this non-uniform surface roughness, the fabrication of micro-milled lens arrays required several days, which is unacceptably long. The length of time needed to fabricate a single array microscope prototype with 5 lens arrays stretches out over one month. The need to test and improve techniques for aligning bi-convex and meniscus lenses, as opposed to plano-convex or plano-concave lenses, a fabrication process measured in months is a serious drawback. For this reason, a second lens array fabrication technique was developed. This fabrication technique is the first of its kind and it was shown to provide significantly better surface finish than micro-milling in a fraction of the time. This new process is called 4-axis single point diamond machining (4-axis SPDM). The process and the results demonstrating the improvement in cutting time and surface finish were published in *Optics Express* in February of 2013 [46]. New techniques were also developed in this study for eliminating form errors and defects that result from a misaligned tool.

6.1. Micro-milling

The results of this experiment were published in the *Journal of Optical Engineering* in October 2010 [47].

Two plastic lens array were fabricated, one concave and one convex, with a 2 mm radius, 2.6 mm clear aperture, and an edge slope of 40°. At the time, the edge slope was outside the range that could be achieved by STS or FTS, although recent advances have brought the edge slope limit of STS and FTS up to 40° [48]. Both were

arrays of 20 lenses (4 × 5) fabricated in polystyrene (Rexolite 1422). The results of this study indicate that lenses can be produced by micro-milling with very accurate form error and roughness just low enough to be considered optical quality. Less than 1% per surface scattering requires approximately 15 nm roughness or less.

6.1.1. Equipment and setup

The machine used is a four-axis (X, Y, Z, and C) Nanotech 250 Ultra-Precision Lathe (UPL) (Moore Nanotechnology Systems, Swanzey, New Hampshire). The C axis control is not used, so there are three automated axes. The equipment used is shown in Figure 6.1. The milling tools are ball nose endmills with radii of ~0.5 mm made by Contour Tool (Elyria, Ohio). The 250 UPL also comes with the Moore Nanotechnology diamond turning software suite, including NanoCAM™ 1.0, NanoCAM 2D, Work Spindle Trim Balancer, and Workpiece Error Correction (WEC) software (Swanzey, NH). A spindle adapter is fixed onto the face of the work spindle, and a Swiss Rego-Fix (Indianapolis, IN) ultra-precision collet and collet nut hold the endmill in place. The Nanotech 250 comes with an internal spindle balancer that is capable of accurately balancing the spindle at speeds up to 7000 RPM. The endmill must be aligned with the spindle axis as best as possible, as described by Holme et al [39]. Misalignment can lead to form errors across the entire part, and a microscopic nub-like feature at the lens center. The tool is assumed to be centered with respect to the tool shank, and the position of the spindle adapter is adjusted while loosened until the runout of the tool shank is less than 1.5 μm. The electronic gage head shown in Figure 6.1 (Mahr Federal Incorporated, Providence, Rhode Island, model

EHE-2056) was used to measure the runout of the tool shank. Due to the tightness of fit between the spindle adapter and work spindle, no further adjustments could be made to the tool position once the spindle adapter was secured. A linear variable differential transformer (LVDT), used to measure 2-D lens profiles, is calibrated before the spindle adapter is mounted. The LVDT was calibrated by measuring a one inch calibration sphere and storing the measured error. This reference file measurement was then used to adjust later measurements of micro-milled lenses. A compound goniometer was used to minimize the tilt of the surface with respect to the spindle axis.

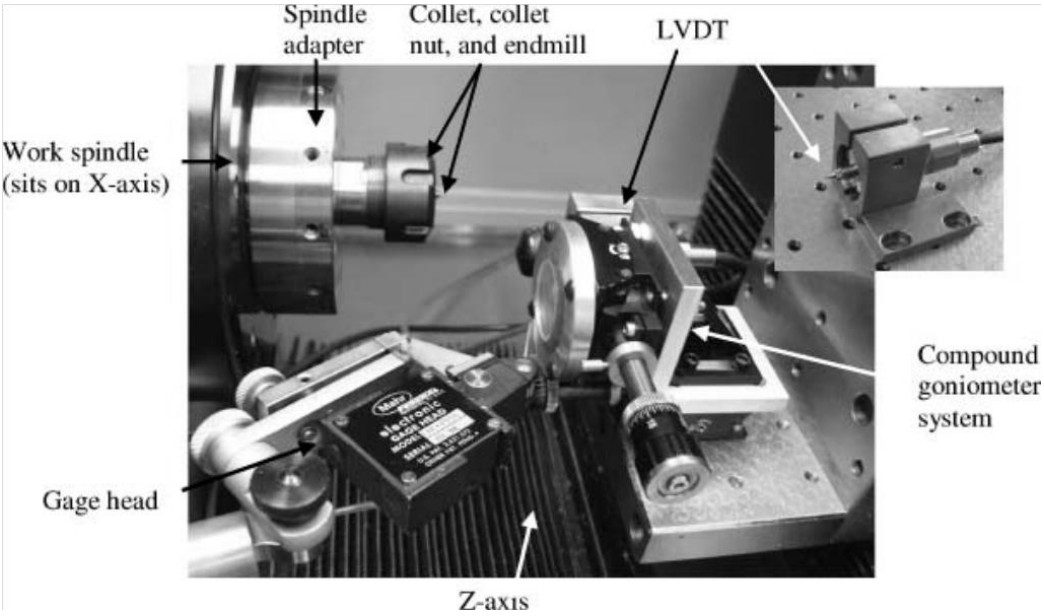

Figure 6.1. Nanotech 250 UPL setup for micro-milling. Inset: LVDT unmounted.

6.1.2. Cutting programs

A lens is micro-milled using a spiral cutting program [39], as shown in Figure 6.2. During this study, the angular feed rate was held nearly constant, so the linear

feed rate varied from the edge of the lens to the center of the lens. The micro-milling parameters used in this study are shown in Table 6.1. For both lens types, a separate rough cut program with larger radial feed rates (0.2 mm/rev) was created to remove the bulk of the material. The part programs were generated using NanoCAM 1.0. This software compensates for the shape of the spinning tool with the assumption that the solid rotation of the endmill is spherical. Waviness or misalignment of the tool makes this shape non-spherical and results in form errors, which must be corrected. Since the lenses being made in this study are rotationally symmetric, the same techniques used to correct tool path errors in single point diamond turning can be used to correct a 3-D micro-milling tool path. The Nanotech WEC software is capable of obtaining a 2-D error profile from a 2-D contact profile measurement of the part and a reference measurement of a calibration sphere. NanoCAM 2-D can be used to generate a corrected 2-D sag table, which can be converted into a corrected 3-D sag table and corresponding tool path by NanoCAM 1.0. The result of a single tool path correction applied to a micro-milled lens is shown in Figure 6.3.

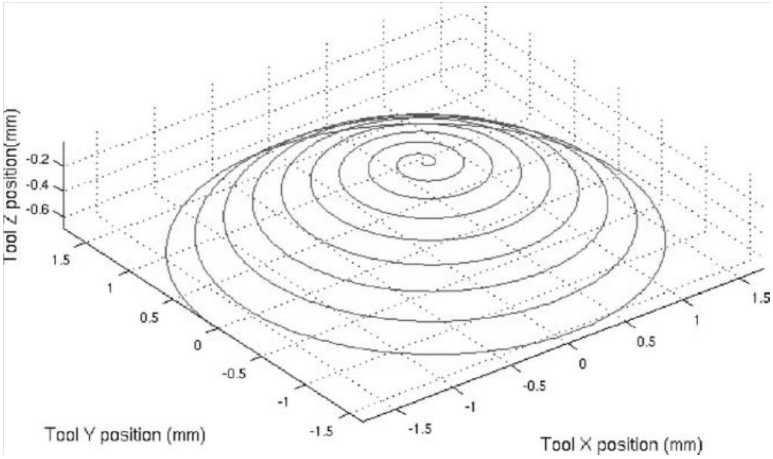

Figure 6.2. Example tool path generated by NanoCAM 1.0 for a rough-cut micro-milled convex lens having a 0.2-mm/rev radial feed rate.

Table 6.1. Single lens micro-milling parameters.

	Convex	Concave
Part radius (mm)	2.0	–2.0
Clear aperture diameter (mm)	2.6	2.6
Point density (pts/deg)	1	1
Spindle speed (RPM)	3400	3400
Radial feed rate (µm/rev)	2.5	5.0
Angular feed rate (deg/s)	125	125
Linear feed rate at part edge (mm/min)	215	126
Linear feed rate at part center (mm/min)	0.105	0.143
Depth of final cut (µm)	15	15

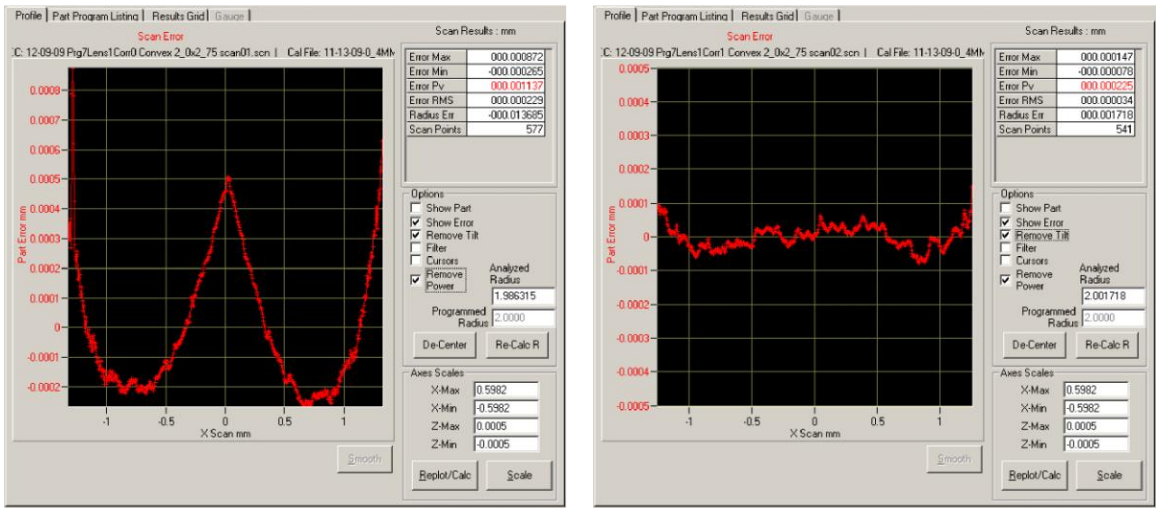

(a) (b)

Figure 6.3. Nanotech WEC measurement of lenses cut with (a) an uncorrected program and (b) a program with one correction iteration.

6.1.3. Results

The two lens arrays fabricated in this study are shown in Figure 6.4. Measurements were taken of each lens radius, surface irregularity, and roughness. Radius and surface irregularity were measured using a Zygo (Middlefield, Connecticut) PTI250 Fizeau interferometer with an f/1.5, 25-mm-diam, 655-nm wavelength transmission sphere. The radius measured is the distance between the cat's eye and confocal positions. Spatial modulations with wavelengths shorter than 15 μm were removed. Surface profiles of the lenses were measured using a Zygo New View 5032 Optical Profiler. These measurements were taken over a 0.27 $\times$ 0.35 mm field of view at a lateral resolution of 0.56 μm. Roughness estimates were calculated using these surface profiles. Modulations in the surface profile of wavelengths longer than 26.7 μm are attributed to form error and removed. The

type of filter used is a Gauss spline filter. An interferogram from the PTI250 and a surface profile measurement from the New View are shown in Figure 6.5. The tolerances typically achieved for single plastic injection molded lenses are compared to the errors measured in this study in Table 6.2.

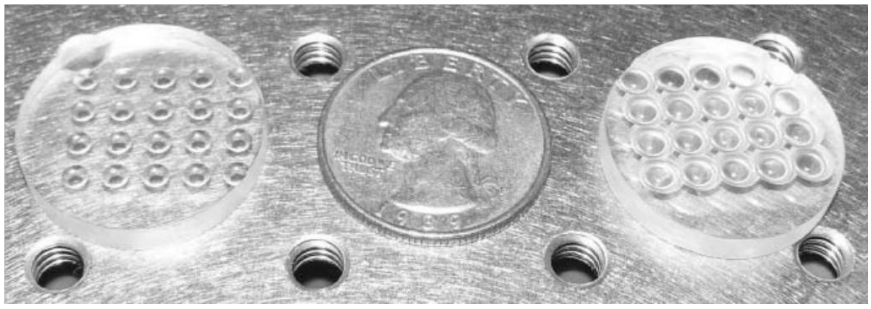

Figure 6.4. A 4×5 array of concave lenses (left) and a 4×5 array of convex lenses (right).

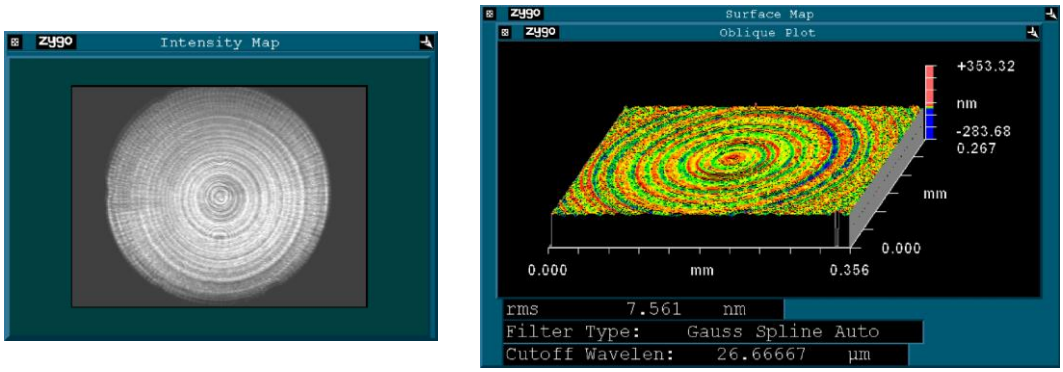

(a) (b)

Figure 6.5. (a) Fizeau interferogram of convex lens and (b) surface profile of same lens obtained from a white light optical profiler.

Table 6.2. Fabrication errors of optical parameters (±standard deviation) of convex and concave arrays micro-milled in this study.

	Convex	Concave	Versus injection molding[a]
Radius error (%)	0.102 ± 0.054	0.180 ± 0.034	State of the art (0.3)
PV irregularity (nm)	175 ± 33	179 ± 43	Tight (150)
RMS irregularity (nm)	31.4 ± 7	23.6 ± 5	Tight (30)
R_q (nm)	12.825 ± 2.45	15.813 ± 4.19	Low cost (10)

a - State of the art tolerance of single plastic injection molded lenses (not arrays of lenses) is 0.3%, tight tolerance of PV irregularity of plastic injection molded lenses is 150 nm, etc. [49]. R_q refers to the rms surface profile after filtering.

The quality surface finish of the lenses in the arrays made in this study was on average higher than what can be obtained using low-cost plastic injection molding processes. Still, with $R_q \approx$ 12-15 nm, these lenses are of optical quality. The surface irregularity of these lenses are all very good, although in this category the highest quality lenses made by plastic injection molded lenses can still outperform these lenses. Few if any plastic injection molding processes can provide a tighter tolerance on radius error. Most notable is that every lens measured has less than 0.3% radius error (Figure 6.6), which is classified as the tightest of tolerances for plastic injection molded lenses [49]. One of the concave lenses was scratched at the apex, so its cat's eye position could not be found, and therefore its radius could not be measured.

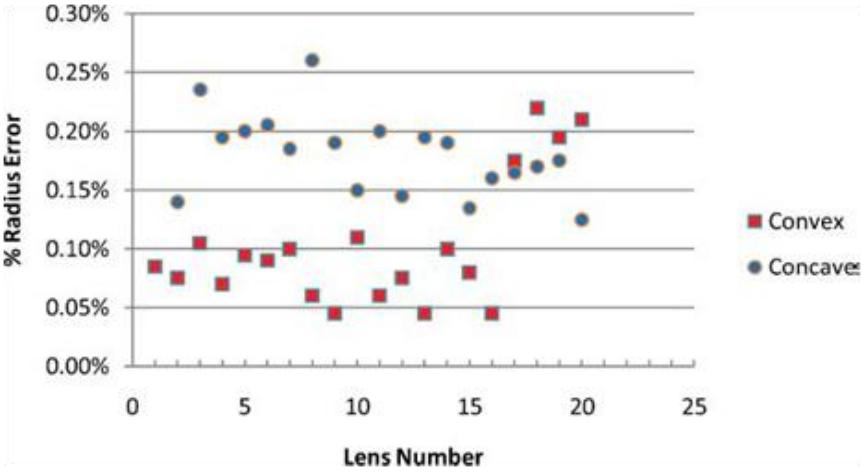

Figure 6.6. Radius error of micro-milled lenses.

6.2. Array microscope alignment and fabrication

In order to fabricate array microscopes, the arrays of bi-concave or meniscus lenses must be precisely aligned during cutting so that the two curved surfaces lie on the same optical axis. By milling complementary alignment features into the faces of two parts that need to be aligned together, the spacing, tilt, and orientation of the lens arrays can be precisely controlled (Figure 6.7). These same alignment features can also keep the two sides of a single lens array in the correct position during alignment. This process is illustrated in Figure 6.8 and explained in the following eight step process:

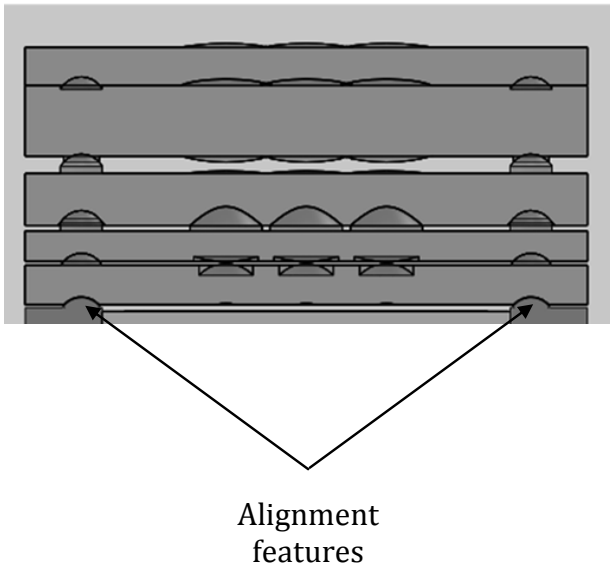

Figure 6.7. Alignment features controlling the tilt, spacing, and orientation of lens arrays in an array microscope.

1. A workpiece is pre-machined with low flat posts at the locations where positive alignment features will be cut.
2. An alignment fixture is pre-machined with low flat posts at the positions where positive alignment features will be cut.
3. The alignment fixture in practice is bolted to the milling machine's Y-axis facing the spindle. The workpiece is aligned to the alignment fixture within 1 mm.
4. Lenses and negative alignment features are cut into the workpiece.
5. The lens array is removed,
6. Positive alignment features are cut into the alignment fixture.
7. The lens array is placed back on the alignment fixture with the lenses and negative features facing the fixture. The mated positive and negative features provide micrometer level alignment.
8. Lenses are cut on the back face of the lens array at the same positions as the lenses on the front face. Positive alignment features are cut at the same locations as the negative alignment features.

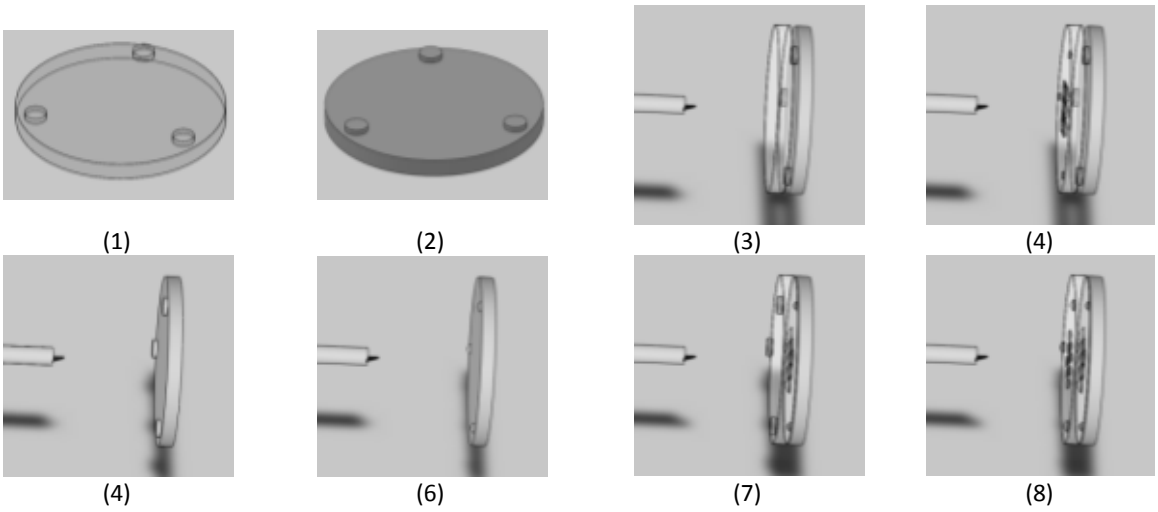

Figure 6.8. Procedure for milling alignment features in a bi-concave lens array and alignment fixture.

What is not shown in Figure 6.8 is the collar that fits over the lens array with through holes for screws that sandwich the lens array between the collar and the alignment fixture. The collar effectively distributes force around the edge of the lens array, reducing the risk of bending or pulling the workpiece out of alignment.

This alignment system was tested by milling two flat surfaces with the complementary alignment features. One flat was placed under the New View optical profiler, and the stage tilt was adjusted until the measured tilt of the flat was 0. The second flat was placed on top of the first flat, aligned with the alignment features described above, and the tilt of the top surface was measured. This process was repeated 9 times. The tilt was found to be 24 arc seconds (0.0067°) with a standard deviation of 16 arc seconds (0.0046°). The maximum tilt found was 46.1 arc seconds (0.013°), which corresponds to a difference in height between the edge and center of the lens array of 4 μm.

The initial test of the alignment fixture system validated the alignment system designed for array microscope fabrication, but fabrication of an array microscope with this system was not successful. The attempted lens array is shown in Figure 6.9. The central element can easily resolve the 2 μm size features of Group 7 Element 6 of a USAF resolution target, but the contrast is very low. The air force objective was illuminated in transmission at 455 nm, so the resolution limit should be 0.69 μm, but 2 μm is the smallest feature size on a typical USAF target. The surface roughness of most of these lenses did not meet the standards set in the previous experiment, and some lenses appeared slightly cloudy upon close inspection. These surface attributes could easily lead to low image contrast, as seen in Figure 6.9.

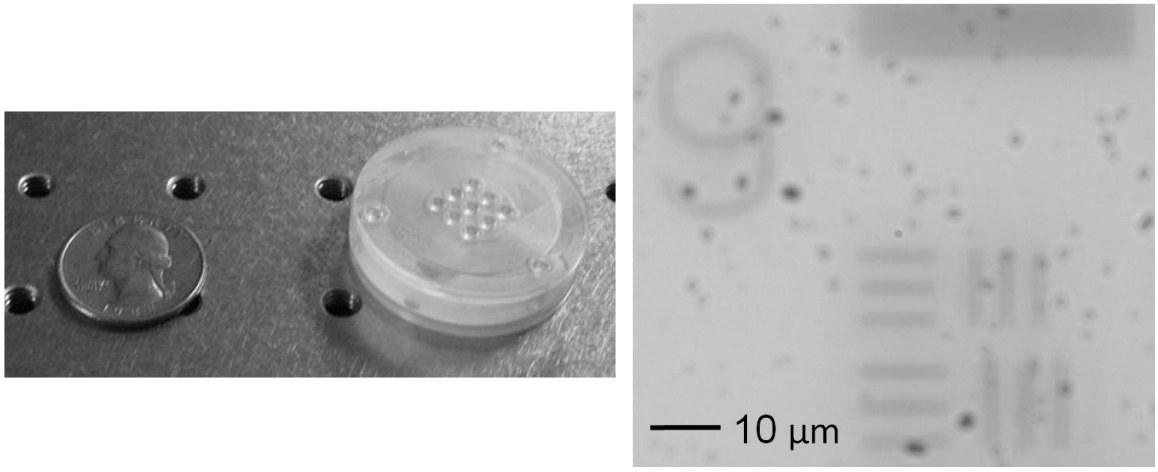

Figure 6.9. (Left) Initial attempt to fabricate an array microscope. (Right) First image taken with first array microscope built at Rice University. USAF resolution target, Group 7 Elements 5 & 6, imaged in transmission using a ThorLabs 455 nm 700 mW LED.

Specific changes between the process used in the first micro-milling experiment and the attempt to fabricate an array of microscopes are listed below.

Any one or combination of these factors may have led to the reduction in surface quality:

- A new alignment fixture was used

  Different alignment fixtures will have different stiffness and resonant frequencies. Vibrations in the fixture during machining lead directly to surface roughness.

- The tool's alignment changed

  There will always be a difference in the alignment of a tool from one setup to the next on the order of a few microns. Certain tool misalignment cause the tool to scrape the surface of the lens when it is rotated 180° from the intended point of contact.

- A collar was used to hold the lens array in place

  This collar obstructs air flow which clears chips. Chips can collect, melt, and coalesce into a clump of plastic on the tool. Clumps of plastic can cause wear on the surface of the lens and the tool.

- The shapes of lenses milled were different

  These lenses included lenses with a shallow curvature. The tool cuts shallow curvature surfaces with a point that is closer to the tip and moves at lower velocity

- The surface quality of the first micro-milled lenses is only partially known; the milling parameters may have been sub-optimal

  These lenses were 2 mm in diameter with slopes up to 40°. The New View optical profiler has difficulty measuring slopes steeper than 8°, so only the central portion of these lenses could be measured.

Misalignment of the tool and sub-optimal machining parameters are the easiest to detect and correct, and these errors were fixed after the first attempt to fabricate a lens array. The alignment system was also modified to remove the collar and allow better chip clearance by applying the screws directly to the lens array (Figure 6.10). The new alignment system fared much worse than the first in terms of positional

tolerances, and some surface defects remained, although roughness was reduced somewhat. Another improvement to the micro-milling process was found by other researchers who mounted the milling tool at an oblique angle [50], rather than parallel to the Z-axis (Figure 6.1). This adjustment cannot be done on the Nanotech 250 UPL, however.

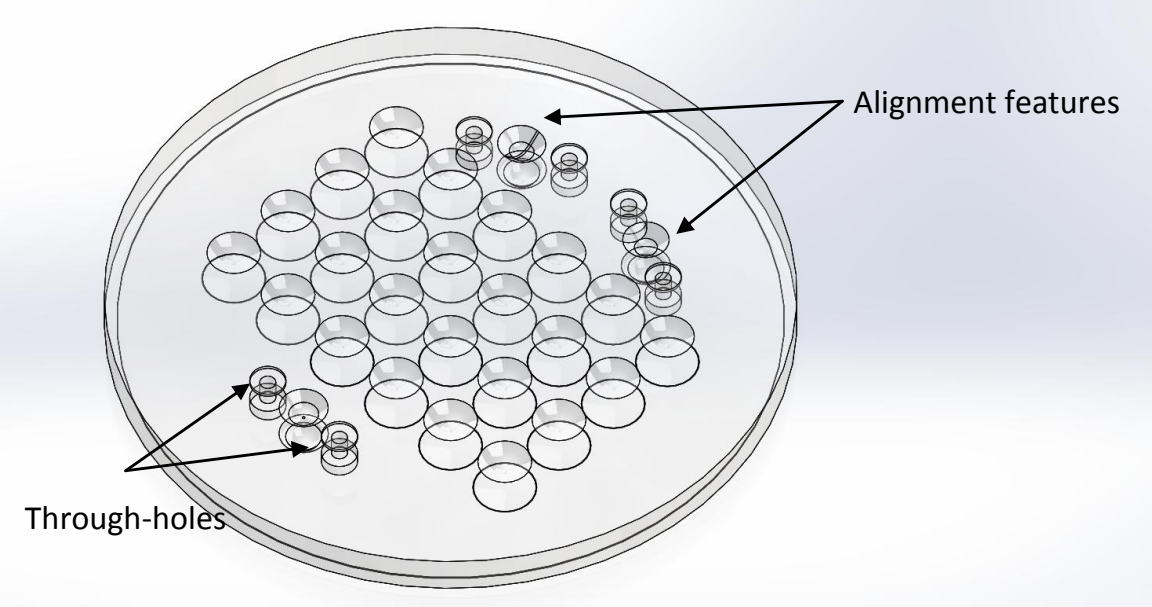

Figure 6.10. Alternative approach to securing lens array to alignment fixture during lens fabrication: put through holes into the array before micro-milling and bolt the lens array directly to the alignment fixture without a collar.

It became clear that micro-milling is a long way from being a fabrication technique that is capable of producing array microscopes, and worse, the adjustments made to optimize the machining parameters and reduce roughness led to hour long cutting times just for the finish cut of a single lens. For a lens array design with 240 lenses, this is far too long to be a rapid prototyping process. In order to develop an array microscope, a diamond machining technique was needed.

6.3. 4-axis single point diamond machining

The process and the results demonstrating the improvement in cutting time and surface finish were published in *Optics Express* in February of 2013 [46]. This process was found to produce lens arrays more than 10x faster using our own lens fabrication equipment. State of the art micro-milling machines use high speed spindles, which allow faster micro-milling, but this technique was found to outperform even these machines. A provisional patent for this technology was filed on December 12, 2012 [51].

A novel method for fabricating lens arrays and other non-rotationally symmetric free-form optics is presented. This is a diamond machining technique using 4 controlled axes of motion – X, Y, Z, and C. As in 3-axis diamond micro-milling, a diamond ball endmill is mounted to the work spindle of a 4-axis ultra-precision computer numerical control (CNC) machine. Unlike 3-axis micro-milling, the C-axis is used to hold the cutting edge of the tool in contact with the lens surface for the entire cut. This allows the feed rates to be doubled compared to the current state of the art of micro-milling while producing an optically smooth surface with very low surface form error and exceptionally low radius error.

6.3.1. Overview

Several microlens array fabrication techniques have been well established and are in widespread use. All of these techniques are capable of producing lenses with state of the art form and surface finish, but each of these techniques has a

limitation that makes it unsuitable or undesirable to meet the demands of emerging miniature lens array imaging systems (Table 6.3). Single point diamond turning, a very fast 2-axis lathe technique, is capable of producing high quality individual lenses in a wide range of focal lengths and diameters. Lens array fabrication with SPDT takes much longer and cannot be automated because the work piece must be manually repositioned for each lens in the array. Other similar diamond turning techniques such as STS and FTS synchronize the motion of the X and Z axes of SPDT with the work spindle using a spindle encoder, also called a C-axis. This extra degree of freedom enables 3-D fabrication of non-rotationally symmetric objects like lens arrays. Although fast and fully automated, the edge slopes of lenses fabricated by STS and FTS are limited by the diamond tool's relief angle [38,52–54]. STS/FTS tools with a 40° relief angle have recently become available [48], but it is impossible to achieve a 90° relief angle. Non-machining techniques can provide both automation and steep slopes, but come with other difficulties. Grayscale lithography can produce high quality lenses of arbitrary shapes and with nearly vertical edge slopes, but sags greater than 60 μm are considered extreme for this technique [37,55]. Droplets of optically clear material form low f/# spherical lenses naturally due to surface tension. They can be melted and cooled as in thermal reflow or printed using inkjet technology and cured with ultra-violet (UV) irradiation [35,36]. Larger lenses can take on aspheric shapes due to the effects of gravity [56,57]. Application of an electrostatic field gives greater control over the shape of the lens [58]. The overall size of the lens is limited, however, and arbitrary shapes are not currently possible. Other non-cutting techniques such as laser direct writing and deep lithography with

protons have been developed, but do not produce lenses with the same quality as thermal reflow and microjet printing [59]. Three-axis micro-milling is another diamond machining technique which overcomes the limitations on lens geometries found in other lens array fabrication techniques. This process can produce a wide range of lens shapes including steep, low f/# lenses, aspheres, asymmetric lenses, and other freeform optics [38,39,47,50,60]. The drawback of 3-axis micro-milling is that it requires long fabrication times compared to most other lens fabrication techniques. With a feed rate of 100 mm/min and radial feed rate (stepover) of 4 μm per revolution (0.4 mm^2/min), a 5 mm clear aperture diameter lens requires approximately one hour of machining time. This is the fastest fabrication rate published for 3-axis micro-milling of optically smooth surfaces so far [38,60]. A 3x3 array of 5 mm lenses fabricated on a 19.1 mm diameter disk would require a 9 hour finish cut with micro-milling, compared to 3.2 hours with STS, or 1.3 hours with FTS.

Table 6.3. Limitations of fabrication processes.

Fabrication technique	Automatic	Arbitrary Aspheres	Sag (mm)	D (mm)	Edge Slope (°)	Fabrication Rate[b]	Ref
SPDT	No*	Yes	No limit	No limit	0-90	5-25 mm/min	[61]
STS	Yes	Yes	No limit	No limit	0-40*	0.1 mm/min	[48,53]
FTS	Yes	Yes	0-6	No limit	0-40*	0.25 mm/min	[48,54]
Thermal reflow	Yes	No*	0-2[a]	0.005-2*	0-90	Parallel, 0.5 min	[56,57,59]
Microjet Printing	Yes	No*	0-5[a]	0.02-5	0-180	0.5-5 mm^3/min	[36,58,59]
Grayscale Lithography	Yes	Yes	0-0.06*	> 0.0006	0-90	Parallel, 1.33 min	[37]
3-axis micro-milling	Yes	Yes	No limit	No limit	0-90	0.4-1.25 mm^2/min*	[38,60,62]
4-axis SPDM	*Yes*	*Yes*	*No limit*	*No limit*	*0-90*	*0.5-2.5 mm^2/min*	

[a] – The height of a spherical reflow or printed lens does not exceed its diameter. Additional limitations may apply.
[b] – Unless otherwise specified, fabrication rate refers to unit of part semi-diameter fabricated per unit time (mm/min), unit of part area in XY plane fabricated per unit time (mm^2/min) or unit of part volume fabricated per unit time (mm^3/min). Only "finishing" steps, those that determine the final shape and surface quality of the lens, are included.
* – Indicates that all other fabrication techniques outperform this technique in the given category. These limitations may lead one to consider choosing an alternative fabrication technique.

A system such as an array of miniature microscopes such as the one proposed in [40] requires aspheric lenses with low f/#, deep sag and tight tolerances. Altogether, 240 lenses need to be machined, 192 of which have a diameter larger than 5 mm with sags and edge slopes that fabrication techniques other than 3-axis micro-milling cannot possibly fabricate in an automated process. With micro-milling, each 5 mm diameter lens would require approximately one hour for the finish cut at 0.4 mm^2/min, totaling 8 days of uninterrupted machining time for the all the lenses in the arrays [38,60]. This much fabrication time adds up to a prohibitive expense for prototyping novel, complex, arrayed imaging devices. Fabrication rates for micro-milling have been increasing as the process and equipment have improved, reaching feed rates up to 250 mm/min and fabrication rates up to 1.25 mm^2/min [62]. Despite the improvements, 3-axis micro-milling is still slower than the other automated diamond machining techniques for most lens arrays. A new technique is needed that can match the ability of 3-axis micro-milling to produce a range of lens types of excellent optical quality in an array or freeform pattern in a fraction of the time currently needed. Four-axis single point diamond machining (4-axis SPDM) is the technique that is proposed here, and it meets all the same requirements as 3-axis micro-milling while reaching feed rates of 500

mm/min, 5x faster than published feed rates for micro-milling optical surfaces [38] and double the feed rates possible today.

This paper will describe the principles and implementation of the proposed technique and show results demonstrating the reduction in cutting time while achieving equal or better tolerances (roughness, form error, and radius error) as 3-axis micro-milling. Implementation includes the process of converting a 3-axis micro-milling numerical control (NC) program into a 4-axis SPDM NC program and new methods to compensate for tool misalignment in the spiral tool path. To the best of our knowledge, this is the first time that the 4-axis SPDM technique, the methods presented here to correct the tool misalignments in the tool path, and results obtained using these methods have been published. In addition, lenses fabricated using a 3-axis (X,Y,Z) micro-milling process are presented for comparison with lenses fabricated with this new technique.

6.3.2. The 4-axis SPDM process

6.3.2.1. Principles of 4-axis SPDM

Four-axis SPDM shares similarities with both 3-axis micro-milling and conventional SPDT. The path of the tool is a spiral in (X, Y, Z) coordinates, the same as in 3-axis micro-milling. The difference is that the spindle turns much slower, making only one revolution for every loop in the spiral tool path, and it turns in the opposite direction. The 4^{th} axis is the C-axis, which is used to keep the tool angle and position tightly synchronized. The tool angle always orients the face of the tool so

that it is coplanar with the lens axis of symmetry (Figure 6.11). From the point of view of the diamond tool, the motion is exactly the same as SPDT.

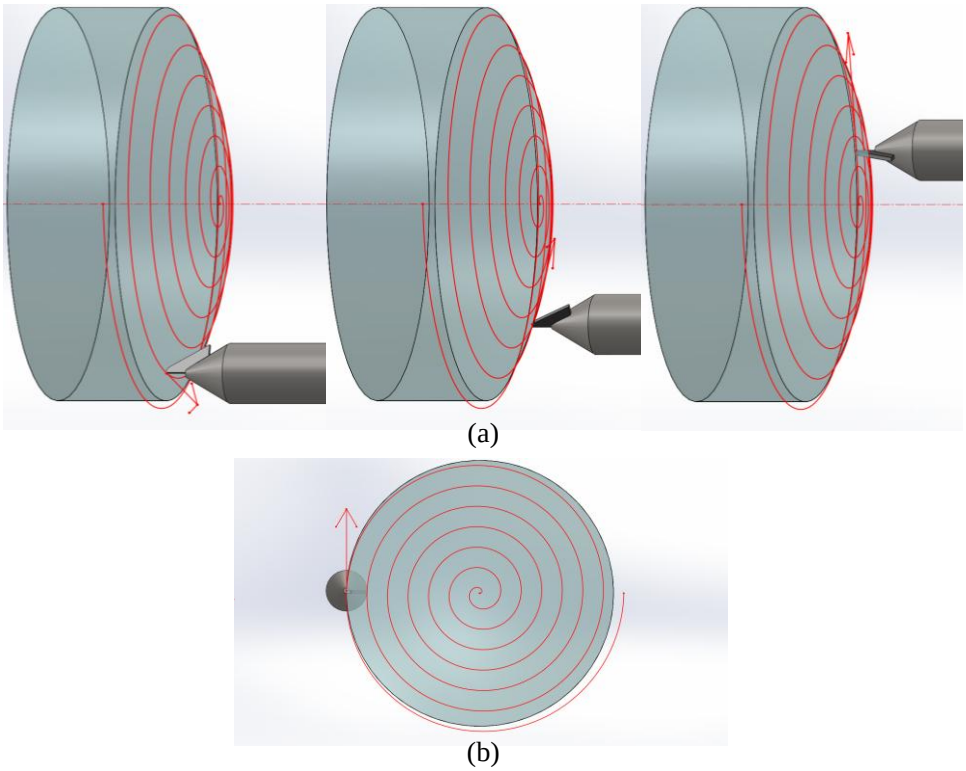

Figure 6.11. (a) View from the side of the tool changing its orientation along with its position so that the face of the tool is always coplanar with the axis of symmetry. Shown in red is the spiral path of the tool and an arrow indicating the direction of travel. The dashed red line is the axis of symmetry. (b) View along the axis of symmetry from behind the lens.

6.3.2.2. Four-axis SPDM vs. other diamond machining techniques

In diamond turning (SPDT, STS, and FTS), the surface finish is affected by a number of factors which include tool quality, stability of the spindle, work-piece fixture and stages, and the radial feed rate or feed per revolution. When the radial feed rate is too high, the tool imprint (i.e. – the grooves left by the tool) becomes the

main contributor to surface roughness. The width and depth of these grooves depends on the tool radius and the feed per revolution. In 3-axis micro-milling, the tool imprint is not a groove, but a divot (Figure 6.12). These divots are a result of a cutting process in which the tool is not in constant contact with the work piece. Instead the tool removes a small amount of material once per spindle rotation, leaving behind a divot. The width and depth of these divots depends on the tool radius and radial feed rate, just as the groove width does in diamond turning. The length of these divots depends on the chip per tooth. Chip per tooth is the distance the tool moves in the time it takes the spindle to complete one rotation and is equal to feed rate divided by spindle speed. In order to achieve a surface finish comparable to diamond turning without changing tools, the chip per tooth and feed per revolution in 3-axis micro-milling need to be low enough so that the width, length and depth of the divot are negligible. A decrease in chip per tooth can be accomplished either by decreasing the feed rate or by increasing the spindle speed. In order to increase the feed rate without the tool imprint size, the spindle speed must be increased proportionally as well. High speed spindles with top speeds of 60,000 rotations per minute (RPM) have been used to micro-mill lenses at feed rates of up to 250 mm/min at a roughness of 5 nm [62].

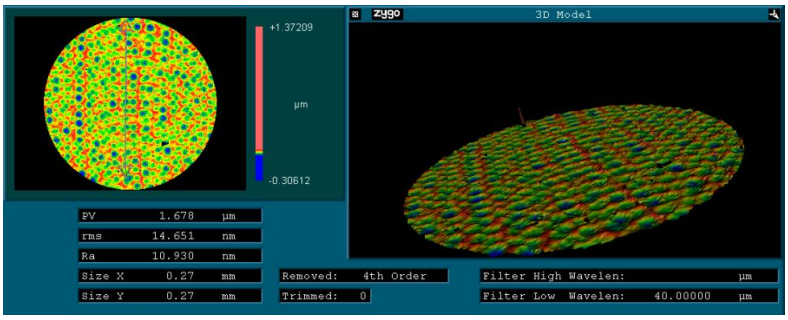

Figure 6.12. Micro-milling tool imprint on a plastic lens when chip per tooth is too large. The height and spacing of the divots depends on spindle speed, feed rate, and tool size. This surface was obtained using a 0.53 mm radius tool at a 14 µm chip per tooth.

6.3.3. Methods

6.3.3.1. Equipment

The 4-axis SPDM technique was developed on a 250 Ultra-Precision Lathe (UPL) from Moore Nanotechnology Systems, Inc. (Nanotech®). The 250 UPL lathe comes standard with X and Z axes. This 250 UPL is also equipped with the optional C and Y axes. In work spindle mode, the spindle reaches a top speed of 10,000 RPM, so it is not a high-speed spindle. Finished surfaces were cut with a 0.539 mm diamond ball endmill from Contour Fine Tooling, Inc. 3-axis micro-milling NC programs were generated by Nanotech's NanoCAM 1.0 software. These NC programs have the necessary G-code headers and a spiral tool path that allows the milling tool to cut out the shape of the lens. The conversion of 3-axis micro-milling NC programs to 4-axis SPDM NC programs was done in Matlab® (R2010b). The Nanotech Work piece Error Correction (WEC) system was used to make 2-D profile measurements of test parts. This system includes a linear variable differential transformer (LVDT) and

accompanying data acquisition and analysis software. 3-D scans of finished surfaces were taken using two Zygo® interferometers, the PTI250™ Fizeau interferometer and the NewView™ 5032 optical profiler. The Zygo interferometer measurements were analyzed in MetroPro™ 8.2.0 (Sunnyvale, CA).

6.3.3.2. Tool path conversion

Because 4-axis SPDM and 3-axis micro-milling both require a spiral tool path, the easiest way to create a 4-axis SPDM NC program is to convert it from an existing 3-axis micro-milling NC program. The most important change that needs to be made in the header section is the removal of M03 or M04 work spindle commands that activate the spindle asynchronously. The 250 UPL's controller will halt execution if an M03 or M04 is encountered in an NC program while the C-axis is engaged. Other changes may be needed to ensure that the tool safely approaches the part and starts cutting from the correct position in the correct orientation. Next, the C-axis coordinate must be added to each of the XYZ-axis coordinates. It is best to do this using an automated script or executable program which reads in and copies out the XYZ coordinates with the C-axis coordinate appended (Figure 6.13).

In order to mimic the of SPDT process, the face of the tool must be coplanar with the surface's axis of symmetry. In the spiral tool path generated by NanoCAM 1.0, XY coordinates are defined at regular angular intervals. This means that the C-axis coordinate needs to be incremented by the same angular step. As shown in Fig. 4, the tool starts a cut oriented at 180° and turns clockwise 0.5° every time it moves from one point in the tool path to the next. The direction that the tool turns depends

on the tool, but will always be in the opposite direction used for micro-milling. A tool that spins clockwise when micro-milling will turn counter-clockwise during 4-axis SPDM and vice versa.

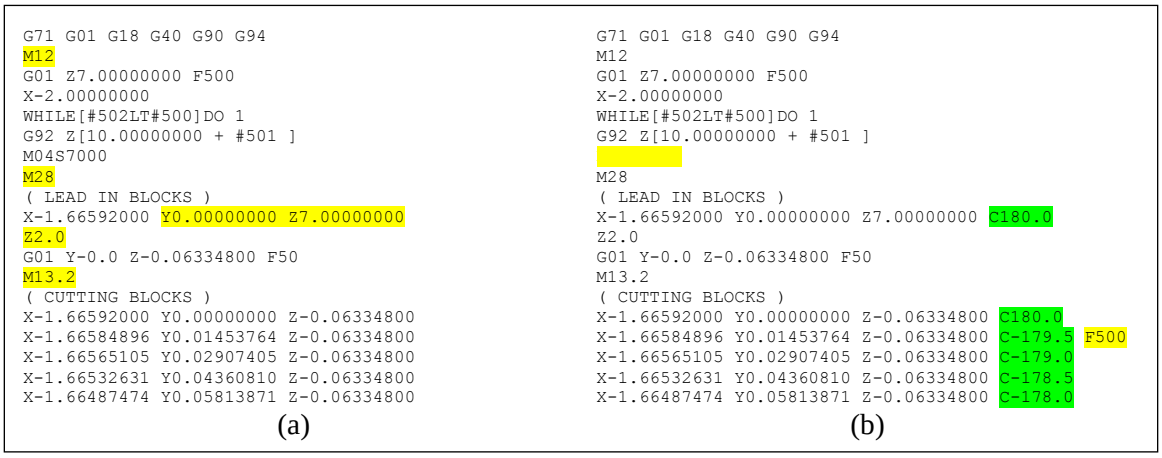

Figure 6.13. (a) Segment of a 3-axis micro-milling NC program generated by NanoCAM 1.0. Highlighted in yellow are changes that were made to the program manually after it was generated in NanoCAM. (b) 4-axis SPDM NC program segment generated from the 3-axis micro-milling NC program on the left. Green highlights indicate changes made to the code in (a) by an automated Matlab script, which added C-axis coordinates to all XYZ coordinates. Yellow highlights indicate changes made in a text editor afterwards.

6.3.3.3. Tool misalignment and tool path correction

The machine configuration for 4-axis SPDM is the same as in 3-axis micro-milling [47]. The diamond tool is mounted to the work spindle by a collet chuck. The collet chuck and tool must be carefully aligned with the spindle centerline for best results. Despite best efforts, though, there will inevitably be some misalignment between the tool and the spindle centerline which can be several microns. The types of tool misalignment errors that can occur in 3-axis micro-milling also occur in 4-

axis SPDM, and their effects on form error are the same. These alignment errors are called tool height error (t_h) and tool past center or not to center (t_c) (Figure 6.14). The names tool height error and tool past or not to center are used because these misalignments produce the same exact form errors as their well-known counterparts in SPDT. Tool orientation is an additional type of misalignment that is unique to 4-axis SPDM.

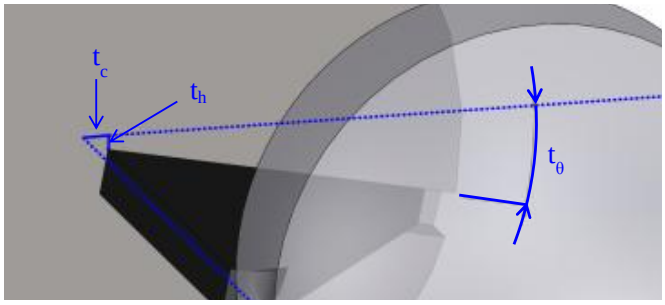

Figure 6.14. Four-axis SPDM tool misalignment errors when the C-axis coordinate is 0°. Tool height error, t_h, and tool past center error (or tool not to center error), t_c are the vertical and horizontal distances from the spindle centerline to the tool apex. Tool orientation error, t_θ, is the angle between the face of the tool and the plane containing the spindle centerline and the lens axis of symmetry.

Because t_h and t_c are already well-known in SPDT, there are a number of techniques already used to evaluate the form error of a lens or a spherical test surface and determine their values. Tool height error can be estimated by examining the nub or cone at the center of the lens using a microscope and an eyepiece reticule. MetroPro and WEC both include analysis features that estimate t_c based on a test surface measurement. Any technique for measuring t_h and t_c for SPDT surfaces is equally valid and useful in 3-axis micro-milling and 4-axis SPDM. In these experiments, the WEC measurements were used to calculate t_c, and an Edmund

Industrial Optics 3x zoom lens and a Sony® SSC-DC193 Color Video Camera were used to determine t_h. $t_h < 0$ if the tool is below the spindle centerline when the tool is at the 0° C-axis position. $t_c < 0$ if the tool is not to center.

In SPDT, t_h and t_c errors can be eliminated by adjusting the physical height of the tool and shifting the XZ coordinate system in the ±X direction. Physical adjustments to the position of a milling tool are more difficult, and a coordinate system shift will not correct either of these errors. Instead, each coordinate in the tool path must be adjusted independently. For each pair of XY coordinates generated by NanoCAM 1.0, which assumes zero misalignment, the adjusted coordinates, X*Y*, can be calculated using Equation (6-1). Figure 6.15 shows a corrected 4-axis SPDM NC program segment.

$$\begin{bmatrix} X^* \\ Y^* \end{bmatrix} = \left(\begin{bmatrix} 1 & 0 \\ 0 & 1 \end{bmatrix} + \frac{1}{\sqrt{X^2 + Y^2}} \begin{bmatrix} t_c & t_h \\ t_h & t_c \end{bmatrix} \right) \begin{bmatrix} X \\ Y \end{bmatrix} \tag{6-1}$$

```
G71 G01 G18 G40 G90 G94                          G71 G01 G18 G40 G90 G94
M12                                              M12
G01 Z7.00000000 F500                             G01 Z7.00000000 F500
X-2.00000000                                     X-2.00000000
WHILE[#502LT#500]DO 1                            WHILE[#502LT#500]DO 1
G92 Z[10.00000000 + #501 ]                       G92 Z[10.00000000 + #501 ]
M28                                              M28
( LEAD IN BLOCKS )                               ( LEAD IN BLOCKS )
X-1.66592000 Y0.00000000 Z7.00000000 C180.0      X-1.66888096 Y0.00670000 Z7.00000000 C180.0
Z2.0                                             Z2.0
G01 Y-0.0 Z-0.06334800 F50                       G01 Y-0.0 Z-0.06334800 F50
M13.2                                            M13.2
( CUTTING BLOCKS )                               ( CUTTING BLOCKS )
X-1.66592000 Y0.00000000 Z-0.06334800 C180.0     X-1.66888096 Y0.00670000 Z-0.06334800 C180.0
X-1.66584896 Y0.01453764 Z-0.06334800 C-179.5 F500   X-1.66875134 Y0.02126322 Z-0.06334800 C-179.5 F500
X-1.66565105 Y0.02907405 Z-0.06334800 C-179.0    X-1.66849463 Y0.03582471 Z-0.06334800 C-179.0
X-1.66532631 Y0.04360810 Z-0.06334800 C-178.5    X-1.66811087 Y0.05038331 Z-0.06334800 C-178.5
X-1.66487474 Y0.05813871 Z-0.06334800 C-178.0    X-1.66760007 Y0.06493796 Z-0.06334800 C-178.0
                  (a)                                              (b)
```

Figure 6.15. (a) An uncorrected 4-axis SPDM NC program segment. (b) The same 4-axis SPDM NC program with numerical correction for tool height error (t_h) and tool not to center error (t_c). t_h = -0.0067 and t_c = 0.00296096.

The tool is oriented roughly by rotating the tool so that it faces straight up and then setting the Nanotech 250 UPL's program C-axis coordinate to 0. By eye,

this can be done with a precision of about 15°. With the help of a camera t_θ can be reduced to approximately ±3°. A more precise estimate of the tool orientation error requires cutting and measuring a spherical test part.

When the tool is oriented incorrectly, it will have an elliptical cutting profile. The cutting profile of a tool in coordinates (S,T) are the radial and axial offsets, respectively, from the commanded tool position to the point of contact with the surface (Figure 6.16). For a perfectly aligned tool with zero radius error and waviness, the tool's shape, cutting profile, and programmed tool radius compensation offsets should be identical. In the case of a misaligned tool, the cutting profile differs from the tool shape and programmed tool compensation offsets. The tool cutting profile can be calculated using the WEC measurement of a test surface profile. For nominally spherical test surfaces, the tool profile can be calculated from the measured test surface profile, (X, Z), using Equations (6-2)and (6-3). For aspherical surfaces, numerical methods must be used to find the cutting profile. In these equations, $F(X) = Z$ is the commanded tool position in Z as a function of X, and $G(X) = F'(X)$. R_t is the programmed tool radius and R_s is the programmed test part radius.

The calculated cutting profile of a misaligned tool and its elliptical fit are shown in Figure 6.17. The major axis of this ellipse is the tool diameter, and the minor axis depends on the tool orientation error. Tool orientation error can be calculated from the best fit ellipse using Equation (6-4). The sign of the tool orientation error is ambiguous because a misalignment in either direction will

produce the same elliptical cutting profile. The larger the sweep of the tool used to cut the test part, the more accurate the calculation of tool orientation error will be.

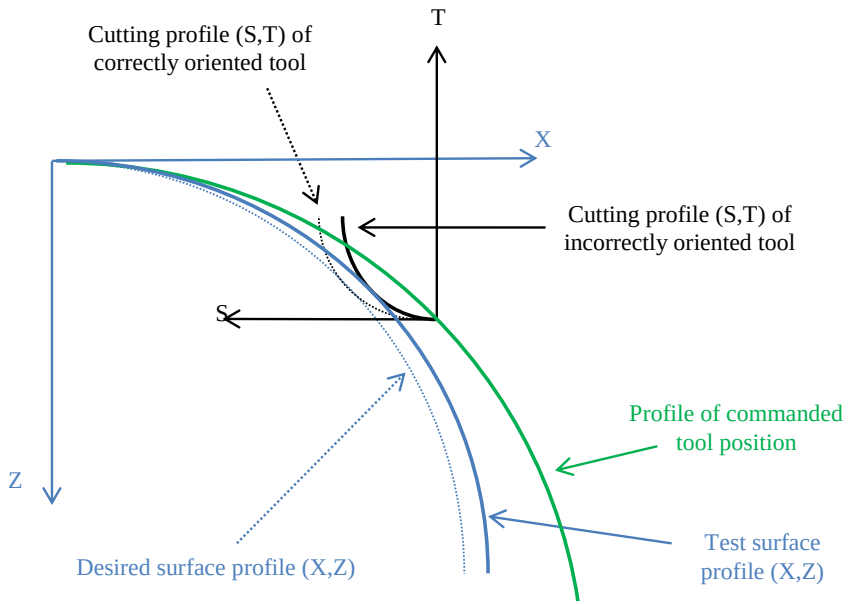

Figure 6.16. Relationship between the surface profile, the profile of the commanded tool position, and the tool profile. The points along the cutting profile can be found by moving the ST coordinate system along the profile of the commanded tool position and finding the intersection between the tool and surface profiles.

$$S = -X + G^{-1}(X) = -X - (R_t + R_s)\frac{\frac{dZ}{dX}}{\sqrt{1+\left(\frac{dZ}{dX}\right)^2}} \tag{6-2}$$

$$T = Z + F\left(G^{-1}(X)\right) = Z + (R_t + R_s)\left(1 - \frac{1}{\sqrt{1+\left(\frac{dZ}{dX}\right)^2}}\right) \tag{6-3}$$

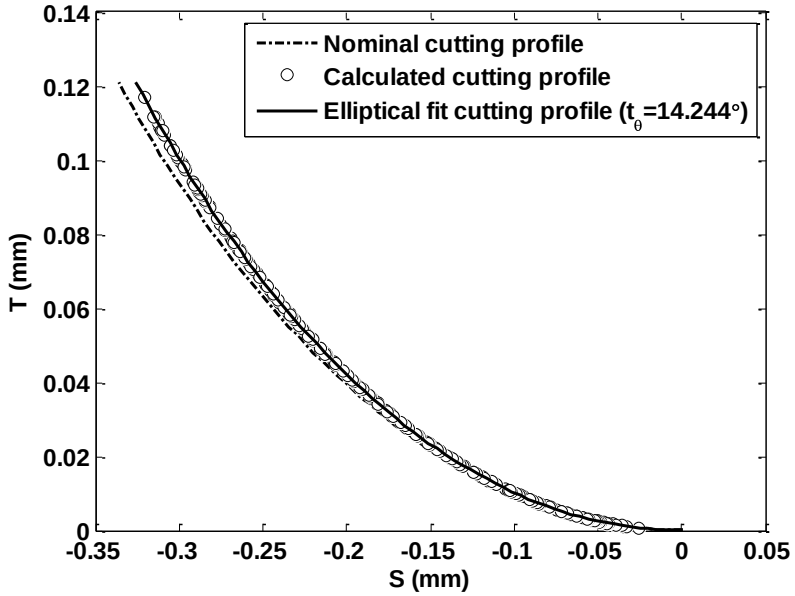

Figure 6.17. Cutting profile of a misaligned tool in (S,T) coordinates. S and T are what the program radial and axial tool compensation offsets should be. The nominal tool profile is what the cutting profile would be if the tool had no orientation error (t_θ = 0). The actual tool cutting profile is calculated using the measured test surface profile and Eqs. 2 and 3. An off-center ellipse is fit to the calculated cutting profile. Eq. (6-4) gives a value of 14.244° for t_θ.

$$|t_\theta| = \cos^{-1}\left(\frac{\text{minor diameter}}{\text{major diameter}}\right) \tag{6-4}$$

For low waviness tools, most of the form error can be corrected just by removing or compensating tool misalignments as described in this section. Figure 6.18 shows a measurement of a 2 mm test part using the WEC system over a 3 mm scan range using a 1 mm radius probe tip. Correcting t_h, t_c, and t_θ leads to a surface profile measurement with 0.04% radius error and 21 nm root-mean-square (RMS) form error, both of which are very tight tolerances for plastic lenses.

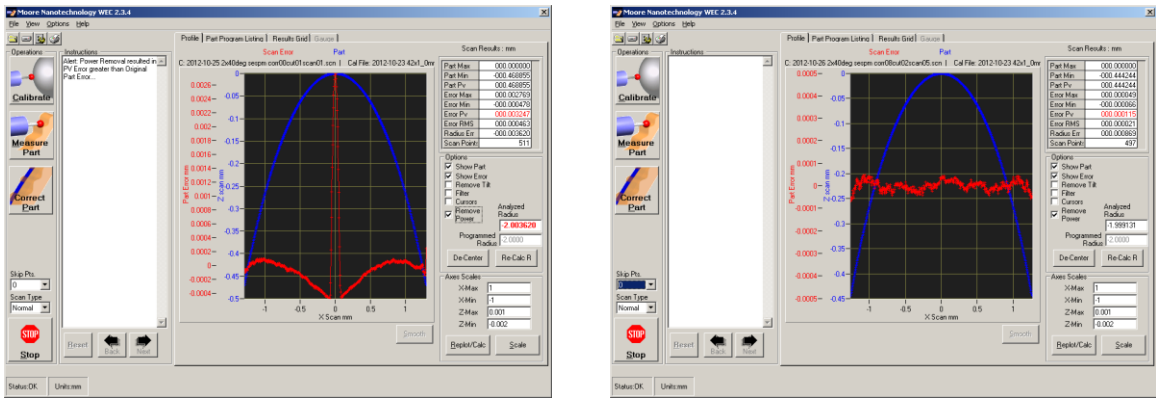

(a) (b)

Figure 6.18. (a) WEC error measurement of a 2 mm radius test part before applying corrections. The errors t_h and t_c contribute to a nub in the middle of the lens. The 1 mm radius WEC probe has difficulty measuring features of this size, so the nub appears as wide spike instead. (b) WEC error measurement of a 2 mm radius test part after t_h, t_c, and t_θ have been compensated and/or corrected. The radius error of this test part as measured by WEC is 0.869 µm (0.04%), and the RMS form error as measured by WEC is 21 nm.

6.3.4. Results

Two 3x3 convex lens arrays were cut into polystyrene (Rexolite 1422). The outer diameter of each lens is 3 mm, and the radii are 2 mm (f/1.12) and 20 mm (f/11.2) (Figure 6.19). The f/11.2 lenses could also be fabricated using STS and FTS, but the f/1.12 lenses would require a tool with a 50° relief, where most tools have 40° of relief or less. The roughing passes were done using 3-axis micro-milling. Roughing using 4-axis SPDM would have required a tool with both positive and negative sweep, similar to tools used in SPDT. The ball endmills used in micro-milling have a strictly positive tool sweep. During roughing, a 3-axis micro-milling program can be run at full speed because roughness is not a concern. The finishing passes were done using the new 4-axis SPDM technique. These finishing passes did

not include tangential lead-ins or fillets. The tool misalignment compensation techniques described in the previous section were used to eliminate form error as best as possible. The same compensations were applied for every lens in the array. Aside from compensating for tool misalignment, no additional tool path compensation was applied. The top spindle speed reached in C-axis mode was approximately 126 RPM. As the spindle speed approached this limit, acceleration limits reduced the actual feed rate almost linearly. Near the end of the NC program, acceleration limits further reduced both spindle speed and feed rate to nearly zero. The radial feed rate was 5.5 μm/rev. This should theoretically yield the same surface finish as a SPDT lens cut at 2000 RPM and 11 mm/min. The finish pass for each 2 mm radius lens requires 5 minutes and 34 seconds. The finish pass for each 20 mm radius lens lasted 4 minutes and 4 seconds. Form and radius errors for 20 mm lenses were found to be reduced by running 3 warm-up dry runs prior to cutting the lenses. Each of the arrays in Figure 6.19 were cut in 50 minutes.

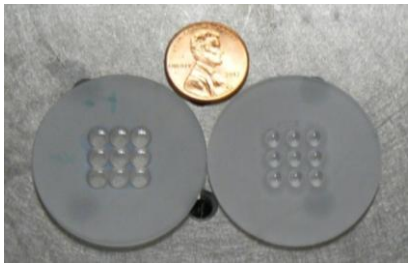

Figure 6.19. Two 3x3 polystyrene lens arrays with radii of 20 mm (left) and 2 mm (right). The finish cut for both of these lens arrays was done using the 4-axis SPDM technique.

A 0.33 mm diameter area at the apex of the 2 mm lens was measured with the NewView optical profiler to assess the surface roughness. Fringe contrast drops

off outside this area as the slope of the lens increases, which leads to measurement errors. The best fit sphere and 4th order Zernike polynomials were removed from the measured profile, and a 40 μm high-pass Gauss Spline filter was applied to the residue to obtain the roughness profile. A 12 μm diameter mask was used to exclude the nub left in the middle of the lens from the roughness calculations (Figure 6.20). The 20 mm lenses are much shallower, and can therefore be measured over a larger area. A 0.4 mm × 1.2 mm area was scanned from the apex of each 20 mm lens out towards the edge.

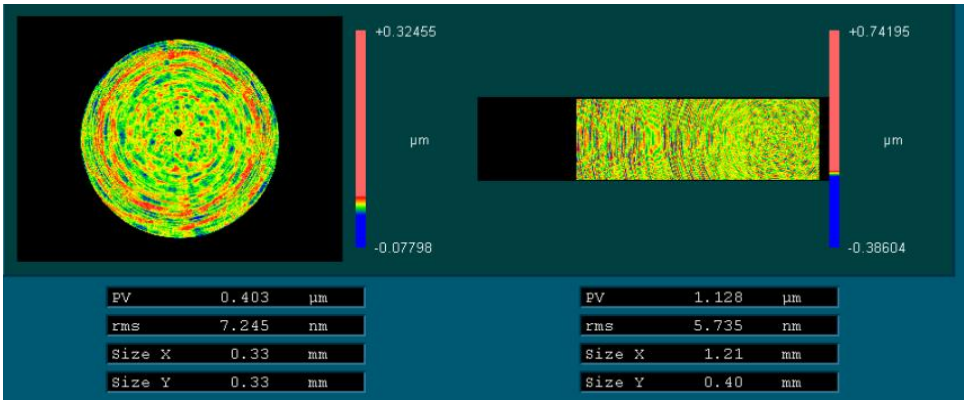

Figure 6.20. Surface profile measurements of a 2 mm lens (left) and a 20 mm lens (right) fabricated using 4-axis SPDM measured with the Zygo® NewView™ 5032 Optical Profiler. RMS roughness and R_q are the same.

The PTI250 was used to measure surface form error and lens radii. A 1.27 mm diameter area of the surface was measured using an f/1.5 transmission sphere. This transmission sphere is not fast enough to measure the entire lens surface, but the PTI250 f/0.58 transmission sphere has a negative working distance and cannot be used. An f/4.8 transmission sphere was used to measure a 2.75 mm diameter area of the 20 mm radius lenses (Figure 6.21). Focusing error was removed from the

form error measurements and a 40 μm low-pass Gauss spline filter was applied to the residue to eliminate surface roughness from the surface form error calculation.

Visible in the surface plots of all lenses is a ridge running almost vertically across the face of the lens. This is an artifact caused by following errors in the Y-axis. These artifacts cover a small area, however. Judging from the RMS form errors of these lenses, none of which is larger than 30 nm, the influence of these artifacts on lens performance will be negligible. The RMS surface roughness (R_q), RMS form error, and radius error of both lens arrays are shown in Tables 6.4 and 6.5.

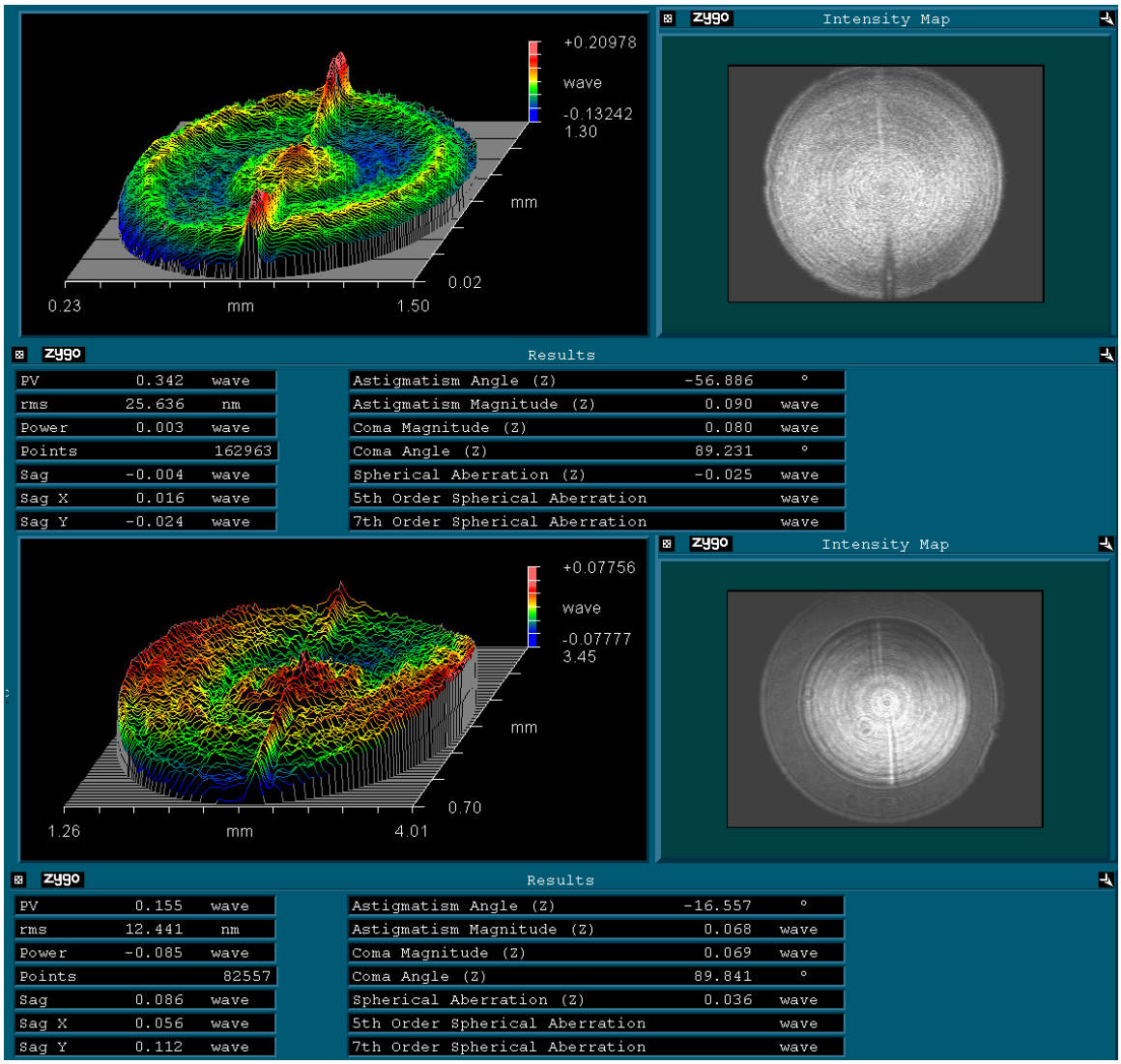

Figure 6.21. Surface form error of a 2 mm lens (top) and a 20 mm lens (bottom) fabricated using 4-axis SPDM measured with the Zygo® PTI250.

Table 6.4 Roughness, surface form error, and radius error measurements for a 3x3 array of lenses having 2 mm radii of curvature. These lenses were fabricated by 4-axis SPDM.

Lens #	R_q (nm)	RMS Form Error (nm)	Radius error (μm)
1	6.98	25.94	1.58
2	6.91	24.78	2.04
3	6.06	25.17	1.59
4	7.43	23.25	1.71
5	7.25	25.64	1.70
6	5.97	22.60	1.60
7	6.74	25.22	2.15
8	6.44	29.17	1.56
9	6.25	15.92	1.61
Mean	6.67	24.83	1.73
Std Dev	0.52	2.18	0.22

Table 6.5 Roughness, surface form error, and radius error measurements for a 3x3 array of lenses having 20 mm radii of curvature. These lenses were fabricated by 4-axis SPDM.

Lens #	R_q (nm)	RMS Form Error (nm)	Radius error (μm)
1	5.74	26.92	-17.38
2	5.43	16.59	-22.88
3	5.39	27.36	18.61
4	5.52	10.34	-23.08
5	5.60	12.44	-40.85
6	5.58	19.00	-19.98
7	5.24	16.13	-0.39
8	5.64	15.40	4.18
9	5.44	15.92	0.44
Mean	5.51	17.79	-11.26
Std Dev	0.15	5.85	18.20

In order to compare cutting times between 4-axis SPDM and 3-axis micro-milling, 3 additional lenses were micro-milled using the same tool path used to cut the 20 mm lenses shown above. This tool path includes the compensations for tool misalignments t_h and t_c. A 5 μm chip per tooth was chosen in an effort to match the surface roughness of the 4-axis SPDM lenses. The spindle was run at 7,000 RPM

with a feed rate of 35 mm/min. The cutting blocks portion of this NC program, which excludes tangential lead-in, requires 45 min to execute. The surface roughness, form error and radius measurements for these lenses are shown in Table 6.6.

Table 6.6 Roughness, surface form error, and radius error measurements for three 20 mm radius micro-milled lenses.

Lens #	R_q (nm)	RMS Form Error (nm)	Radius error (μm)
1	5.46	14.04	6.47
2	5.75	13.53	-0.17
3	5.76	27.89	-0.46
Mean	5.72	18.49	1.95
Std Dev	0.07	8.15	3.92

6.3.5. Discussion

6.3.5.1. Surface quality

All of the surface errors measured for both lens arrays are very low and meet low cost tolerances for surface roughness, tight tolerances for surface form error, and state of the art tolerances for radius error (Table 6.7). Two of the 20 mm radius lenses would meet state of the art tolerances for surface form error. These tolerances are either better than or not significantly different from tolerances previously reported for micro-milling plastic lenses using the same Nanotech UPL 250 [47], and for micro-milling array masters on a Nanoform 250 in cylindrical coordinates [38,60].

The worst case tolerances expected for much larger lens arrays is determined by the 3-sigma value, whichever of $\mu \pm 3\sigma$ is further from 0. Based on this criterion, the roughness of large numbers of lenses is still expected to be similar to the roughness of the lenses shown here. With large numbers of lenses, there may be one or two that fail to meet tight tolerances for form error, but still meet commercial tolerances. 2 mm lenses can be expected to hold state of the art radius tolerances in large numbers, while a small percentage of 20 mm lenses will exceed this tolerance by a few tenths of a percent. Put another way, these results predict an 80% yield for 5x5 lens arrays of 2 mm radii that must meet tight tolerances on form error and state of the art tolerances on radius error for every lens in the array. Similarly, the predicted yield for 5x5 arrays of 20 mm lenses is 54%. The predicted yields for 10x10 arrays are 41% and 11% respectively. For higher yields on larger lens arrays, a 60 nm tolerance on form error must be accepted for any lens array, and a 0.5% tolerance on radius error must be accepted for longer radii. These tolerances are still very suitable for emerging applications of lens arrays.

Table 6.7 Tolerances of 4-axis SPDM technique

Lens Array Radius	R_q (nm)			RMS Form Error (nm)			Radius error (%)		
	Best	Worst	3σ	Best	Worst	3σ	Best	Worst	3σ
2 mm	5.97 L	7.43 L	8.22 L	21.72 T	29.17 T	31.39 C	0.08 S	0.11 S	0.12 S
20 mm	5.24 L	5.74 L	5.96 L	10.34 S	27.36 T	32.46 C	0.00 S	-0.21 S	-0.33 T
	L – Low Cost (5-10nm)			S – State of the art (<15 nm) T – Tight (15-30 nm) C – Commercial (30-60 nm)			S – State of the art (±0.3%) T – Tight (±0.5%)		

This table shows the best (absolute smallest) and worst (absolute largest) tolerances from Tables 2 and 3 and the 3-sigma, arg max(|x|,x=μ±3σ), expected worst case tolerances for larger numbers of lenses. Also included is the classification of each of these tolerances (low cost, commercial, tight, or state of the art). Here, the naming conventions are as follows: state of the art is best tolerances possible, next is tight, then commercial (standard), and then low cost. What is referred to as "state of the art" in [49] for roughness and radius error is called "tight" here, and what is referred to as "extremely tight" in [49] for roughness and radius error is called "state of the art" here. Form error here is called wavefront error in [49] and "standard" is used in [49] where "commercial" is used here. The breaks between state of the art, tight, commercial, and low cost are the same here as they are in [49].

6.3.5.2. Comparing fabrication rates

At low feed rates, micro-milling fabrication times are proportional to the area of the tool path diameter. At higher feed rates and smaller diameters, acceleration limits have a noticeable effect, and the fabrication rate of micro-milling slows. The same effect is seen in 4-axis SPDM. For lenses with millimeter scale diameter, the effect of acceleration limits can be approximated as a fixed time acceleration penalty added to the total cutting time. In addition to acceleration limits, 4-axis SPDM is also limited by the maximum C-axis spindle speed. The effect of the maximum spindle speed in 4-axis SPDM is to cause the relationship between fabrication time and part diameter to be approximately linear for diameters smaller than $F/(\pi S_{max})$, where F is the feed rate and S_{max} is the maximum spindle speed, and then to transition to a quadratic dependence. Equation (6-5) estimates cutting time for a single micro-milled lens in terms of the tool path diameter (D), feed rate (F), radial feed rate (F_{rad}), and acceleration penalty (P_{acc}). Equation (6-6) estimates the cutting time of a single lens 4-axis SPDM process.

$$t = \frac{\pi D^2}{4F \cdot F_{rad}} + P_{acc} \tag{6-5}$$

$$t = \begin{cases} \dfrac{D}{2S_{max} \cdot F_{rad}} + P_{acc}, & D < \dfrac{F}{\pi S_{max}} \\ \dfrac{\pi D^2}{4F \cdot F_{rad}} + \dfrac{F}{4\pi S_{max}^2 \cdot F_{rad}} + P_{acc}, & D \geq \dfrac{F}{\pi S_{max}} \end{cases} \quad (6\text{-}6)$$

In the 4-axis SPDM process presented here, F is 500 mm/min, F_{rad} is 0.0055 mm, and S_{max} is 126 RPM. The tool path semi-diameter of the 2 mm radius lens was 2.000 mm and this lens required 5.57 minutes of cutting time. The tool path semi-diameter of the 20 mm radius lens was 1.668 mm and required 4.07 minutes of cutting time. Using Equation (6-6) to back-calculate P_{acc} yields 32 and 26 seconds respectively. To estimate cutting times for a wider range of part diameters, P_{acc} is assumed to be 29 seconds.

Schieding et al and Davis et al both report fabrication rates of 0.4 mm^2/min with roughnesses of 7 nm and 9 nm respectively [38,60]. Both groups used a Precitech Nanoform 250 with a high speed spindle from Professional Instruments. Lenses with tool path diameters larger than 0.7 mm are expected to take longer to fabricate by micro-milling at 0.4 mm^2/min than using the 4-axis SPDM process presented here (Figure 6.22). A 5 nm surface finish is possible using a Nanotech 350 freeform generator (FG), a 0.5 mm radius tool, 250 mm/min feed rate, and 0.005 mm radial feed for a fabrication rate of 1.25 mm^2/min, although the feed rate is typically programmed to decrease linearly with each pass in the spiral path [62]. The fabrication rate of the lenses micro-milled for comparison with the 4-axis SPDM lenses was 0.19 mm^2/min with a roughness of 5.7 nm. Using the same feed rate and chip per tooth, but with a spindle speed of 60,000 RPM instead of 7,000 RPM would yield a 300 mm/min feed rate and a 1.65 mm^2/min micro-milling fabrication rate. It

is unlikely that a 5-6 nm surface roughness would be maintained at these rates, however [62].

Acceleration limits do have an effect on micro-milling time at these feed rates, and they do depend on the machine configuration. Whether the acceleration penalty for 3-axis micro-milling is assumed to be zero or 29 seconds as in 4-axis SPDM, the fabrication rate of 4-axis SPDM does not become significantly higher than 3-axis micro-milling until the tool path diameter is approximately 2 mm (Figure 6.22).

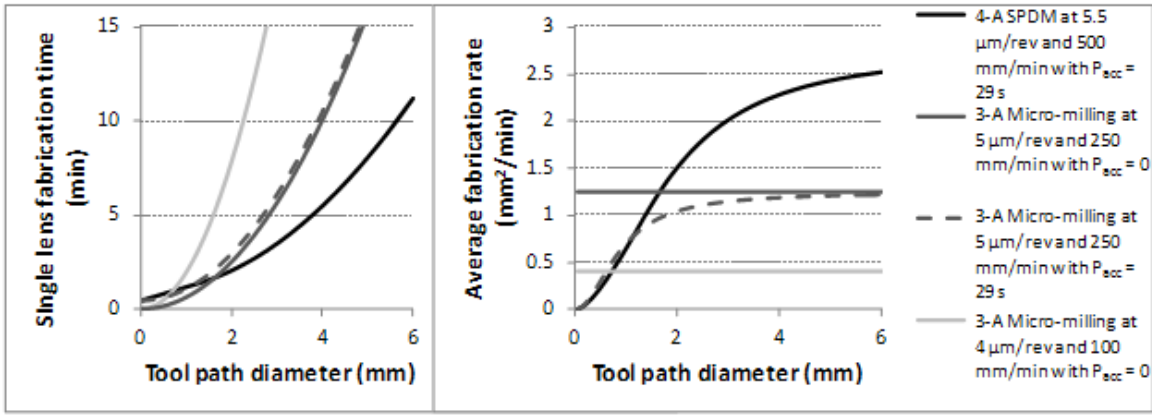

Figure 6.22. Fabrication times and fabrication rates of 4-axis SPDM vs. 3-axis micro-milling. The fastest published rate of fabrication for micro-milling is 0.4 mm²/min using a Precitech Nanoform 250 [38,60]. Peak feed rates of 250 mm/min and fabrication rates of 1.25 mm²/min are possible using a Nanotech 350 FG while maintaining a surface roughness of 5 nm [62]. The acceleration penalty is unknown at these feed rates. 4-axis SPDM at 500 mm/min has an acceleration penalty of approximately 29 s. For the sake of comparison, curves for expected micro-milling times at 1.25 mm²/min with acceleration penalties of 0 and 29 seconds are shown.

The maximum possible fabrication rate of 4-axis SPDM using the parameters presented here is 2.75 mm²/min, but only at diameters too large for most lens

arrays. Typical fabrication rates to be expected for millimeter scale lenses are 0.5-2.5 mm^2/min. The average fabrication rate achieved with the 20 mm lens was 2.12 mm^2/min. While this is not the fastest rate projected for the process, it is still 5.3x faster than fabrication rates published using cylindrical 3-axis micro-milling on a Nanoform 250 [38,60]. The fabrication rates possible today using a 0.5 mm radius tool on a Nanotech 350 FG come closer to the fabrication rates of 4-axis SPDM, but even at 250 mm/min and 0.005 mm stepover [62], the fabrication rate of the 20 mm 4-axis SPDM lenses is still 70% (2.87 minutes) faster. As the process is developed and improved, fabrication rates are expected to get faster still.

With machining processes such as SPDT, the finish cut makes a small amount of the total effort required to prototype an optical system. Setup, alignment, calibration, and fixturing and programming generally take more time than making the finish cut if the configuration needs to be changed. With micro-milling, the fabrication time is a more significant part of the prototyping process. Since fabrication services for prototyping typically cost $100 - $200 per hour, a reduction in cutting time associated with a 70% increase in fabrication rates can lower prototyping costs noticeably. Further cost and time savings can be found in the setup time, due to the fact that spindle only needs to be balanced for operation at 126 RPM. This is much easier and requires less specialized equipment than balancing a high speed spindle at 40,000 – 60,000 RPM.

6.3.6. Conclusions

A novel diamond machining technique known as 4-axis single point diamond machining has been presented. Like slow tool servo, fast tool servo, and 3-axis micro-milling, this technique is capable of producing arrays of lenses in a fully automated process. A simple method for converting an existing 3-axis micro-milling NC program to a 4-axis SPDM NC program has been described. NC compensation of 3-axis micro-milling and 4-axis SPDM tool alignments has been proposed. The 4-axis SPDM technique has been shown to produce plastic lens arrays of excellent optical quality. Lens arrays can be expected to easily meet tolerances of 10 nm roughness, 60 nm form error, and 0.5% radius error for every lens in the array. For 3x3 and 5x5 lens arrays, tolerances of 30 nm form error and 0.3% radius error are achievable. 4-axis SPDM can produce the same range of lens radii, sags, and slopes that 3-axis micro-milling currently offers, which is a wider range than STS or FTS. Thus, this technique can be used to produce both the high f/# and low f/# lenses needed in systems such as an array microscope without changing machine configuration. 3-axis micro-milling is still as fast if not faster for fabricating micro-lenses. Miniature lenses, on the other hand, with tool paths larger than 2 mm in diameter can be fabricated using 4-axis SPDM 1.2-2x faster than 3-axis micro-milling, without the use of a high speed spindle. This takes hours off the total cutting time of a complex lens array. As a result, this technique is expected to reduce the cost of prototyping novel optical systems based on arrays of miniature lenses by anywhere from hundreds to thousands of dollars.

Chapter 7

Summary

This dissertation has addressed two critical needs for development of an array microscope for Mtb detection. The first is the need for a miniature objective design. Several replicates of this objective must fit within the spatial constraints of a sputum smear while meeting the imaging requirements of FSSM. The second need is for a rapid method of diamond machining arrays of optically smooth and accurate lens surfaces into plastic substrates for prototyping.

To meet the first need, two specific aims were accomplished. In the first specific aim, a miniature objective that meets the required criteria was designed, and its performance was theoretically evaluated both nominally and with tolerances for errors expected in diamond machining. This design is the first all-plastic miniature objective designed for FSSM. The theoretical nominal and tolerance performance was found to be diffraction limited. The lens design and analysis were presented and discussed in Chapter 4, along with the justifications for the

specifications chosen based on the imaging needs of FSSM. In the second aim, this lens design was fabricated using SPDT and evaluated by imaging a resolution target with sub-micron feature sizes, AFB test slides which were also imaged by a standard microscope objective designed for use in FSSM, and by quantifying the accuracy of digital FSSM and by quantitatively comparing the accuracy of digital FSSM using this prototype objective to standard FSSM. These comparisons included counts of bacteria in matched fields of view and diagnostic comparisons. Higher bacterial counts were obtained using digital FSSM than standard FSSM, indicating that digital FSSM may be reveal organisms that cannot be seen in standard FSSM. The concurrence between digital FSSM, standard FSSM, and the reference culture diagnosis were found to be highly concordant, with a Fleiss's kappa statistic of 0.88, showing that the increase in bacterial counts is not indicative of low specificity. The initial estimates for the sensitivity and specificity of digital FSSM with the miniature objective are 100% and 95%, which are sufficiently high for diagnostic use. These evaluations confirm the expected theoretical performance and tolerance of the lens designed in the first aim. The methods used to perform these evaluations, and the results obtained by these methods were presented in Chapter 6.

The second need met by this dissertation is the need for a rapid prototyping method for production of plastic lens arrays. This was the third aim of this dissertation. The first method explored for this purpose was micro-milling. Plastic lenses were micro-milled for the first time, demonstrating that this technique can be used as a single-step prototyping technique, rather than a first step in an injection molding process. The form of these lenses was found to be very accurate, nearly

state of the art, and the accuracy of the lens radii were found to be better than state of the art. The surface of these lenses was initially thought to be optically smooth, but upon further examination of the process, it was found that a smooth plastic surface could not be produced without lengthening the process considerably. Other researchers have found these limitations as well in the production of lens molds and overcome them with advanced equipment, such as a high speed spindle, which our equipment could not be retrofitted for. With micro-milling ruled out as a rapid diamond machining process, a new technique, never before used in lens array fabrication, was developed that did not require any modification of our equipment. This diamond machining process is known as 4-axis single point diamond machining, and as of today, it can reach fabrication rates for miniature lenses that are twice as fast as the state of the art of micro-milling, and nearly 10x faster than micro-milling with a low-speed spindle. The form and radius accuracies remain unchanged compared to our previous micro-milling experiments, and the surface quality is significantly better. With the lens fabrication time reduced from 45 minutes to 5 minutes per lens, this diamond machining process is expected to accelerate the development of an array microscope for Mtb detection.

In order to accomplish the goal of an array microscope, future work is needed in fabrication and system integration. The first task that must be accomplished is the fabrication of precisely aligned bi-convex, bi-concave, and meniscus lenses with optically smooth surface finish. The principles of such a technique were proposed in Chapter 6. A method of lens array fabrication that embodies these principles was implemented and tested. The results are promising

since a discernible image of micron-scale features could be formed with this lens array. This suggests that the alignment tolerances are close to being met. The optical surface and imaging quality was not what was expected or desired, however. Alternative alignment systems are already under development and are nearing the testing phase. 4-axis SPDM has also been shown to provide improved surface quality over micro-milling in a rapid fabrication process, so lens array fabrication technology may be nearing maturity soon. The next task that must be accomplished in order to complete the array microscope is the integration of the imaging lens array with individually addressable illumination systems. This could be done by creating an array of LEDs with individual power supply lines on a printed circuit board, where each LED has its own collector and condenser lens. These LEDs could be placed just beneath the sample which would be illuminated in transmission. Finally, the digital FSSM technique would need to be tested with the array microscope on a larger scale. The non-significant, but noticeable tendency of digital FSSM to lead to more positive results, both true positives and false positives, should be further explored to determine if it is a real effect and if so whether it needs to be enhanced or mitigated if the effect has a significant impact on treatment decisions.

The research presented in this dissertation also has potential applications in other areas of research and development. Any microscopy-based test for pathogen detection, of which Mtb is just one, would benefit from the use of a high-throughput, easy to use array microscope. Malaria is another example of a disease where microscopy is a common method of detection in the developing world [63]. Miniature lens arrays have also found use in hyperspectral imaging systems [64]

and LED illumination systems [65], so the improvements in their manufacture will likely be put to use in these applications as well.

References

1. World Health Organization Tuberculosis Programme, *Framework for Effective Tuberculosis Control* (World Health Organization, 1994).
2. WHO, "WHO | The world health report 2004 - changing history," http://www.who.int/whr/2004/en/.
3. C. Dye, G. P. Garnett, K. Sleeman, and B. G. Williams, "Prospects for worldwide tuberculosis control under the WHO DOTS strategy," The Lancet **352**, 1886–1891 (1998).
4. World Health Organization, "Tuberculosis control programme," in (WHO, n.d.), Vol. WHA44.8.
5. C. Dye, "Global epidemiology of tuberculosis," The Lancet **367**, 938–940 (2006).
6. WHO, *WHO | Global Tuberculosis Control - Surveillance, Planning, Financing* (WHO, 2006).
7. E. Keeler, M. D. Perkins, P. Small, C. Hanson, S. Reed, J. Cunningham, J. E. Aledort, L. Hillborne, M. E. Rafael, F. Girosi, and C. Dye, "Reducing the global burden of tuberculosis: the contribution of improved diagnostics," Nature **444**, 49–57 (2006).
8. K. R. Steingart, M. Henry, V. Ng, P. C. Hopewell, A. Ramsay, J. Cunningham, R. Urbanczik, M. Perkins, M. A. Aziz, and M. Pai, "Fluorescence versus conventional sputum smear microscopy for tuberculosis: a systematic review," The Lancet Infectious Diseases **6**, 570–581 (2006).
9. M. D. Perkins and J. Cunningham, "Facing the Crisis: Improving the Diagnosis of Tuberculosis in the HIV Era," The Journal of Infectious Diseases **196**, S15–S27 (2007).
10. WHO Stop TB, *Roadmap for Rolling Out Xpert MTB/RIF for Rapid Diagnosis of TB and MDR-TB* (WHO, 2010).
11. World Health Organization, "Policy statement: Automated real-time nucleic acid amplification technology for rapid and simultaneous detection of tuberculosis and rifampicin resistance: Xpert MTB/RIF system," (2011).
12. C. Liang, M. Descour, K.-B. Sung, and R. Richards-Kortum, "Fiber confocal reflectance microscope (FCRM) for in-vivo imaging," Opt. Express **9**, 821–830 (2001).
13. E. Laemmel, M. Genet, G. Le Goualher, A. Perchant, J.-F. Le Gargasson, and E. Vicaut, "Fibered Confocal Fluorescence Microscopy (Cell-viZio™) Facilitates Extended Imaging in the Field of Microcirculation," Journal of Vascular Research **41**, 400–411 (2004).
14. A. Osdoit, M. Genet, A. Perchant, S. Loiseau, B. Abrat, and F. Lacombe, "In vivo fibered confocal reflectance imaging: totally non-invasive morphological cellular imaging brought to the endoscopist," 608208–608208 (2006).

15. D. Wang, B. V. Hunter, M. J. Cobb, and X. Li, "Super-Achromatic Rapid Scanning Microendoscope for Ultrahigh-Resolution OCT Imaging," IEEE Journal of Selected Topics in Quantum Electronics **13**, 1596–1601 (2007).
16. M. D. Chidley, K. D. Carlson, R. R. Richards-Kortum, and M. R. Descour, "Design, assembly, and optical bench testing of a high-numerical-aperture miniature injection-molded objective for fiber-optic confocal reflectance microscopy," Appl. Opt. **45**, 2545–2554 (2006).
17. R. T. Kester, T. S. Tkaczyk, M. R. Descour, T. Christenson, and R. Richards-Kortum, "High numerical aperture microendoscope objective for a fiber confocal reflectance microscope," Opt. Express **15**, 2409–2420 (2007).
18. R. T. Kester, T. Christenson, R. R. Kortum, and T. S. Tkaczyk, "Low cost, high performance, self-aligning miniature optical systems," Appl. Opt. **48**, 3375–3384 (2009).
19. M. Kyrish, U. Utzinger, M. R. Descour, B. K. Baggett, and T. S. Tkaczyk, "Ultra-slim plastic endomicroscope objective for non-linear microscopy," Opt. Express **19**, 7603–7615 (2011).
20. M. Kyrish and T. S. Tkaczyk, "Achromatized endomicroscope objective for optical biopsy," Biomedical Optics Express **4**, 287 (2013).
21. I. N. de Kantor and K. Weyer, *Laboratory Services in Tuberculosis Control* (World Health Organization, 1998).
22. N. Selvakumar, M. Gomathi, F. Rehman, and P. R. Narayanan, "Evaluation of a two-reagent cold staining method for detection of acid-fast bacilli," Int. J. Tuberc. Lung Dis **6**, 728–731 (2002).
23. S. Gupta, V. Prasad, I. Bairy, and S. Muralidharan, "Comparative evaluation of two cold staining methods with the Ziehl-Neelsen method for the diagnosis of tuberculosis," Southeast Asian J. Trop. Med. Public Health **40**, 765–769 (2009).
24. J. Mardoquio and P. Cernoch, "Fluorochrome Stain," (1999).
25. "FIND - FIND-negotiated prices for Primo Star iLED and country list," http://www.finddiagnostics.org/about/what_we_do/successes/find-negotiated-prices/primo-star-iled.html.
26. A. R. Miller, G. L. Davis, Z. M. Oden, M. R. Razavi, A. Fateh, M. Ghazanfari, F. Abdolrahimi, S. Poorazar, F. Sakhaie, R. J. Olsen, A. R. Bahrmand, M. C. Pierce, E. A. Graviss, and R. Richards-Kortum, "Portable, Battery-Operated, Low-Cost, Bright Field and Fluorescence Microscope," PLoS ONE **5**, e11890 (2010).
27. R. W. Smithwick, "Laboratory Manual for Acid-Fast Microscopy," (1976).
28. Médecins Sans Frontières, *Results from a Questionnaire Entitled: Specifications for Point-ofCare TB Tests Expert Opinion Check from TB Field Practitioners* (Médecins Sans Frontières, 2009).
29. R. S. Weinstein, M. R. Descour, C. Liang, G. Barker, K. M. Scott, L. Richter, E. A. Krupinski, A. K. Bhattacharyya, J. R. Davis, A. R. Graham, M. Rennels, W. C. Russum, J. F. Goodall, P. Zhou, A. G. Olszak, B. H. Williams, J. C. Wyant, and P. H. Bartels, "An array microscope for ultrarapid virtual slide processing and telepathology. Design, fabrication, and validation study," Hum. Pathol. **35**, 1303–1314 (2004).

30. B. Potsaid, Y. Bellouard, and J. Wen, "Adaptive Scanning Optical Microscope (ASOM): A multidisciplinary optical microscope design for large field of view and high resolution imaging," Opt. Express **13**, 6504–6518 (2005).
31. E. Schonbrun, S. S. Gorthi, and D. Schaak, "Microfabricated multiple field of view imaging flow cytometry," Lab Chip **12**, 268–273 (2012).
32. R. Ng, M. Levoy, M. Brédif, G. Duval, M. Horowitz, and P. Hanrahan, "Light field photography with a hand-held plenoptic camera," (2005).
33. D. Miyazaki, K. Ito, Y. Nakao, T. Toyoda, and Y. Masaki, "Retrieval of Three-Dimensional Image from Compound-Eye Imaging with Defocus Using Ray Tracing," in *3rd International Conference on Innovative Computing Information and Control, 2008. ICICIC '08* (2008), p. 51.
34. J. Tanida, T. Kumagai, K. Yamada, S. Miyatake, K. Ishida, T. Morimoto, N. Kondou, D. Miyazaki, and Y. Ichioka, "Thin Observation Module by Bound Optics (TOMBO): Concept and Experimental Verification," Appl. Opt. **40**, 1806–1813 (2001).
35. Z. D. Popovic, R. A. Sprague, and G. A. N. Connell, "Technique for monolithic fabrication of microlens arrays," Appl. Opt. **27**, 1281–1284 (1988).
36. W. R. Cox, T. Chen, and D. J. Hayes, "Micro-Optics Fabrication by Ink-Jet Printers," Opt. Photon. News **12**, 32–35 (2001).
37. J. Rogers, A. Kärkkäinen, T. Tkaczyk, J. Rantala, and M. Descour, "Realization of refractive microoptics through grayscale lithographic patterning of photosensitive hybrid glass," Opt. Express **12**, 1294–1303 (2004).
38. G. E. Davis, J. W. Roblee, and A. R. Hedges, "Comparison of freeform manufacturing techniques in the production of monolithic lens arrays," Proc SPIE **7426**, 742605 (2009).
39. N. C. R. Holme, T. W. Berg, and P. G. Dinesen, "Diamond micro-milling for array mastering," Proc SPIE **7062**, 70620J (2008).
40. B. McCall, M. Pierce, E. A. Graviss, R. Richards-Kortum, and T. Tkaczyk, "Toward a low-cost compact array microscopy platform for detection of tuberculosis," Tuberculosis **91**(Suppl 1), S54–60 (2011).
41. Brian McCall, R. J. Olsen, Nicole J. Nelles, Dawn L. Williams, Kevin Jackson, Rebecca Richards-Kortum, Edward A. Graviss, and Tomasz S. Tkaczyk, "Evaluation of a miniature microscope objective designed for fluorescence array microscopy detection of Mycobacterium tuberculosis," Arch Pathol Lab Med, accepted pending revisions, March 21, 2013.
42. D. B. Murphy, *Fundamentals of Light Microscopy and Electronic Imaging* (John Wiley & Sons, 2002).
43. M. G. Forero, G. Cristóbal, and M. Desco, "Automatic identification of Mycobacterium tuberculosis by Gaussian mixture models," Journal of Microscopy **223**, 120–132 (2006).
44. P. Cernoch, "Kinyoun's acid fast stain," (1996).
45. J. L. Fleiss, B. Levin, and M. C. Paik, "Statistical Inference for a Single Proportion," in *Statistical Methods for Rates and Proportions* (John Wiley & Sons, Inc., 2004), pp. 17–49.

46. B. McCall and T. S. Tkaczyk, "Rapid fabrication of miniature lens arrays by four-axis single point diamond machining," Optics Express **21**, 3557 (2013).
47. B. McCall and T. Tkaczyk, "Fabrication of plastic microlens array for array microscopy by three-dimensional diamond micromilling," Opt. Eng. **49**, (2010).
48. Contour Fine Tooling and Technodiamont, "Reaching new heights in clearance and sweep," Cutting Edge (2012).
49. M. Pfeffer, "Optomechanics of Plastic Optical Components," in *Handbook of Plastic Optics*, S. Bäumer, ed. (Wiley-VCH, 2005), pp. 7–33.
50. S. Schieding, R. Steinkopf, A. Kolbmüller, S. Risse, R. Eberhardt, and A. Tünnerman, "Lens array manufacturing using a driven diamond tool on an ultra precision lathe," in *Proceedings of the European Society for Precision Engineering and Nanotechnology*, H. van Brussel, ed. (EUSPN, 2009), Vol. 2, pp. 423–426.
51. B. McCall and T. Tkaczyk, "Rapid fabrication of miniature lens arrays by four-axis single point diamond turning," US Provisional patent application 61/736,222, filed Dec 12, 2012.
52. A. Y. Yi and L. Li, "Design and fabrication of a microlens array by use of a slow tool servo," Opt. Lett. **30**, 1707–1709 (2005).
53. C.-C. Chen, Y.-C. Cheng, W.-Y. Hsu, H.-Y. Chou, P.-J. Wang, and D. P. Tsai, "Slow tool servo diamond turning of optical freeform surface for astigmatic contact lens," 812617–812617 (2011).
54. S. Scheiding, A. Y. Yi, A. Gebhardt, L. Li, S. Risse, R. Eberhardt, and A. Tünnermann, "Freeform manufacturing of a microoptical lens array on a steep curved substrate by use of a voice coil fast tool servo," Opt Express **19**, 23938–23951 (2011).
55. T. D. Milster and T. S. Tkaczyk, "Miniature and Micro-Optics," in *Handbook of Optics*, M. Bass, ed., 3rd ed. (McGraw-Hill Professional, 2010), Vol. 1, pp. 22.1–22.50.
56. F. T. O'Neill, C. R. Walsh, and J. T. Sheridan, "Photoresist reflow method of microlens production: modeling and fabrication techniques," 197–208 (2004).
57. S. Audran, B. Faure, B. Mortini, J. Regolini, G. Schlatter, and G. Hadziioannou, "Study of mechanisms involved in photoresist microlens formation," Microelectronic Engineering **83**, 1087–1090 (2006).
58. W. H. Hsieh and J. H. Chen, "Lens-profile control by electrowetting fabrication technique," IEEE Photonics Technology Letters **17**, 606 –608 (2005).
59. H. Ottevaere, R. Cox, H. P. Herzig, T. Miyashita, K. Naessens, M. Taghizadeh, R. Völkel, H. J. Woo, and H. Thienpont, "Comparing glass and plastic refractive microlenses fabricated with different technologies," Journal of Optics A: Pure and Applied Optics **8**, S407–S429 (2006).
60. S. Scheiding, A. Y. Yi, A. Gebhardt, R. Loose, L. Li, S. Risse, R. Eberhardt, and A. Tünnermann, "Diamond milling or turning for the fabrication of micro lens arrays: comparing different diamond machining technologies," Proc SPIE **7927**, 79270N (2011).

61. Moore Nanotechnology Systems LLC, "General diamond machining parameters for ultra-precision machining systems," (2003).
62. T. Stewart, personal communication (January 15, 2013).
63. WHO Global Malaria Programme, "World Malaria Report 2010," (2010).
64. L. Gao, N. Bedard, N. Hagen, R. T. Kester, and T. S. Tkaczyk, "Depth-resolved image mapping spectrometer (IMS) with structured illumination," Opt. Express **19**, 17439–17452 (2011).
65. P. Schreiber, S. Kudaev, P. Dannberg, and U. D. Zeitner, "Homogeneous LED-illumination using microlens arrays," Proc SPIE **5942**, 59420K (2005).

Appendix A

Calculation of area imaged by array microscope

Not all fields of view are fully imaged by the CCD of the DSLR camera. The extent to which each field of view overlaps with the CCD is diagramed in Figure A1. In order to compute the total areas imaged by the array microscope, the areas of each overlap must be computed.

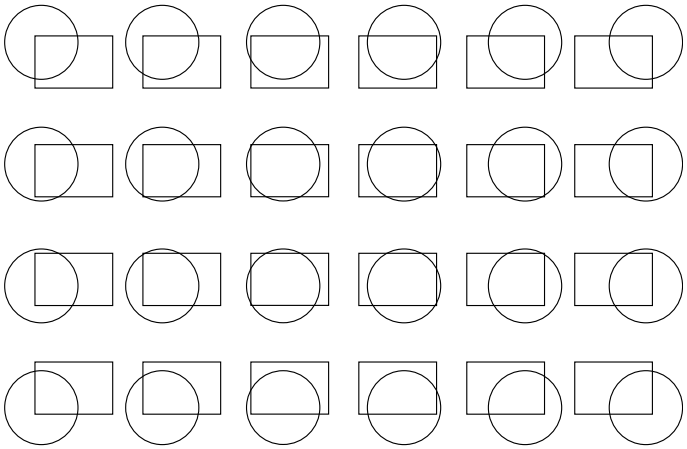

Figure A1. Overlap of fields of view of each array microscope subsystem with the CCD.

Calculating the area of overlap between an image and the CCD is a straightforward process. The intersection of the lines bounding the CCD and the

field of view form chords, as shown in Figure A2(a). The area subtended by these chords must be subtracted from the area of the field of view. Equation A1 gives the area of a chord with chord length c. When the corners of the CCD lie within the area of the image, there may be one or more chords that overlap. The area of the overlap between these chords must be added back to the area calculated for the overlap of the image and CCD. Equation A2 gives the area adjacent to the corner shown in Figure A2(b).

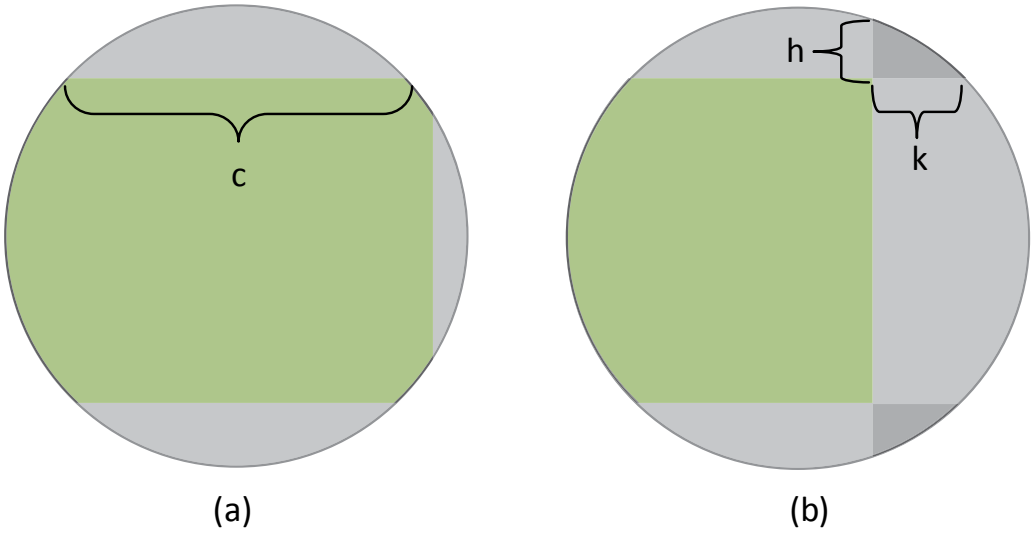

Figure A2. (a) Area of overlap between image and CCD, green, can be calculated by subtracting the area of the chords that lie outside the CCD sensor area, grey. (b) The chords will overlap when the corners of the CCD lie within the field of view.

$$A_{chord}(c) = R^2 \sin\left(\frac{c}{2R}\right) - \frac{c}{2}\sqrt{R^2 - \frac{c^2}{4}} \qquad \text{(A1)}$$

$$A_{corner}(h,k) = \int_0^h \sqrt{R^2 - t^2}\,dt + \int_0^k \sqrt{R^2 - t^2}\,dt - hk$$
$$= \frac{1}{2}\left[h\sqrt{R^2 - h^2} + k\sqrt{R^2 - k^2} + R^2\left(sin^{-1}\left(\frac{k}{R}\right) + sin^{-1}\left(\frac{h}{R}\right)\right)\right] - hk \quad \text{(A2)}$$

Once all chords and corners are found, the area of the overlap is given by Equation A3. This calculation is implemented in Matlab using the code shown in the next section. In the section that follows, the code used to calculate the total amount of overlap for an array with a given field of view and pitch (the spacing between lenses) is given.

$$A_{overlap} = \pi R^2 - \sum_i A_{chord}(c_i) + \sum_i A_{corner}(h_i, k_i) \quad \text{(A3)}$$

A.1 Calculation of overlap between image and sensor

```
function A = overlap(w,h,R,x,y,magnification)

  A = pi*R^2;

  x = abs(x);
  y = abs(y);

  for y0 = h/2 + [y -y]
    if abs(y0) >= R
      continue
    end
    f = @(t)(sqrt(R^2-t^2)-y0);
    a = fsolve(f,0.001, optimset('Display', 'off'));
    A = A - R^2*asin(a/R) + a*sqrt(R^2-a^2);
  end

  for x0 = w/2 + [x -x]
    if abs(x0) >= R
      continue
    end
    f = @(t)(sqrt(R^2-t^2)-x0);
    a = fsolve(f,0.0001, optimset('Display', 'off'));
    A = A - R^2*asin(a/R) + a*sqrt(R^2-a^2);
  end
```

```
  corners = [[w;h] [-w;h] [-w;-h] [w;-h]]*0.5 ...
    + [x x x x; 0 0 0 0] + [0 0 0 0; y y y y];

  for k=1:length(corners)
    a = abs(corners(1,k));
    b = abs(corners(2,k));

    if norm([a b]) >= R
      continue
    end
    A = A + 0.5*(a*sqrt(R^2 - a^2) + b*sqrt(R^2 - b^2)) ...
      + 0.5*R^2*(asin(a/R) + asin(b/R)) - a*b;
  end

  A = A / magnification^2;

end
```

A.2 Calculation of total area imaged by an array

```
function A = arrayoverlap(smearwid,...
             smearht,...
             CCDwid,...
             CCDht,...
             fov,...
             pitch,...
             magnification)

  Nrow = round(CCDht/pitch*2);
  Ncol = round(CCDwid/pitch*2);

  [a,b] = meshgrid((-Ncol/2):(Ncol/2),(-Nrow/2):(Ncol/2));
  a = a*pitch;
  b = b*pitch;

  A = 0;

  for a0 = [0 pitch/2]
    for b0 = [0 pitch/2]
      ai = a + a0;
      bi = b + b0;
      idx = ai < smearwid/2 & ai > -smearwid/2 ...
        & bi < smearht/2 & bi > -smearht/2;
      d = sqrt(ai.^2 + bi.^2);
      bedge = abs(bi).*(1 + magnification*(fov/2)*abs(bi)./d);
      aedge = abs(ai).*(1 + magnification*(fov/2)*abs(ai)./d);
      full = bedge < smearht/2 & aedge < smearwid/2;
      Ai = 0.25*pi*fov^2*sum(full(:));
      idx = idx & ~full;
```

```
      ai = ai(idx);
      bi = bi(idx);
      Ai = 0;
      for k=1:length(ai)
        Ai = Ai + overlap(CCDwid,...
                  CCDht,...
                  fov/2*magnification,...
                  ai(k),...
                  bi(k),...
                  magnification);
      end
      if Ai > A
        A = Ai;
      end
    end
  end


end
```